Assessing the impact of climate change on longshore sediment transport along the central Dutch coast using statistical downscaling

C. D. Rozas Rojas

TUDelft Delft University of Technology

UC UNIVERSIDAD DE CANTABRIA

Oregon State University

Deltares Enabling Delta Life

Challenge the future

Assessing the impact of climate change on longshore sediment transport along the central Dutch coast using statistical downscaling

By

Carlos David Rozas Rojas

in partial fulfilment of the requirements for the degree of

Master of Science
in Civil Engineering

at the Delft University of Technology,
to be defended publicly on Wednesday August 30, 2017 at 10:00 AM.

Thesis committee::	Prof. dr. ir. A. J. H. M. Reniers	TU Delft
	Dr. ir. D. J. R. Walstra	TU Delft/Deltares
	Dr. ir. S. Caires	Deltares
	Ir. F. Scheel	Deltares
	Dr. ir. O. Morales-Nápoles	TU Delft

An electronic version of this thesis is available at http://repository.tudelft.nl/

This thesis is part of a collaboration between:

Preface

This thesis marks the end of my studies at TU Delft, following the Coastal Engineering specialization from the Hydraulic Engineering track. These two years in the lovely city of Delft have been a continuous learning process, not only academically but also personally.

First of all, I would like to acknowledge the funding through the "Becas Chile" Scholarship n° 73161597, from the Chilean National Scholarship Program for Graduate Studies, Advanced Human Capital Program, of the National Commission for Scientific and Technological Research (CONICYT).

I would also like to thank the support from my former company PRDW. My colleagues and the smart guidance of Javier Vásquez have cultivated my passion for the coastal discipline.

This MSc thesis work represents the first outcome of a joint research project between Deltares (Netherlands), Oregon State University (USA) and Universidad de Cantabria (Spain). This thesis has represented a challenging project which I have accomplished with the collaboration of many institutions and people. In first place, I would like to acknowledge IFREMER and NCEP for generating and making available the wave and atmospheric datasets, respectively, considered in this thesis. Acknowledgements to CSIRO-BOM for the climate model ACCESS1.0 and to Rijkswaterstaat for wave and water level observations.

I would like to thank Dirk-Jan Walstra for inviting me to participate in this collaboration and his continuous support through the whole process. His confidence in my work has been very important for fulfilling the objectives of this thesis. Thanks to Sofia Caires, who helped me a lot with her knowledge and experience. I have to express my gratitude to Oswaldo Morales-Nápoles, who showed great interest in my thesis from the first meeting, for his time and guidance regarding the vine-copula implementation, as well as Weibke Jäger. Finally from the Dutch side, I would like to thank prof. Ad Reniers and Freek Scheel for their interest in my research and the fruitful discussion and comments about this work, and Jacco Groeneweg for facilitating access to the water level time series at IJmuiden.

My deepest gratitude to Fernando Méndez and his team, who offered me an extraordinary guidance throughout the whole thesis and made my time in Spain a fruitful experience. Especial mention for José Antonio Álvarez Antolínez, who was committed to the success of this thesis from the very beginning. His friendship is one of the best achievements of my time here. Also, I have to thank Ana Rueda for post-processing the information from ACCESS1.0 model.

Of course, I would like to thank Peter Ruggiero, from Oregon State University, for his kind interest in this research and the useful insights and recommendations.

During my time living abroad, I have felt the constant support from my friends in Chile and all over the world. We had the fantastic opportunity to visit and be visited by some of them here in Europe, making our experience here unforgettable. The best wishes from my family and my family-in-law were fundamental to fight the homesickness that visited us from time to time. The memory of my grandmother, who could not make it until my return to Chile, will live in my heart forever.

I would like to also show my gratitude for all the friends I have made here at TU Delft and Deltares. You are all very welcome to spend a lovely visit to Chile.

Finally, and more importantly, I would like to express my deepest gratitude to my lovely wife Paula. She was the one who encouraged me to apply to TU Delft and pursue this MSc degree. Her daily support and company during our stay in The Netherlands has added meaning to my time here. The experiences lived together will undoubtedly become one of the most important memories of our family.

Carlos Rozas Rojas

Delft, July 2017

A low-lying country as The Netherland is prone to coastal flooding, and its risk may be enhanced by global-warming induced climate change. Sea level rise has been historically considered as the key factor in coastal retreat, but waves also play an important erosive role along the coast, which can also be affected by the changing climate. During the last years, important advances have been achieved in climate modeling, with a very detailed characterization of the different components of the climate system, for the present and for different future scenarios. However, characterization of future ocean waves is still a matter of discussion and ongoing research.

In this thesis, a statistical downscaling methodology based on weather types has been chosen to model the present wave climate and explore potential changes in future waves. These changes are quantified in terms of the impact of these variations in the longshore sediment transport. The methodology is applied to Noordwijk, selected as a representative location of the central Dutch coast.

The statistical downscaling methodology is based on a classification procedure of the predictor into similar atmospheric patterns over the wave generation areas, namely the weather types. Then, the wave data is grouped according to the occurrence of the weather types. The predictor is built from the sea level pressure fields (SLP) and the squared SLP gradients, while the predictant wave climate is characterized by significant wave height, wave peak period and mean wave direction of wind sea and swell components, resulting in unimodal or bimodal sea states.

The chronology of the weather types is modeled using an autoregressive logistic model, which incorporates the seasonality, the interannual variability and the persistence observed from the historical data. For each weather type, wave parameters are modeled using the categorical distribution for the sea-state type, non-parametric kernel density functions for the central-mass regime and two generalized Pareto distributions for the lower and upper tails of wave height and wave period data. The statistical dependence between wave parameters for each sea state is included using a vine-copula approach, where the bivariate dependence of H_s and T_p is modeled using the AC skew-t copula and the remaining relations are considered to be Gaussian.

The effect of climate change is studied using SLP predictors from the global circulation model ACCESS1.0, under the RCP8.5 scenario and period 2070-2099. The statistical model is applied to identify changes in the occurrence probability of the weather types in the future. The importance of these changes are quantified in terms of the wave-induced longshore sediment transport using the process-based model Unibest-TC. The longshore sediment transport distribution for each weather type is computed and afterwards the changes in gross and net transports are estimated using the present and future probabilities of the weather types.

In terms of the weather types, the results of this work suggest changes in the occurrence probability of the weather types in the future, with variations of ±60% with respect to present climate, and no relevant changes in the sequence of weather types, neither in terms of the transition probability matrix nor in terms of the persistence of each weather type. In terms of longshore sediment transport, significant changes are detected in the transport associated with some of the weather types. For the remaining weather types, the changes are in the order of the model uncertainty. Taking into account the contributions from all weather types, a net increase of the southward directed net longshore sediment transport with respect to the historical period is detected. This increase is driven by a decrease in northwards transport and a lower decrease in southwards

transport. This result is in line with a poleward shift of the North Atlantic storm track reported in other studies.

Most importantly, weather-type based climate classification has in this thesis been succesfully proven to be a reliable tool to analyze the wave climate at the location of interest. Furthermore, the statistical downscaling also provides a climate emulator that captures the climate dynamics at different time scales, which can be used for stochastic simulations of the atmospheric and wave climate, either for the recent past or future projections.

Table of Contents

viii

Appendixes

Appendixes

1. Introduction

1.1. Overview

Any offshore or coastal project requires a reliable long-term wave climate characterization. During the last decades, much effort has been spent in characterizing the wave climate at global scale and solving how these results can be projected to a local scale. Dynamic models are available and they can be used to bring down regional outcomes to local scale, but dynamic modeling is computationally very expensive. Therefore, statistical techniques have been developed to downscale the global model outcomes at regional scale to any local area of interest.

The increasing development of global models has been also applied to study the effects of the more evident climate change that is currently going on. Important advances in climate modeling has been achieved during the last years, with a very detailed characterization of the different components of the climate system, for the present and for different future scenarios. Although the projections of future climate have been generated by several models with high level of confidence, characterization of future ocean waves is still a matter of discussion and ongoing research.

Evaluation of the future wave climate is a fundamental task for countries such as The Netherlands, which is under the continuous threat of coastal erosion that may lead to an increased flooding risk. Under this scenario, the development of reliable tools to assess the impact of the future waves under climate change is required. Sea level rise has been considered as the most important factor regarding coastal safety, but waves could also play a rol as they are an important driver of sediment transport processes. Recent research has been focused in assessing potential changes in future wave climate which can enhance dune erosion, but less attention has been given to the wave-induced longshore sediment transport along the Dutch coast.

This issue has motivated this MSc thesis work as a joint research project between Deltares (Netherlands), Oregon State University (USA) and Universidad de Cantabria (Spain). Statistical techniques has been applied to downscale the outcomes from global circulation models at regional scale (sea level pressure fields) to the local area of interest, in order to obtain a reliable characterization of the present wave climate. The statistical downscaling is based on a climate classification, where similar atmospheric patterns over the wave generation areas are grouped in clusters named Weather Types, being one synoptic condition representative of the whole cluster. Then, the wave data is grouped according to the occurrence of the weather types, connecting the wave climate with the corresponding generating atmospheric conditions.

Afterwards, the statistical model has been applied using the climate projections for the most severe scenario (RCP8.5) and the last time slice of the 21st century (2070-2099) to explore changes in the atmospheric forcings. Finally, a process-based morphodynamic model has been run in order to obtain the longshore sediment transport distribution in the recent past and in the future scenario, aiming to quantify the changes induced by climate change. The methodology has been applied to Noordwijk, selected as a representative location of the central Dutch coast.

This research has been carried out as a graduation project to obtain a Master of Science degree in Civil Engineering, specialization Coastal Engineering, from the Faculty of Civil Engineering and Geosciences of Delft University of Technology. The daily work has been undertaken at Deltares facilities, with a research visit to Universidad de Cantabria.

Under the colaboration framework, sea level pressure fields datasets from reanalysis and from Global Circulation Models have been provided by Universidad de Cantabria.

1.2. Objective and research questions

The main objective of this thesis work is to assess the impact of climate change on the long-term longshore sediment transport along the central Dutch coast (in front of Noordwijk).

The research questions that motivate this work can be listed as:

1. Will the probability of occurrence of atmospheric synoptic patterns (weather types) change in the future? How will it change?
2. How will the longshore sediment transport be affected in the future?

1.3. Methodology

To fulfill the main objective of this thesis and give answers to the research questions, 3 main units were proposed to be completed as shown in the following flowchart.
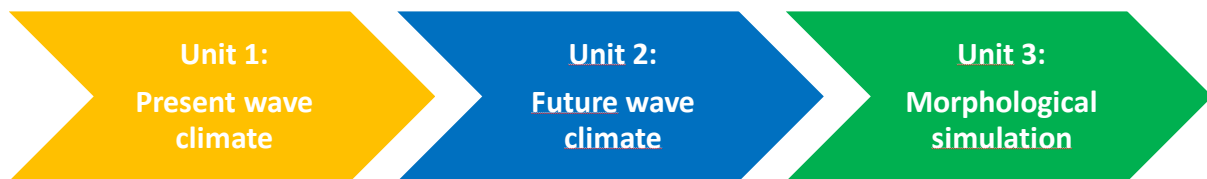
Figure 1-1: Units to be completed in this research.

In Unit 1, statistical downscaling has been be applied to characterize the present wave climate at Noordwijk, linking atmospheric variables (especifically sea level pressure fields) with the wave climate (described in terms of bulk parameters of sea states). Afterwards, in the second unit, sea level pressure fields from a global circulation model has been used as input of the statistical model to generate future wave climate. Finally, the third unit aims to assess the impact of climate change on the longshore sediment transport using a process-based morphodynamic model.

1.4. Report outline

The report is organized as follows: chapter 2 presents a literature review, addressing the most relevant topics related to this thesis, and the research methodology is given in chapter 3. The modeling of the present wave climate is covered in chapter 4, describing in detail the statistical model developed in this research. Chapter 5 presents the validation of the Global Circulation Model for the present and how changes are projected by the statistical model for the last thirty years of the 21st century. The morphological simulation is presented in chapter 6, illustrating what the impact of climate change will be in the longshore sediment transport at Noordwijk.

Finally, chapter 7 discusses the methodology followed in this study and the results from the statistical approach. The main conclusions of this work and suggestions for further research are drawn in chapter 8.

2. Theoretical Background

2.1. Wave climate modeling

Characterization of wave climate at a local scale for offshore and coastal design requires reliable data that is usually not available. In engineering projects or morphological studies, measurement campaigns of wave parameters, when part of the project/study, often spans for months and to be confident in statistical analyses, especially in the description of extreme wave climate, much larger time series are needed (time scale of decades). Therefore, wave data must be reconstructed from different sources of information. Different sources of information can be identified:

- Buoys: accurate, frequent (typically at 3 h intervals), but limited in number, very sparse and mostly close to coast (Cavaleri & Sclavo, 2006).
- Satellite altimetry: good accuracy, except for very low and high values, continuous, but very intermittent at a given location, difficulties in working close to the coast (Cavaleri & Sclavo, 2006). Data is only available from 1992.
- Voluntary observing ships (VOS): longest records of independent sea and swell, but insufficient sampling and correction algorithms are required (Gulev & Grigorieva, 2006).
- Numerical models: continuous in space and time, full information (wave spectrum) but often underestimated in enclosed basins (Cavaleri & Sclavo, 2006).

In numerical modeling, a typical approach consists in using the outputs from large-scale models to nest local models, with higher spatial resolution and more detailed formulation of the physical processes involved. This is known as dynamical downscaling and offer a solid alternative to observations, but they are computationally expensive and require detailed inputs as high-quality bathymetries and atmospheric forcings (Wang et al., 2010; Casas-Prat & Sierra, 2013).

During the last decades, effort has been put in developing numerical models capable of accurately describing the observed wave climate over a historical period. This approach is referred as *wave hindcast* when no observations are assimilated in the model, while the term *wave reanalysis* is used when observational information is considered in the model (Mínguez et al., 2011). There are several models with global coverage which use wind information from meteorological reanalysis to calculate the wind-driven wave climate, which is calibrated using available data from buoys and satellite altimetry (Caires et al., 2004; Reguero et al., 2012). Although these wind-wave models give accurate results in open ocean, they are not suitable near the coast because non-linear and wave-bottom processes are not appropriately represented. Moreover, the relative coarse grid resolution of these global models (in the order of degrees) does not allow to use them directly in local models and then downscaling is mandatory.

In contrast to dynamical downscaling, statistical downscaling appears to be a computationally cheaper approach and it has been widely applied by climatologists. In statistical downscaling for coastal applications, regional-scale meteorological variables and local met-ocean variables are related using statistical relationships. For instance, Camus et al. (2014b) have successfully applied statistical downscaling to bring down the local wave climate from sea level pressure fields at regional scale.

A combination of both approaches is also possible, the so-called hybrid approach, where computational effort is reduced combining statistical methods, data mining techniques and dynamic modeling, with accurate results [see for instance Camus et al. (2011b) and Camus et al. (2013)].

Althought validation of local wave data against measurements might be required, it is sometimes not possible and also not relevant for the accuracy of the downscaling.

2.1.1. Statistical downscaling

As previously mentioned, statistical downscaling (SD) can be defined as quantitative relationships between regional-scale atmospheric variables (predictors) and local-scale met-ocean variables (predictands) (Wilby et al., 2004). This approach is based on the following assumptions (Wilby et al., 2004; Camus et al., 2014b):

- Predictors relevant to the local-scale predictand should be adequately reproduced by the regional-scale model.
- The relationship between the predictors and the predictands should be invariant, i.e. remains valid for periods outside the fitting period.
- Variability of the predictands should be explained by the statistical relationship.
- Changes in the mean climate should lie within the range of its natural variability.

Wave reanalysis databases and atmospheric outputs from Global Circulation Models (GCMs) fulfill these conditions and have been proven to be valid predictands/predictors respectively by several authors [see for instance Caires et al. (2006); Casas-Prat et al. (2014); Antolínez et al. (2016a)].

The main advantage of the SD is its inexpensive computational cost, allowing to develop multiple realizations from different forcing conditions, faster predictand characterization and a larger number of long-term simulations. On the other hand, a SD model based on empirical probabilistic distributions of wave parameters is unable to generate local conditions that have not been registered in the past. To overcome this limitation, theoretical distributions can be fitted to the empirical data for extrapolation of extremes (Rueda et al., 2016a).

Giorgi et al. (2001) classifies the different SD approaches into i) transfer functions, ii) weather-types classification and iii) stochastic weather generators. Each method has its own strengths and weaknesses and the performance of each SD technique depends on the selection of the predictors and the local conditions of each case. Weather-type classification is preferred in this work because the link between the predictor and the predictand can be explained in physical terms, relating the local wave climate to synoptic circulation patterns (Camus et al., 2014b).

The general framework to apply the SD method for wave climatology involves the following steps:

1. Definition of the predictor and the predictand.
2. Collection of historical data for the predictor and the predictand.
3. Classification of the predictor conditions in a reduced number of weather types.
4. Classification of the predictand conditions in sea state types.
5. Formulating the statistical relationship between predictor and predictand.
6. Validation of the statistical model.

2.1.2. Predictor

2.1.2.1. Definition

Intuitively, wind speed and wind directions are the first candidates to be used as predictors for wave climate modeling because wind fields are the primary forcer of waves. Nevertheless, sea wind fields are not as well represented as sea level pressure fields in Global Circulation Models (Caires et al., 2006). Moreover, wind fields can be obtained from sea level pressure fields: the geostrophic wind

direction is well represented by the isobars and the geostrophic wind speed is proportional to the pressure gradient (Camus et al., 2014a). Following previous works (Wang et al., 2012; Camus et al., 2014b; Casas-Prat et al., 2014), the Sea Level Pressure (SLP) fields and the square of the SLP gradients (SSLPG) are considered to define the wave predictor.

After the selection of the atmospheric variables for the predictor, the spatial and temporal extent shall be defined to incorporate the sea and swell waves arriving to the area of interest. For this task, the ESTELA method (Pérez et al., 2014a) is applied to estimate the predictor area of influence and the possible temporal coverage. This method evaluates the source and travel time of wave energy reaching a target location, where the valid source points are linked to the area of interest along a great circle path over the globe without any interruption, and the travel time is computed as the effective energy flux at each point travelling at the group velocity and removing the energy loss by viscous dissipation.

Energy flux, group velocity and energy losses are computed from spectral reconstruction at each source point. The ESTELA model uses a global wave reanalysis carried out by the *Institut Francais de Recherche pour l'Exploitation de la Mer* (IFREMER). This wave database (Rascle & Ardhuin, 2013) was obtained by the numerical wave model WAVEWATCH III in its version 4.04 forced by winds from the Climate Forecast System Reanalysis (Saha et al., 2010). The wave spectrum is discretized using a spectral grid with 24 directions and 31 frequencies exponentially spaced from 0.037Hz to 0.7Hz, on a spatial and temporal resolution of 0.5° and 3 hours, respectively. Further details about ESTELA are available in Pérez et al. (2014a).

Figure 2-1 shows an example of the results from the ESTELA model for a location in the northwest Spanish coast in the North Atlantic Ocean. The upper panel depicts the effective energy flux reaching the point of interest and the travel times are indicated by the isochrones corresponding to the gray and black lines; while the lower panel presents the area of gain and loss of energy flux for the target location. In this particular case, two important areas can be identified: local sea waves arriving to target location (travel time of 1 day, black box in the figure) and swell waves travelling during 2-6 days from the whole North Atlantic Ocean (red box in the figure). In the given example, the predictor was built considering 2 spatial scales: the daily mean fields of SLP and squared SLP gradients in the local area (black box) and the daily mean fields of the same variables of the previous 4 days in the regional area (red box), being the last day of the regional area coincident with the daily mean fields of the local area.

The predictor must represent the time scale of the predictand, but there is no unique way to define it. It can be calculated as a daily predictor, where the variables are averaged over each day and the *n* previous days over a certain spatial extent are included (Camus et al., 2014a; Antolínez et al., 2016a); a monthly predictor could be constructed in the same way but using monthly averaged SLP and SSLPG (Camus et al., 2014a); or the predictor can be formulated considering the daily isochrones from the ESTELA model: the spatial domain located between the daily isochrone $i - 1$ and i is put together with the spatial domain between the isochrone i and $i + 1$ until the area defined by the last isochrone is considered in the predictor, which represent the longest possible wave propagation time from generation until reaching the target location (Hegermiller et al., 2017).
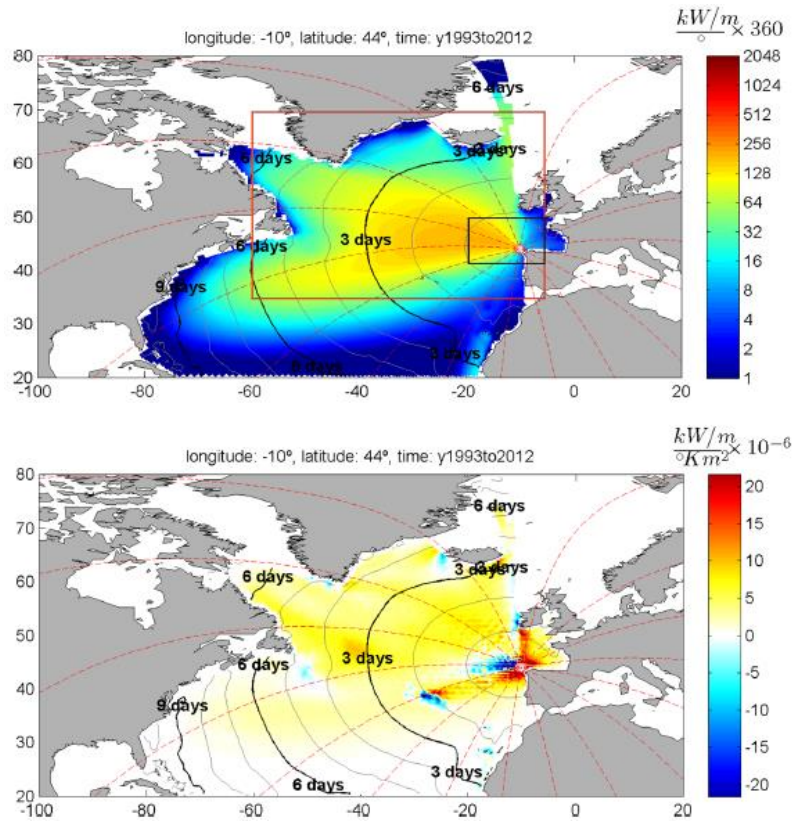
Figure 2-1: Effective energy flux at source points for target location at the Spanish northwest coast (upper panel). Travel time (in days) is represented in black and gray lines. The red and black boxes are the spatial domain of the regional predictor and the local predictor, respectively. Gain/loss of energy flux for the target point at the Spanish northwest location (lower panel). From Camus et al. (2014a).

2.1.2.2.   Sources of information

Nowadays, there are several global atmospheric reanalysis databases where Sea Level Pressure fields can be obtained. One of the most used databases among the scientific community is the NCEP/NCAR Reanalysis I (NNR) (Kalnay et al., 1996) from the National Center for Environmental Prediction (NCEP) and the National Center for Atmospheric Research (NCAR). SLP data in this global reanalysis consists of 6-hourly fields on a horizontal latitude/longitude grid of 2.5° x 2.5° (approximately 277km).

NNR was developed during the 1990s, and in the meantime, the European Centre for Medium-Range Weather Forecasts (ECMWF) conducted two reanalysis: ERA-40 (Uppala et al., 2005) and ERA-Interim (Dee et al., 2011). The former reanalysis spans from 1957 to 2002 on a horizontal grid of 1.5° x 1.5°, while the second one has a temporal coverage from 1979 to present with a spatial resolution of 0.75° x 0.75°.

In 2010, NCEP made available the outcomes from the global Climate Forecast System Reanalysis (CFSR) (Saha et al., 2010), which was extended in 2014 by NCEP Climate Forecast System Version 2 (CFSv2, Saha et al. (2014)). This reanalysis spans from 1979 to 2014 with hourly temporal resolution and spatial resolution of 0.5° x 0.5°, which is the highest resolution currently available.

2.1.3. Weather Types

Following Camus et al. (2014b), the predictor time series is partitioned into a certain number of clusters, named Weather Types (WTs), where each WT represents a synoptic atmospheric circulation pattern. This classification is generated using three different techniques.

First, a Principal Component Analysis (PCA) is applied in order to reduce data dimensionality and eliminate data redundancy with the minimum loss of variance. PCA projects the original data (the predictor) on a new space, searching for the maximum variance of the sample data. To achieve this, the predictor is written as a matrix of $n_t \times N$, where n_t is the temporal length of the records and N is twice the amount of source points in the spatial domain (the factor 2 relates with the definition of the SLP and SSLPG at each point of the spatial domain). The eigenvectors of this matrix correspond to the spatial structure of the predictor modes, named Empirical Orthogonal Functions (EOFs) and the eigenvalues represent the explained variance of the original data. Under this transformation, the original data can be expressed as a linear combination of the EOFs, where the linear coefficients are the so-called Principal Components (PCs) and only vary in time (Camus et al., 2014a):

$$X(x, t_i) = EOF_1 \cdot PC_1(t_i) + EOF_2 \cdot PC_2(t_i) + \cdots + EOF_N \cdot PC_N(t_i) \qquad (2\text{-}1)$$

The EOFs are sorted by a descending order of explained variance, being the first EOF related to the largest value of explained variance. Thus, a reduction of dimensionality can be achieved considering just the amount of modes that explain a certain percentage of the variance [see for instance Camus et al. (2014a); Espejo et al. (2014)].

Secondly, the K-means algorithm (KMA) (Camus et al., 2011c) is applied to the selected PCs. This clustering technique divides the data in n_{wt} groups, where each cluster is defined by a prototype (or centroid) which represents all the closest points in the data. Prototypes are selected as the closest data value to the average of all the data in the corresponding cluster. This set of centroids correspond to the Weather Types (WTs). The selection of the number of WTs could be a matter of optimization or to be defined based on certain criteria, such as easing the implementation, fitting and interpretation of the model results (Antolínez et al., 2016a).

Finally, the prototypes are transformed to the original space and organized in a bidimensional lattice, which allows for an intuitive visualization of the classification (see Figure 2-2 as an example). In the lattice, the arrangement of the WTs is defined by an algorithm that minimizes the sum of the distance between all the neighbors (Bermejo & Ancell, 2009). The main advantage of applying this algorithm is that WTs with similar characteristics stay together in the lattice, resembling a self-organizing map (Camus et al., 2011a), which eases the visualization of the classification and further analysis.

As an example, the lattice obtained by Camus et al. (2014b) is depicted in Figure 2-2, where 100 WTs were considered in the classification of SLP fields in the North Atlantic Ocean. It can be seen that WTs with similar patterns are located together.

A multivariate regression model between one variable of the predictand (daily significant wave height, for instance) and the corresponding daily Principal Components (predictor) may be applied to test the skill of the selected predictor (Camus et al., 2014a).
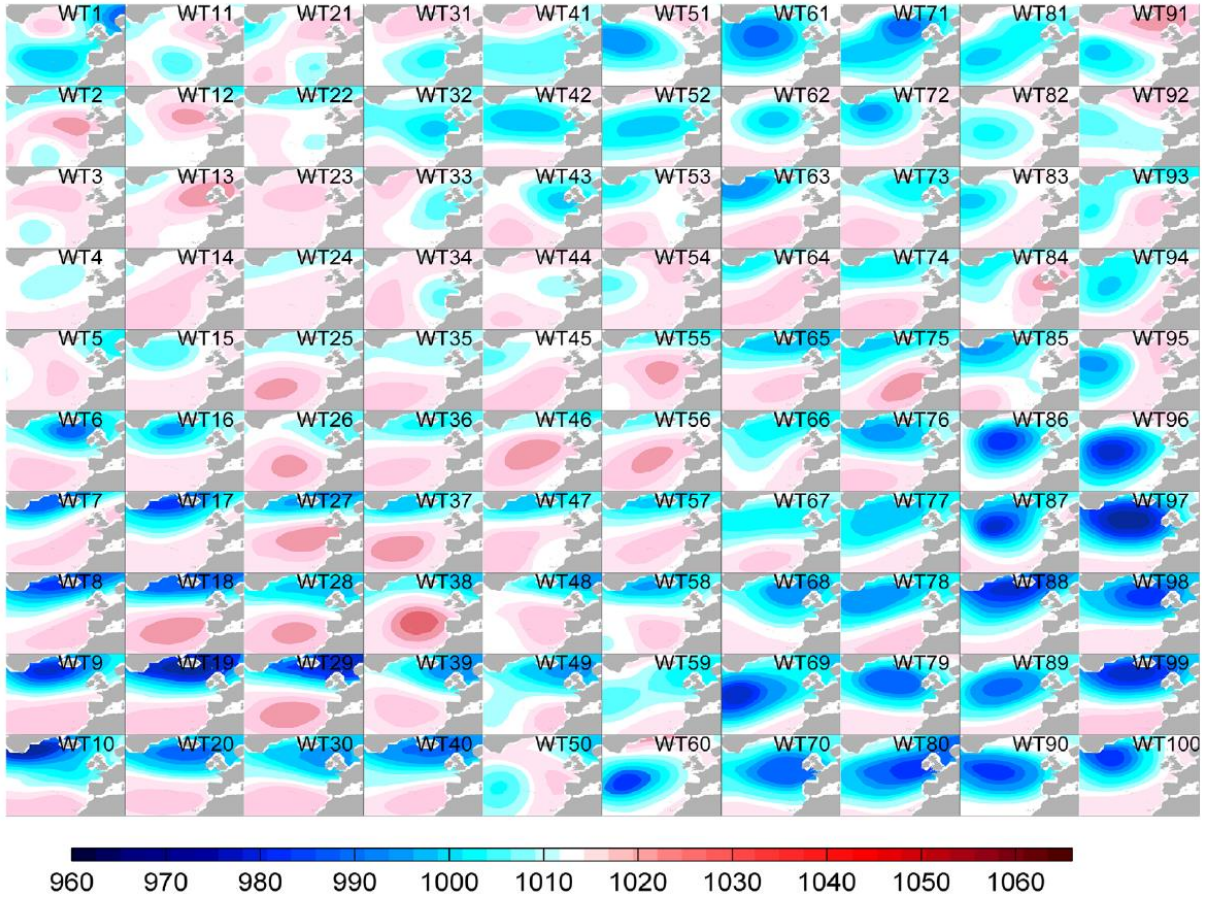
Figure 2-2: 100 WTs represented by the SLP fields (hPa) obtained from the K-means algorithm (from Camus et al. (2014b)).

2.1.4. Chronology of weather types

The temporal sequence of the WTs cannot be modeled with traditional linear regression models because WTs are a categorical variable, i.e. they just can take discrete values from 1 to n_{wt}, which are not normally distributed. Therefore, alternative regression models are required and they should be capable to reproduce the historical probability of occurrence of each WT, the transition probabilities between WTs, the persistence of each WT and the seasonal to interannual variability (Guanche et al., 2014).

Following Guanche et al. (2014), Autoregressive Logistic Regression (ALR) models are able to deal with weather type analysis including seasonality, interannual variability, long-term trends and Markov chains. The ALR model is stated as follows: let Y_t; $t = 1, \dots, n_t$ be the observations of WTs at time t with the possible outcomes $Y_t \in \{1, \dots, N_k\}$ related to each WT. Considering X_t; $t = 1, \dots, n_t$ to be a time-dependent row vector of covariates with dimensions $1 \times n_c$, with n_c the number of covariates, the probability of occurrence of Y_t is given by:

$$Prob(Y_t = i | Y_{t-1}, \dots, Y_{t-d}, X_t) = \frac{\exp\left(\pi_i^S + \pi_i^C + \pi_i^{LT} + \pi_i^{AR}\right)}{\sum_{k=1}^{n_{wt}} \exp\left(\pi_i^S + \pi_i^C + \pi_i^{LT} + \pi_i^{AR}\right)}; \; \forall i = 1, \dots, n_{wt} \qquad (2\text{-}2)$$

Where d is the number of previous WTs relevant for the model and π represents the terms referring to the different components of the model, explained as follows:

π^S: Seasonality

The seasonality is introduced in the model using harmonics:

$$\pi^S = \beta_0^S + \beta_1^S \cos(\omega t) + \beta_2^S \sin(\omega t) \tag{2-3}$$

Where β_0^S denotes the annual mean values, β_1^S and β_2^S are the amplitudes of harmonics and $\omega = 2\pi/T$ is angular frequency, with T equivalent to 1 year.

π^C: Covariates

Covariates can be regarded as any variable that could explain the behavior of the categorical variable Y, for instance atmospheric indexes or larger time scale variables, such as monthly or yearly scale for daily-based analysis. They are introduced in the model as follows:

$$\pi^C = X \cdot \beta^C \tag{2-4}$$

Where X is a row vector of covariates and β_i^C is a column vector of parameters.

π^{LT}: Long-term trends

Long-term trends in the model are included as follows:

$$\pi^{LT} = \beta^{LT} \cdot t \tag{2-5}$$

Where t denotes time, in years and β^{LT} is the long-term parameter.

Strictly speaking, eq. (2-5) does not represent the typical trend analysis because this term is related to the logarithm of the probability for each WT, but numerical results shows a good agreement on long-term changes of the WT probabilities (Guanche et al., 2014).

π^{AR}: Autoregressive or Markov chain

The autoregressive effect of order d is modeled as:

$$\pi^{AR_d} = \sum_{j=1}^{d} Y_{t-j}\gamma_j \tag{2-6}$$

Where d corresponds to the number of previous WTs which are considered to influence the actual WT, Y_{t-j} is the WT at previous time j and γ_j is the parameter associated to the WT at time j.

When fitting the model, the selection of the model parameters, i.e. the order of the autoregressive term, seasonality, covariates, etc. could be defined according to the experience of the user or based on statistical significance using the likelihood ratio (LR) statistic. This kind of test aims to check if the increment of fitting quality is justified by increasing the number of parameters. Further details can be consulted in Guanche et al. (2014).

It is important to state that all the parameters of the ALR model to be included must be transformed to the lowest time scale considered, in order to account for the different time scales in the model.

After fitting the ALR model, stochastic simulation of WT time series is possible. As it is shown in Guanche et al. (2014), validation of the synthetic WT sequences can be undertaken against the

observed sequence of WTs comparing: 1) occurrence probabilities of each WT, 2) transition probability matrix between WTs and 3) persistence analysis of WTs.

2.1.5. Predictand

2.1.5.1. Definition

As previously stated, the predictand is the set of local variables that are to be explained by the predictor. In this sense, there is no restriction in the type and number of variables to be included in the statistical model. One of the simplest relations should include the significant wave height, but it can be extended to a multivariate relation including the wave period and the wave direction. Camus et al. (2014b) showed that this set of variables at daily scale gives good results for the Spanish and Irish coasts in the North Atlantic Ocean. Clustering techniques can also be applied to the predictand in order to generate a classification into sea states, as is shown in the work of Antolínez et al. (2016a).

Espejo et al. (2014) extended the analysis and used a discretization of the wave spectra as the predictand to explore the spectral wave climate variability. A similar approach was developed by Rueda et al. (2017), where the wave spectral density was parameterized in three main components: one wind sea and two swell partitions generated from the Northern and Southern Hemisphere reaching the South California coast in USA. Under this parameterization, the predictand is a vector with 9 variables: significant wave height, wave peak period and mean wave direction for each one of the 3 partitions.

Statistical downscaling based on weather types has also been used to estimate extreme wave climate, as it is shown in Rueda et al. (2016a), who include the daily significant wave height maxima as the predictand and considered a non-stationary extreme model. Weather-type based SD has also been proven to give good results for the estimation of coastal flooding, as it is described in Rueda et al. (2016b). In the cited work, the predictand corresponds to the extreme non-tidal total water level (TWL), defined as a linear summation of storm surge and wave run-up, which is estimated as a function of the significant wave height and wave mean period. Storm surge, wave height and mean period show a strong statistical relation as they are all depending on the atmospheric synoptic patterns.

2.1.5.2. Sources of information

Several global wave reanalyses have been conducted during the last decades (Caires et al., 2004; Reguero et al., 2012). One of the latest projects corresponds to the ERA-Interim reanalysis (Dee et al., 2011), in which the atmospheric model is coupled to an ocean-wave model resolving 30 wave frequencies and 24 wave directions on a latitude/longitude grid of 0.75° x 0.75°. Analysis model outputs are available every 6 hours.

After the Climate Forecast System Reanalysis (CFSR) (Saha et al., 2010) was published, the *Institut Francais de Recherche pour l'Exploitation de la Mer* (IFREMER) carried out a global wave reanalysis based on the WAVEWATCH III model in its version 4.04, using the CFSR wind forcing and data assimilation (Rascle & Ardhuin, 2013). The computation was performed on a latitude/longitude grid of 0.5° x 0.5°, using a spectral grid with 24 directions and 31 frequencies exponentially spaced from 0.037Hz to 0.7Hz. The database spans for 20 years, from 1993 to 2012, with 3-hourly sea states, and it is the same database considered in the ESTELA model.

2.1.6. Statistical relationship

The next step when fitting the statistical model consists on projecting the local predictand into the WT classification. This aims to identify the empirical distributions of the multivariate predictand for

each weather type. As an example, Figure 2-3 shows 2 WTs from the Figure 2-2 on the left, and the central and right panels depict the joint distributions of significant wave height H_s and mean period T_m, and H_s and mean direction θ_m at the northwest Spanish coast, respectively. The key advantage of this approach is that it describes the occurrence and the main characteristics of sea states in terms of the occurrence of the different WTs.

In the given example, WT35 is the dominant WT during the summer (not shown) and it represents a neutral atmospheric condition, with weak high and low-pressure systems. From the joint distributions in the figure, the most probable H_s is approximately 1.5m, the corresponding T_m is around 7s and θ_m is NW, although a range between SW and NE is possible. On the other hand, WT97 only happens in boreal winter (not shown) and it represents an intense low-pressure system in the Northeast Atlantic with important SLP gradients. This atmospheric pattern is reflected in the observed sea state: H_s is approximately 9m, T_m is around 12s and θ_m is mainly from W. Therefore, it can be concluded in this example that local wind seas are expected in summer and swell generation predominates during winter (Camus et al., 2014b).

The marginal distributions for each parameter of the predictand can be modeled using directly the empirical distributions or fitting a theoretical cumulative density function. For instance, Rueda et al. (2017) divided the wave spectra arriving to the South California coast in 3 partitions, and showed that wave heights and wave periods from each partition followed Generalized Extreme Value distributions, and mean wave directions could be represented by empirical distributions.

Other approaches consider representing the empirical distributions using non-parametric kernel density functions (Athanassoulis & Belibassakis, 2002) or mixed models, which consist of a truncated central distribution representative of the central or main-mass regime and different distributions for the maximum and minimum regimes, representing the upper and lower tails, respectively (Solari & Losada, 2012).

2.1.7.   Weather types and atmospheric patterns

As it was explained in §2.1.3, each WT represents a synoptic atmospheric circulation pattern. One of the main advantages of this classification is the possibility of connecting the WTs with large-scale atmospheric oscillation patterns, named "teleconnection patterns" (NOAA, 2008), such as El Niño Southern Oscillation (ENSO), the North Atlantic Oscillation (NAO), the East Atlantic Oscillation (EA), the Arctic Oscillation (AO) or the Scandinavia Index (SCAND), to name a few. As an example, Camus et al. (2014b) identified that the WTs located at the bottom left of the lattice shown in Figure 2-2, are characterized by a strong low-pressure system over Iceland and a high-pressure around Azores islands, resembling the standard NAO positive mode. Moreover, WTs located at the bottom right corner of the lattice are related to the EA positive mode, with a north-south dipole like NAO but with its center located southwards.

After the statistical relation between the atmospheric classification and the predictand has been established, the link with the teleconnection patterns can be used to explain the observed local wave climate. For instance, Camus et al. (2014b) stated that wave energy is higher when the center of the atmospheric circulation pattern is closer to the target location, as it is the case for WT97 in Figure 2-3. This WT is associated with a positive phase of both NAO and EA, as it located in the lower right bottom of the lattice from Figure 2-2. Also, the configuration of the high and low-pressure systems determines the direction of the incoming waves, as it is explained by Camus et al. (2014b) and Espejo et al. (2014).

2.1.8. Multivariate dependence

Wave parameters are usually strongly correlated to each other, and any statistical model for the predictand must take this interdependence into account. One statistical tool that has been explored during the last years to model the dependence between random variables is the copulas, which have been succesfully developed in the fields of econometrics, finance, risk management or insurance (Haas, 1999; Breymann et al., 2003), and recently in meteorology and climate research (Schölzel & Friederichs, 2008), coastal (Rueda et al., 2016b) and offshore applications (Leontaris et al., 2016). For instance, Rueda et al. (2017) have shown that the joint distribution of wave parameters from multi-modal systems can be adequately represented using a multivariate Gaussian copula.
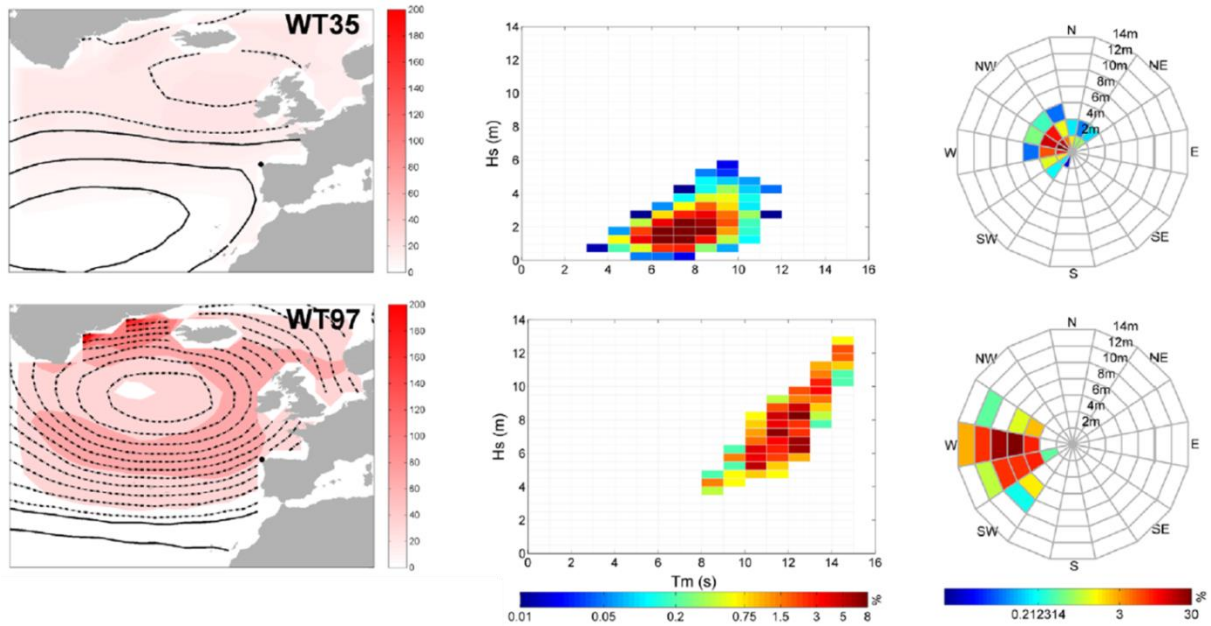

Figure 2-3: WT35 and WT97 (from the WT classification shown in Figure 2-2) with the associated distribution of hourly H_s and T_m and the distribution of H_s and mean direction at northwest Spanish coast location. The contours represent the SLP field (dashed below and continuous over 1013hPa) and the red scale represents the SLPG (from Camus et al. (2014b)).

2.1.8.1. Copulas

According to Kurowicka and Cooke (2006), a copula C is a multivariate distribution with uniform [0,1] marginal distributions. Let F be a multivariate distribution with margins $F_i(x_i)$, $i = 1, ..., n$, then the copula C can be written as:

$$C(u_1, ..., u_n) = F\left(F_1^{-1}(u_1), ..., F_n^{-1}(u_n)\right) \qquad (2\text{-}7)$$

Where $F_i^{-1}(u_i)$ are the inverse distribution functions of the marginals and u_i follows independent uniform [0,1] distributions, for $i = 1, ..., n$. C is a distribution function which also lays in the interval [0,1]. Another important property is that the copula C is unique if F is continuous (Nelsen, 2006).

As the margins of a copula lay in the interval [0,1], it offers the possibility of modeling the dependence between variables considering their cumulative distribution functions, which are defined in the same interval, regardless the marginal distribution which each variable follows (which can in fact be different than the copula). This is the main advantage of the use of copulas when modeling the statistical dependence between random variables.

The simplest case is the bivariate copula and there is a large variety of copulas (see Nelsen (2006) for an overview) which can be used to model joint distributions. One the most common copula is the Gaussian copula, whose cumulative distribution function is given by:

$$C_\rho(u_1, u_2) = \Phi_\rho\big(\Phi^{-1}(u_1), \Phi^{-1}(u_2)\big) \tag{2-8}$$

Where Φ denotes the standard cumulative Gaussian (normal) distribution and Φ_ρ is the standard bivariate cumulative Gaussian distribution function with linear correlation coefficient ρ. The extension to the multivariate case is direct, and it is equivalent to use the multivariate Gaussian distribution with linear correlation matrix Ω, which contains the correlation coefficients ρ between the set of random variables.

Despite their popularity, Gaussian copulas cannot adequately reproduce the dependence structure when existing asymmetries are significant. For instance, the wave steepness limiting condition (Holthuijsen, 2007) introduces an asymmetry in the probabilistic dependence between H_s and T_p. The recent work of Jäger and Morales Nápoles (2017) has shown that the Skew-t copula provides a better representation of the bivariate distribution of these two wave parameters. Although different formulations exist for this copula, the Skew-t copula formulated by Azzalini and Capitanio (2003) (hereafter AC skew-t copula) is considered in this work.

The cumulative distribution function of the AC skew-t copula is given by:

$$C_{\rho,\delta_1,\delta_2,\nu}(u_1, u_2) = St_2(St_1^{-1}(u_1; 0,1,\delta_1,\nu), St_1^{-1}(u_2; 0,1,\delta_2,\nu); 0,\rho,\alpha,\nu) \tag{2-9}$$

Where St_2 denotes the bivariate AC skew-t distribution with correlation coefficient ρ, a transformed skewness vector α and ν degrees of freedom. St_1 and St_2 are the univariate margins of the AC skew-t distribution and δ_1 and δ_2 are the respective skewness parameters. The formulation of the AC skew-t distribution is complicated, its univariate quantile function has no mathematical expression and must be calculated numerically, as it is explained in detail by Yoshiba (2015).

2.1.8.2. Vines

Modeling the dependence structure in a multivariate problem may be very difficult, especially when the number of variables increase (Morales Nápoles, 2011). To overcome this, Bedford and Cooke (2002) proposed a graphical model called vine, where nodes are connected by edges representing the probabilistic bivariate dependence between variables.

Graphically, a vine on n variables $\mathcal{V} = (T_1, ..., T_{n-1})$ is a nested set of trees where the edges of the tree T_j are nodes of the tree T_{j+1} and each tree has the maximum number of edges (Kurowicka & Cooke, 2006). Figure 2-4 shows a vine on $n = 5$ variables, where the tree T_j, $j = 1, ...,4$, consists of $n - j$ edges and $n - j + 1$ nodes, hence the edges from tree T_j are the nodes of tree T_{j+1}.

In a regular vine (or R-vine), one edge in tree T_{j+1} connects two edges from tree T_j, which share one node, as is the case of Figure 2-4. When this condition is violated, the vine is referred to as non-regular vine. Within regular vines, two main types are identified: canonical vines and drawable vines, also known as D-vines. In the latter, each node in tree T_1 has a maximum number of 2 edges connected, as it is the case of Figure 2-4.

In a regular vine, the nodes connected by a given edge in tree T_i are named the *constraint set* of that edge. When 2 edges are joined by an edge in tree T_i, the intersection of the respective constraint sets forms the *conditioning set*, and the symmetric difference of the constraint sets forms the

conditioned set of this edge (Kurowicka, 2011). The label of each edge denotes the conditioned and conditioning sets in Figure 2-4. For instance, the edges 1,2 and 2,3 form the constraint set of the edge 1,3|2 from tree T_2, hence the conditioned set is compounded by the nodes 1 and 3 (symmetric difference), and the conditioning set is formed by the node 2 (intersection). This is precisely what is represented by the label of the edge: 1 and 3 given 2. For further details the reader is referred to Kurowicka and Cooke (2006) and Kurowicka and Joe (2011).
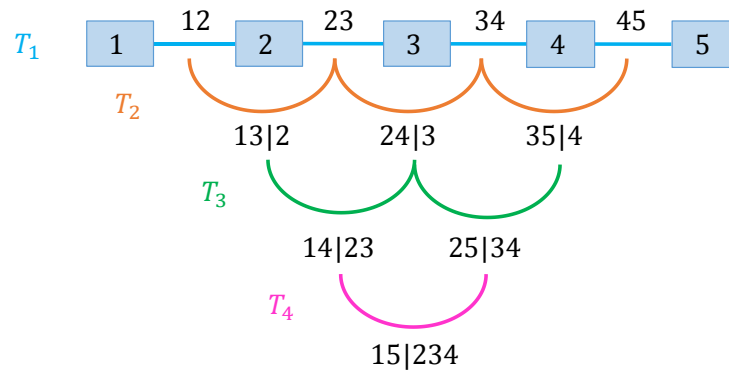

Figure 2-4: A D-vine on 5 elements showing conditioned and conditioning sets.

As it is explained in detail by Cooke et al. (2011), the first regular vine was introduced by Joe, before coining the word, during the nineties. He was focused on extending the bivariate extreme-value copula to higher dimensions, considering a class of n-variate distributions with given unidimensional margins and $n(n-1)$ dependence parameters, where $n-1$ parameters correspond to bivariate margins and the rest are related to conditional bivariate margins. The first formal definition was provided by Cooke in 1997, who was inspired by the use of Markov trees in uncertainty analyses of large risk models related to accidents at nuclear power plants. Finally, Bedford and Cooke (2002) extended the results from Joe, giving an explicit formula for the multivariate copula density in terms of (conditional) copula densities on any regular vine. Further details are given in Cooke et al. (2011).

Vines help to illustrate and model the dependence between random variables, where bivariate copulas are the building blocks of higher dimensionality dependence. In tree T_1, each edge represents the bivariate distribution between the attached nodes, and in the next trees, the relation between the elements of the conditioned set can be modeled as a bivariate distribution conditioned by the conditioning set. In other words, every edge of the regular vine is a copula for T_1 and a conditioned copula for the remaining trees.

A very good application example is provided in the work of Aas et al. (2009), who showed how multivariate data can be modeled using a regular vine as starting point: every edge of the vine corresponds to a bivariate copula density, defined by the conditioned and conditioning set. In tree T_1, the relation between the variables is defined by the rank correlation, and in the subsequent trees this relation is given by the partial correlation between the variables in the conditioned set, given the elements of the conditioning set. For instance, the edge 1,3|2 denotes the conditional copula between 1 and 3 given 2, defined by the partial correlation between 1 and 3 given 2. In this vine-copula approach, calculation of the last tree requires the computation of the previous trees.

At this point, two definitions are pending: partial correlations and conditional copulas. According to Kurowicka and Cooke (2006), the partial correlation $\rho_{12;3,\dots,n}$ between two random variables X_1 and

X_2 given $X_3, \dots, X_n$, can be interpreted as the correlation between orthogonal projections on the plane orthogonal to the space spanned by $X_3, \dots, X_n$. It can be calculated using the iterative formula:

$$\rho_{12;3,\dots,n} = \frac{\rho_{12;3,\dots,n-1} - \rho_{1n;3,\dots,n-1} \cdot \rho_{2n;3,\dots,n-1}}{\sqrt{1 - \rho_{1n;3,\dots,n-1}^2}\sqrt{1 - \rho_{2n;3,\dots,n-1}^2}} \tag{2-10}$$

For bivariate normal distribution, the partial correlation is equal to the conditional correlation. However, this is not true for other distributions and the difference can be large (Kurowicka & Cooke, 2006). The conditional correlation of X and Y given Z is defined as the product moment correlation computed with the conditional distribution of X and Y given Z (Kurowicka & Cooke, 2006):

$$\rho_{XY|Z} = \rho(X|Z, Y|Z) = \frac{E(XY|Z) - E(X|Z)E(Y|Z)}{\sigma(X|Z,)\sigma(Y|Z)} \tag{2-11}$$

Where E is the expected value and σ denotes the standard deviation.

Formally, the conditional distribution function of the bivariate copula $C(u_1, u_2)$ conditioned on u_2 is defined as (Aas et al., 2009):

$$h(u_1, u_2, \theta) = \frac{\partial C(u_1, u_2, \theta)}{\partial u_2} \tag{2-12}$$

Where θ denotes the parameters of the copula. For instance, the conditional Gaussian copula conditioned on u_2 can be written as:

$$h(u_1, u_2, \rho_{12}) = \Phi\left(\frac{\Phi^{-1}(u_1) - \rho_{12}\Phi^{-1}(u_2)}{\sqrt{1 - \rho_{12}^2}}\right) \tag{2-13}$$

Where Φ is the standard cumulative Gaussian distribution, Φ^{-1} denotes the inverse Gaussian CDF and ρ_{12} denotes the linear correlation between u_1 and u_2. The inverse conditional copula distribution is given by:

$$h^{-1}(u_1, u_2, \rho_{12}) = \Phi\left(\Phi^{-1}(u_1)\sqrt{1 - \rho_{12}^2} + \rho_{12}\Phi^{-1}(u_2)\right) \tag{2-14}$$

In practical terms, the conditional copula conditioned on u_2 is equivalent to fix the conditioning variable and take the cumulative distribution function estimated using the copula density along u_1, as it is schematized in Figure 2-5 for a conditional copula on $u_2 = 0.6$. The obtaining of the conditional copula conditioned on u_1 is analogous.
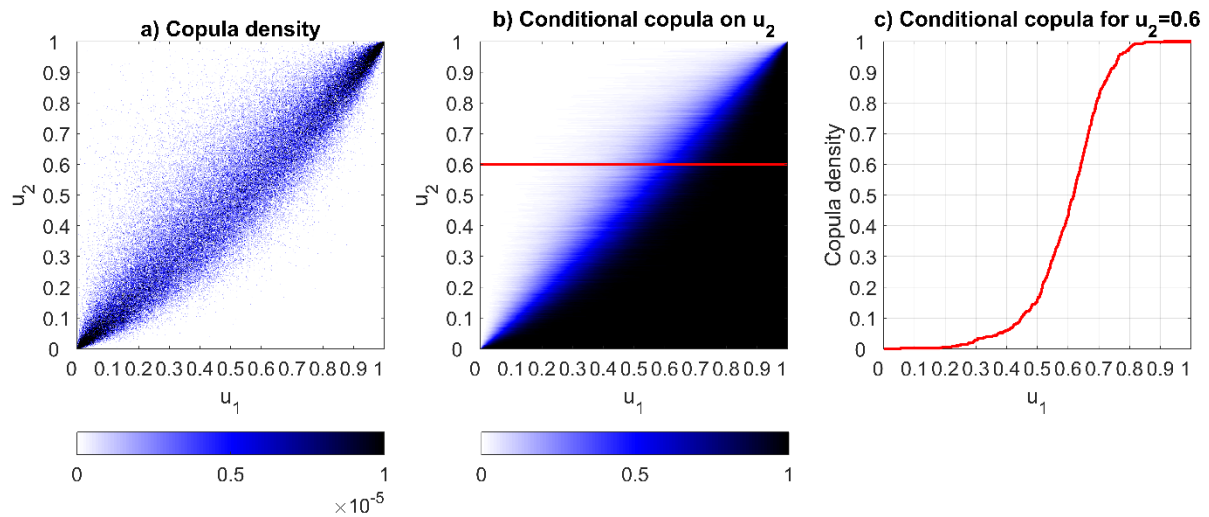
Figure 2-5: a) Copula density for variables u_1 and u_2, b) conditional copula on u_2 obtained from the copula density and c) conditional copula on u_2 for $u_2 = 0.6$.

2.2. Future wave climate

2.2.1. Overview

Accelerated changes in climate have become a global concern during the last years. This motivated the creation of the Intergovernmental Panel on Climate Change (IPCC) in 1988, by the World Meteorological Organization (WMO) and the United Nations Environmental Programme (UNEP). The IPCC has produced a series of reports which show solid evidence of changes in the global climate system during the 21st century, even faster than those observed during the last century (IPCC, 2013).

One of the most important source of information of the IPCC assessments are the outcomes from Global Circulation Models (GCMs). These are numerical models which simulate climate dynamics in response to increasing greenhouse concentrations, taking into account representations of the physical processes in the atmosphere, ocean, cryosphere and land surface (IPCC-DDC, 2013).

The most current publication from IPCC is the fifth Assessment Report (AR5), which was released on 2013 and heavily relies on the fifth phase of the Coupled Model Intercomparison Project (CMIP5, Taylor et al. (2012)), a collaborative climate modeling process coordinated by the World Climate Research Programme (WCRP). CMIP5 constitutes the most updated set of coordinated climate model experiments, comprising several GCMs developed by modeling groups from all over the world.

The CMIP5 projections of climate change are driven by concentration or emission scenarios consistent with the Representative Concentration Pathways (RCPs) described in van Vuuren et al. (2011). According to Taylor et al. (2012), four RCPs have been formulated based on a range of projections of future population growth, technological development, and societal responses. These 4 scenarios are named RCP2.6, RCP4.5, RCP6.0 and RCP8.5, where the labels indicate a rough estimation of the increase of radiative forcing in the year 2100, relative to preindustrial conditions. Therefore, the most severe scenario is RCP8.5, leading to high greenhouse concentration levels. RCP4.5 and RCP6.0 represent two intermediate scenarios, and RCP2.6 includes a mitigation scenario in which radiative forcing reaches a maximum near the middle of the 21st century before decreasing to an eventual nominal level of 2.6Wm^2.

2.2.2. Predictive skills of GCMs

Each GCM is based on a certain spatial resolution and different parameterization of sub-grid processes, thus GCMs produce different results for the same emission forcing scenario. This uncertainty poses the necessity of a methodology to assess the performance of the GCMs in order to select the most appropiate model according to the scope of the research, such as studying changes in climate dynamics or downscaling surface variables, to name a few. Usually, this assessment is undertaken by comparison to historical observations or reanalyses in terms of differences between mean climatologies or probability distributions (Pérez et al., 2015).

Wave climate is not computed explicitly by GCMs and therefore downscaling is needed. Wang et al. (2010) and Laugel et al. (2014) have compared dynamical and statistical wave projections for future scenarios, concluding that the statistical downscaling approach reproduces wave climatology as well as dynamical downscaling, considering mean values, seasonal and interannual scales. Moreover, statistical downscaling based on atmospheric circulation classification (such as weather types) has been succesfully proven to be a sound tool for validation of GCMs (Huth, 2000).

As it was stated, the evaluation of the predictive skills of a GCMs is often undertaken by comparison to reanalysis databases, in order to validate the performance of the GCMs reproducing the historical climate. This analysis can be done in terms of weather types, which takes into account the natural climate variability and allows the evaluation of spatial patterns, as it is shown by Pérez et al. (2014b) or Pérez et al. (2015).

However, future projections cannot be directly validated against observations but different models can be compared to each other, in order to determine the consistency of the projections (Wang et al., 2014). This analysis leads to identify which models may present an anomalous behavior (Pérez et al., 2014b) and therefore their projections should be treated carefully or even not considered.

In this context, Pérez et al. (2014b) made a comparison, based on weather types, between experiments from 42 CMIP5 models. Recent past conditions and the 4 future emission scenarios were considered, in order to assess the performance of the models over the Northeast Atlantic region. The analysis considered 3 factors to be evaluated: 1) the skill of the GCMs to reproduce the synoptic situations, 2) the historical interannual variability and 3) the consistency of the GCMs experiments for the 21st century projections. Results from this work indicate that the most skilled models in the study area are ACCESS1.0, EC-EARTH, HadGEM2-CC, HadGEM2-ES and CMCC-CM (Pérez et al., 2014b).

2.2.3. Changes in future wave climate in front of the central Dutch coast

Recent research has shown that the 1:10,000-yr hydrodynamic boundary conditions in front of the central Dutch coast are not expected to change under climate change scenarios: de Winter et al. (2012) have found no significant changes in H_s and T_m from extreme waves and Sterl et al. (2009) have done the same regarding 1:10,000-yr storm surge levels along the Dutch coast. Furthermore, the work from de Winter et al. (2013) has revealed no significant changes in annual maximum wind speeds, or in wind speeds with lower return periods above the North Sea basin. However, there is evidence that the corresponding wave direction could shift to more westerly directions, because of a poleward shift of the North Atlantic storm track (de Winter et al., 2012; de Winter et al., 2013).

2.3. Coastal sediment transport

2.3.1. Main processes

Coastal morphology is driven by temporal and spatial sediment transport rate gradients. A positive gradient will lead to erosion as the sediment transport rate increases in the direction of transport and conversely, accretion will occur when the sediment transport rate decreases in the direction of transport (a negative gradient) (Bosboom & Stive, 2015).

Besides sea level and tides, waves are one of the main agents driving changes in the sediment transport rates. Two components are easily identified: the cross-shore and longshore sediment transport. In a nutshell, sediment is stirred up by wave orbital motion, making it available to be transported by currents along the shore. These currents can be induced by tides, wind, density differences or wave breaking. Cross-shore sediment transport is related to the wave asymmetry, generating net onshore transport in non-breaking wave conditions outside the surf zone, and net offshore transport under breaking waves (Bosboom & Stive, 2015).

According to van Rijn (1997), the major transport components contributing to the wave-induced transport processes are:

- Net onshore-directed transport due to asymmetry of the near-bed orbital velocities with relatively large onshore peak velocities under the wave crests and relatively small offshore peak velocities under the wave troughs.
- Longshore-directed transport induced by the generation of longshore wave-driven currents due to wave breaking.
- Net offshore-directed transport due to the generation of a net return current (undertow) in the near-bed layers balancing the onshore mass flux between the crest and trough of breaking waves.
- Net onshore-directed transport due to the generation of a quasi-steady weak current (streaming) in the wave boundary layer.
- Net offshore-directed transport due to the generation of bound long waves associated with variations of the radiation stresses under irregular wave groups.

2.3.2. Coastal erosion at the central Dutch coast

The Dutch coast can be divided into 3 subsystems, namely the Delta area in the south, the Holland coast in the center and the Wadden Sea area in the north. The central Holland coast is a sandy, microtidal, inlet-free, wave-dominated coast, bounded by Den Helder in the north and Hoek van Holland in the south, as it is shown in Figure 2-6. The Holland coast system is also compounded by aeolian sand dunes and some minor stretches being reinforced with hard defense structures (Mulder et al., 2011).

Historically, the central Holland coast has suffered from structural erosion due to the combined action of the hydrodynamic forcings, such as waves and tidal currents, and the sediment-importing characteristic of the neighboring tidal inlets (van Rijn, 1997).

Why is so important to prevent coastal erosion in The Netherlands? Because it is a low-lying country, in which 9 million people are living below sea level and 70% of the gross domestic product is being earned in areas below sea level (Mulder et al., 2011). Therefore, the primary function of the coast is to protect the low-lying hinterland from flooding risk. To ensure safety against flooding, in 1990 the Dutch government dictated that the coastline position at that date had to be maintained by all means, by the introduction of the "Dynamic Preservation" policy (van Koningsveld & Mulder, 2004).

This has been achieved by means of sand nourishments (van der Spek & Lodder, 2015) and recently, by a mega-nourishment project referred to as the Sand Engine (Stive et al., 2013).
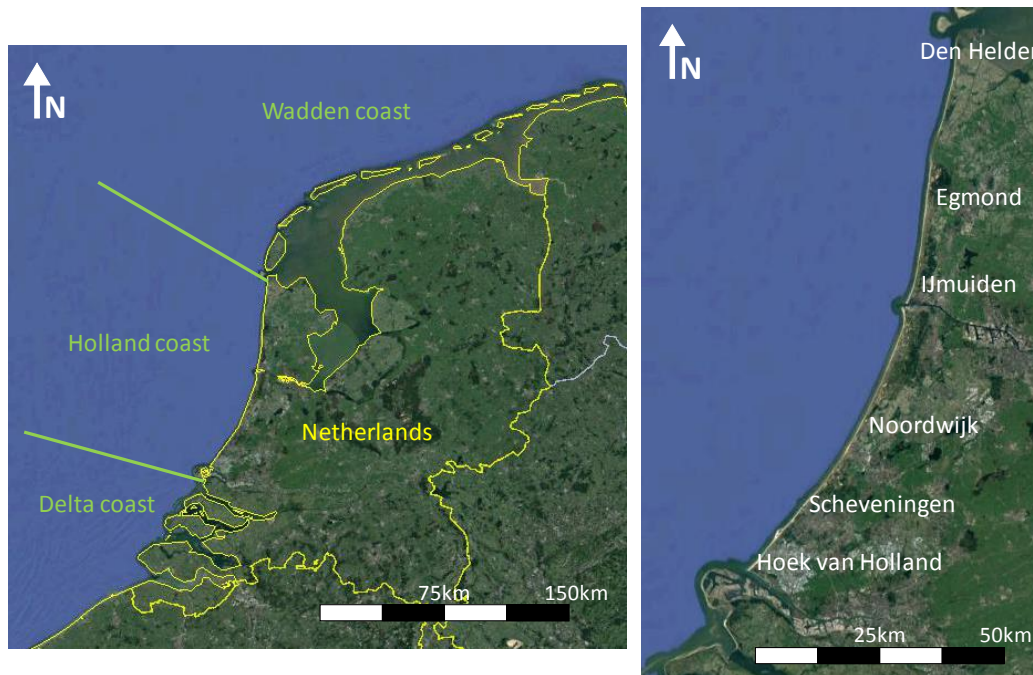

Figure 2-6: Dutch coast and its subsystems (left panel). Central Holland coast (right panel).

Several studies have shown the impact of sea level rise in terms of coastline retreat (Cazenave & Le Cozannet, 2014) and dune erosion (de Winter & Ruessink, 2017), and the rising of sea level may be accelerated under a warmer climate (Katsman et al., 2011). Besides its effect on sea level rise, climate change could also influence the offshore hydrodynamic conditions, such as waves and storm surge levels, and the combined effect with sea level rise would amplify the threat of coastal erosion. In this sense, longshore sediment transport plays an important role in the structural erosion of the central Dutch coast, because the sediment transported alongshore the coast may not be longer available in the system. Moreover, the role of waves in the longshore sediment transport is relevant, as they drive approximately the 80% of the total longshore sediment transport in the central Holland coast (van Rijn, 1997).

2.3.3. Longshore sediment transport in the central Dutch coast

According to the review undertaken by Giardino et al. (2012), two cells can be identified regarding longshore sediment transport along the central Holland coast: from Hoek van Holland to IJmuiden, and from IJmuiden to Den Helder. Due to the presence of the Port of Rotterdam, the yearly-averaged longshore sediment transport has been estimated as zero at Hoek van Holland, increasing up to 500,000m^3/year directed northwards and reducing to zero again due to the presence of the harbor jetties at IJmuiden. In the second cell, the sediment transport along the coast starts at zero and quickly reaches 200,000m^3/year directed southwards at a distance of approximately 30km north to the harbour. Then, the northwards longshore sediment transport increases, reaching up 500,000m^3/year at Den Helder.

In summary, the general trend alongshore the central Dutch coast is northward directed transport, being almost totally blocked by the harbour jetties at IJmuiden. To the north of the port, an inversion of the longshore sediment transport is observed (going southwards), but the general trend is recovered (northwards directed) in about 30km.

The potential shift of wave direction to the more westerly directions under climate change can enhance dune erosion, as it has been demonstrated by de Winter and Ruessink (2017). Subsequently, the change in obliquity of the waves may also have an impact in longshore sediment transport, as wave-induced alongshore currents are determined mainly by wave height and wave angle relative to the shore normal (Bosboom & Stive, 2015).

3. Methodology

3.1. General framework

To fulfill the main objective of this thesis and give answers to the research questions, 3 main units are proposed to be completed as shown in the flowchart of Figure 1-1:

1. Unit 1: Present wave climate
2. Unit 2: Future wave climate
3. Unit 3: Morphological simulation

The different tasks to be carried out in each unit are described in the following sections.

This methodology is applied to Noordwijk, The Netherlands, selected as a representative location of the central Dutch coast according to previous studies (Walstra et al., 2012; Walstra et al., 2013; Walstra et al., 2015).

3.2. Unit 1: Modeling the present wave climate

The goal of this unit is to develop a time-dependent emulator based on a statistical downscaling method which links a multivariate predictand (wave bulk parameters of sea state components from IFREMER reanalysis) with a multivariate predictor (daily representative patterns of sea level pressure from CFSR reanalysis). The statistical downscaling method consists of four main modules, as it is shown in Figure 3-1:

A. Parameterization of data.
B. Statistical model for the predictor.
C. Statistical model for the predictand.
D. Climate-based stochastic simulation.

Following the flowchart of Figure 3-1, the steps comprising each module are described as follows. The corresponding sections from chapter 2 are given in brackets.

A. Parameterization of data

A1. Define the spatial extension of the predictor using the outcomes from the ESTELA model (§2.1.2.1). This step is carried out independently from the rest of the analysis, using as input the wave spectra from the IFREMER reanalysis instead of solely the wave parameters that constitute the predictant.

A2. In this work, sea and swell partitions are explored. For each sea state, 3 sea state types are likely to occur: only sea component or only swell component, corresponding to unimodal sea states, or both simultaneously, referred as a bimodal condition (§2.1.5.1).

B. Statistical model for the predictor

B1. Build the daily predictor as an assembly of the areas of wave generation between the daily isochrones. Principal Components Analysis is applied to reduce the dimensionality of the predictor, retaining a high percentage of the variance (§2.1.2.1).

B2. Apply K-means algorithm to the Principal Components of the predictor to define the daily Weather Types (§2.1.3).

B3. Adjust the chronology model to the observed sequence of weather types (§2.1.4).

C.   Statistical model for the predictand

C1. Obtain the categorical distribution of sea state conditions (unimodals and bimodal) for each weather type. Probabilities of occurrence of each wave condition are estimated from observed wave data (§2.1.5.1).

C2. Fit marginal distributions of H_s, T_p and Dir for the sea and swell partitions, for each weather type (§2.1.6).

C3. Model the dependence between predictand variables for each weather type using a multivariate vine-copula approach (§2.1.8).

D.   Climate-based stochastic simulation

D1. Generate synthetic time series of daily weather types, considering the daily probability of each weather type estimated by the chronology model from module B.

D2. Generate synthetic multivariate sea state parameters (H_s, T_p, Dir) considering the probability of occurrence of the sea state types and the dependence structure between variables for each weather type. The temporal sequence of wave parameters is given by the synthetic time series of weather types generated in the previous step.
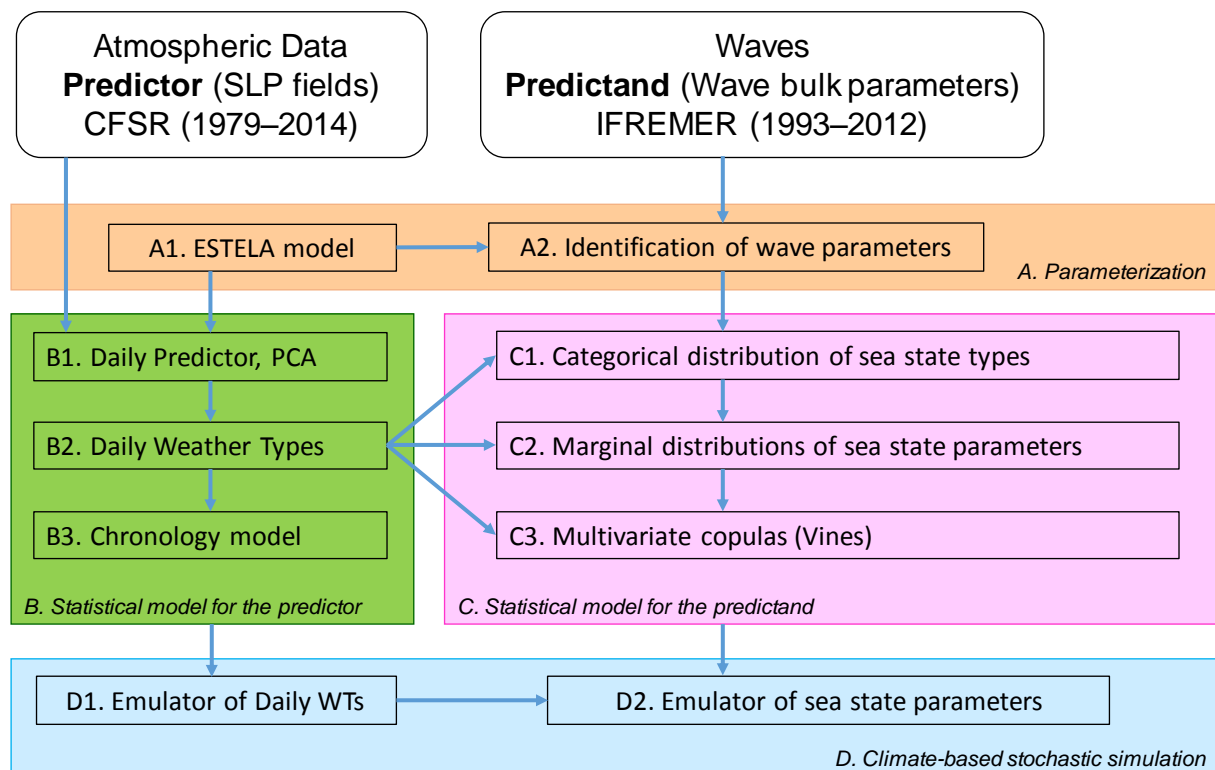

Figure 3-1: Flowchart of the methodology to obtain the time-dependent emulator (adapted from Rueda et al. (2017)).

3.3. Unit 2: Future wave climate

Once the statistical model is validated, the future wave climate is generated. The key assumption for future modeling is that the WT classification is invariant in time, thus it is valid in any future scenario (Pérez et al., 2014b; Wang et al., 2014; Pérez et al., 2015).

In this second unit, the sea level pressure fields are extracted from the outcomes of the GCM ACCESS1.0 (Australian Community Climate and Earth-System Simulator, Collier and Uhe (2012)) developed by the Centre for Australian Weather and Climate Research, a partnership between the Commonwealth Scientific and Industrial Research Organisation and the Bureau of Meteorology (CSIRO-BOM). This model includes a horizontal spacing of 1.25° (Lat) × 1.92° (Lon) and 38 layers in the vertical for the atmosphere, with a daily temporal resolution for the outputs.

SLP fields for the last time slice of the 21st century (2070-2099) and the most severe scenario (RCP8.5) are considered to build the predictor to be used as input for the statistical model.

As it is shown in the flowchart of Figure 3-2, a statistical model for the predictor is obtained using data from reanalysis (CFSR 1979-2014) in the previous unit. As the future predictor comes from a different model, a validation of the GCM ACCESS1.0 for the recent past is required, in order to be confident on the future projections and to guarantee a fair comparison with the present climate. This validation is made at the predictor level, which is the forcer of the climate emulator, and the changes in the future climate forcing will be responsible of the variations in the future wave climate.

The methodology applied for the validation of the ACCESS1.0 model can be summarized as follows:

1. For the recent past, identify the common time slice between the reanalysis (CFSR) and the CMIP5 model.
2. Apply the statistical model for the predictor (box B in Figure 3-1) to ACCESS1.0 data for the common time window.
3. Compare both statistical models for present predictors and validate the model if the agreement is acceptable.
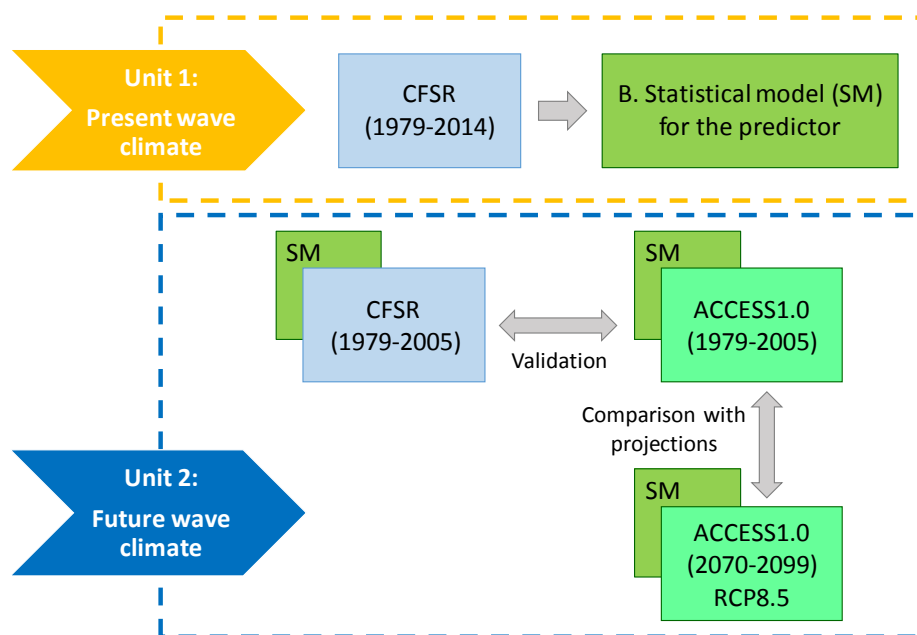

Figure 3-2: Flowchart of the methodology to quantify changes under climate change.

As the statistical relationship between predictor and predictand has been established using the weather types from the CFSR reanalysis data, projecting data from any other model into the weather types from CFSR must always be conducted in order for the statistical relationship to remain valid (Pérez et al., 2015).

In practical terms, applying the statistical model for the predictor means assembling the daily predictor from the data and then project it to the EOFs from CFSR data, which are obtained from the Principal Components Analysis applied in Unit 1. Then, the obtained PCs are clustered using KMA and the centroids from CFSR. Finally, new prototypes are estimated as the closest data value to the average over the whole data in each cluster, leading to a new set of weather types associated to the ACCESS1.0 predictor. If CFSR data and ACCESS1.0 data for the common period were exactly the same, then the weather types from both models would be identical, but of course, some differences are expected.

Finally, the chronology model is trained using the sequence of weather types from the ACCESS1.0 model in order to generate the transition probability matrix and estimate the persistance of each weather type.

Should the set of weather types for ACCESS1.0 predictor look similar to the ones obtained for the CFSR data and the agreement between the chronology models for both predictors be acceptable, then the GCM ACCESS1.0 is validated and therefore can be used as a predictor for future scenarios. Nevertheless, a robust predictor for climate change should cover the climate model uncertainty, taking into account an ensemble of the different CMIP5 GCM models [i.e., Pérez et al. (2015)].

Once the CMIP5 model has been validated, evaluation of the impact of climate change is undertaken in terms of changes of the relative frequency of each of the weather types that are calculated for the present. Another comparison can be undertaken in terms of the chronology model, which is trained again using the future predictor to identify potential changes in the transition probability matrixs and the persistance associated to each WT.

3.4. Unit 3: Morphological modeling

The third and final unit is related to the morphological modeling. Longshore sediment transport at Noordwijk will be used as a metric of the changes induced by climate change by the end of the 21st century. In order to quantify these changes, a simplified approach will be followed:

1. Calculate the wave-induced longshore sediment transport using the wave time series from IFREMER reanalysis.
2. Validate the computed longshore sediment transport by comparison with values from literature and the longshore sediment transport estimated using wave time series from two measurement stations in the area of interest.
3. Compute the distribution of longshore sediment transport for each weather type. The 20-year wave time series from IFREMER reanalysis is considered as the offshore hydrodynamic boundary condition for the process-based model in order to calculate the longshore sediment transport associated to each sea state. Then, the time series of longshore sediment transport is grouped into the weather types, according to the sequence of WTs from CFSR reanalysis.
4. Estimate the yearly-averaged total gross and net longshore sediment transport weighting the previously computed longshore sediment transport distributions by the occurrence probability of each weather type and integrating over all the weather types. Assuming that weather types from CFSR reanalysis and ACCESS1.0 model are the same, WT probabilities from CFSR and ACCESS1.0 for the recent past will be used to compare the longshore

sediment transport and validate the ACCESS1.0 data. Afterwards, probabilities for the future scenario will be considered in order to estimate the projected longshore sediment transport. Changes in gross values associated to each weather type and in the total gross and net longshore sediment transports will be quantified, in order to determine the effect of the climate change.

The process-based model Unibest-TC has been chosen to estimate the wave-induced longshore sediment transport at Noordwijk, because its consumption of computational resources is relatively low, allowing to run several cases in short amounts of time. Other morphodynamic models are available, like Delft3D, but they are very expensive in computational terms and some techniques like input reduction are required to speed up the calculations. As a first approach to the research topic, no input reduction will be considered in order to test the applicability of the statistical downscaling in the area of interest.

3.4.1. Unibest-TC

Unibest-TC is a cross-shore profile model and comprises coupled, wave-averaged equations of hydrodynamics (waves and mean currents), sediment transport, and bed level evolution. Straight, parallel depth contours are assumed. Starting with an initial, measured cross-shore depth profile and boundary conditions offshore, the cross-shore distribution of the hydrodynamics and sediment transport are computed. Transport divergence yields bathymetric changes, which feed back to the hydrodynamic model at the subsequent time step, forming a coupled model for bed level evolution (Walstra et al., 2012).

The model computes the cross-shore distribution of longshore and cross-shore sediment transport, distinguishing between bed load and suspended load transport. The bed load formulations are driven by the instantaneous velocity signal, while the suspended transports are based on an integration over the water column of the sediment flux. The instantaneous velocity signal is computed using a phase-averaged wave model extended with a roller model, for the oscillatory wave motion, combined with the vertical distribution of the advective currents induced by wave-averaged local wave forcing, mass flux, tide and wind forcing (Walstra et al., 2015).

For a detailed description of the formulations included in the model, the reader is referred to Ruessink et al. (2007).

4. Weather-type based wave climate modeling

This chapter presents the results obtained following the methodology described in §3.2.

4.1. Predictor

4.1.1. Spatial extent

As it was stated in §2.1.2, the Sea Level Pressure (SLP) fields and the square of the SLP gradients (SSLPG) from the SLP fields are considered to build the predictor at daily scale. The SLP fields are extracted from the outcomes of the Climate Forecast System Reanalysis (CFSR) (Saha et al., 2010), spanning from 1979 to 2014 (36 years) with hourly resolution.

The outcomes from the ESTELA model are considered to define the spatial domain of the predictor. The node located at 52.5N 4.0E (hereafter "Noordwijk", selected for the definition of the predictand as explained in §4.2) was defined as the target location. The ESTELA method computes the wave energy flux, group velocity and energy losses from spectral reconstruction at each source point using wave spectra from the IFREMER reanalysis. Figure 4-1 shows the effective energy flux reaching the target location at Noordwijk and the corresponding average travel time (in days) of the wave energy. The ESTELA maps reveal an important area of swell generation from the Greenland Sea and the Norwegian Sea, and a second generation area of waves arriving to Noordwijk within 1 day. Almost the whole North Sea lays in this local area, where a high generation area is observed towards the English Channel in the right panel of Figure 4-1. This configuration suggests that bimodality may be important when characterizing the wave climate at Noordwijk, with a swell component coming from the North and a sea component arriving from the West.
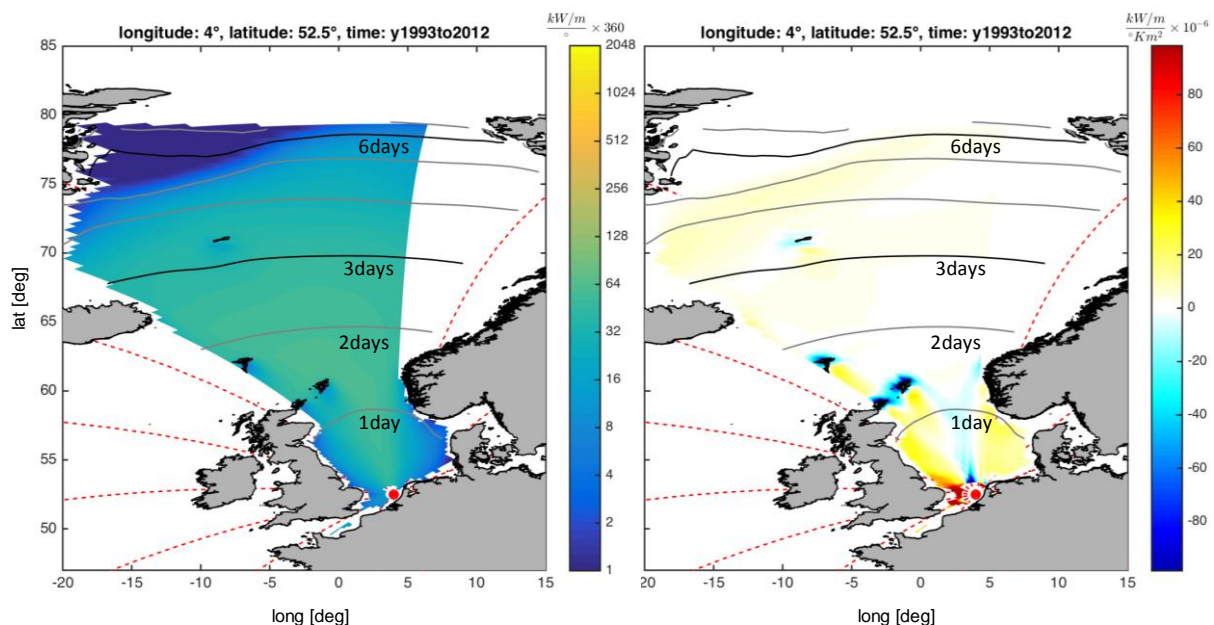

Figure 4-1: Results from ESTELA model: effective energy flux at source points for target location at Noordwijk (left panel). Gain/loss of energy flux for the target point at Noordwijk (right panel). Travel time (in days) is represented in black and gray lines.

4.1.2. Definition

Firstly, the daily mean SLP fields are computed and the square of the hourly SLP gradients are averaged over one day. Then, following Hegermiller et al. (2017), the daily predictor is assembled taking into account the area between the isochrones. For the day t, SLP and SSLPG fields located inside the isochrone of 1 day are put together with the data from the day $t-1$ located between the isochrones of 1 and 2 days. Then, the data from day $t-2$ located between the isochrones of 2 and 3 days is assembled and so on, until the area defined by the last isochrone is considered in the predictor, which represent the longest possible wave propagation time from generation until reaching the target location. A schematization of this procedure is depicted in Figure 4-2.
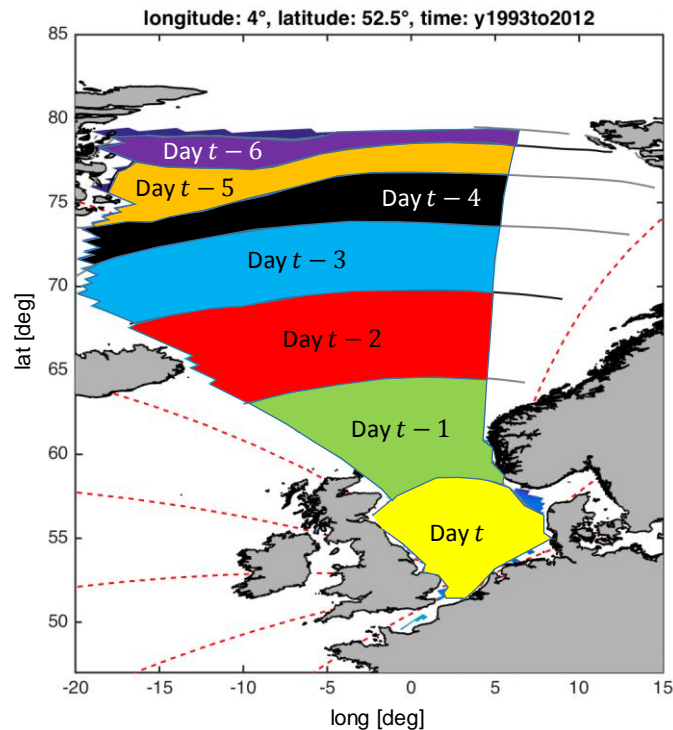
Figure 4-2: Definition of the predictor.

2,190 grid points from CFSR with atmospheric data lay inside the area defined by the ESTELA model, thus the daily predictor is made up of 4,380 variables: 2,190 nodes for the SLP and the same number for the squared SLP gradients. The time series of the daily predictor spans for 36 years, from 1979 to 2014.

4.2. Predictand

Twenty years of wave data, from 1993 to 2012, are extracted at the node located at 52.5N 4.0E (hereafter "Noordwijk") from the global wave reanalysis carried out by IFREMER (Rascle & Ardhuin, 2013), described in §2.1.5.2. The database consists of sea states every 3 hours, including variables such as significant wave height H_s, peak period T_p and mean wave direction Dir for up to 6 partitions of the wave spectrum: the wind sea and five swell trains in the more general case. Under this definition, swell waves aligned with the wind direction are classified as wind sea in this wave reanalysis.

Wave bulk parameters (H_s, T_p, Dir) are calculated from the reanalysis in order to compare them to measurements taken at the YM6 station from Rijkswaterstaat. Location of both the IFREMER wave node and YM6 station is shown in Figure 4-3.

A comparison between measured values at YM6 and hindcasted values from the reanalysis for H_s, T_p and Dir is given in Figure 4-4. Scatter of measured and hindcasted values shows a good agreement, based on a high correlation coefficient (given at the bottom right of each panel). However, as can be seen in the plots, the IFREMER data overestimates the most energetic sea states (cf. left panel of Figure 4-4) and the IFREMER wave directions are biased northwards (cf. right panel of Figure 4-4).
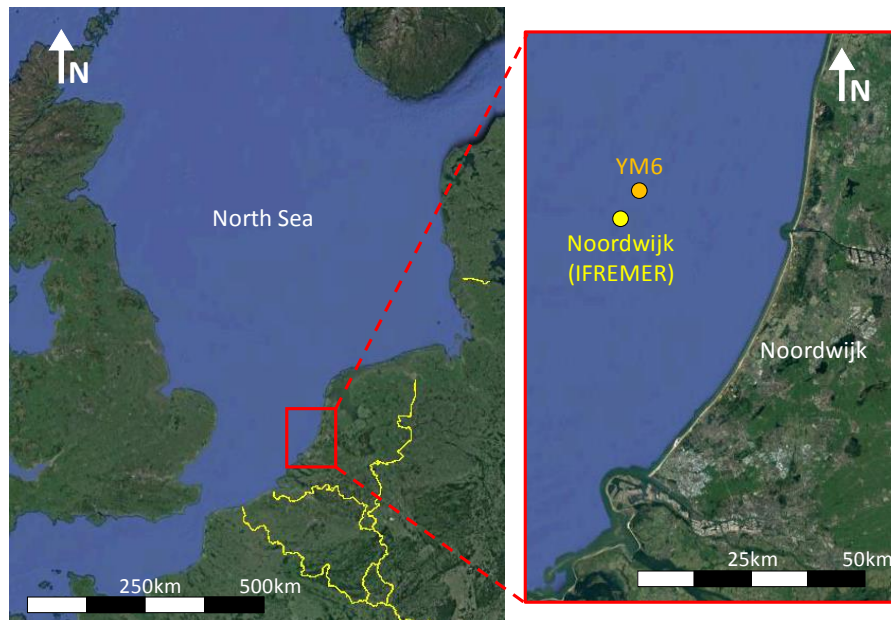
Figure 4-3: Location of wave node and measurements.
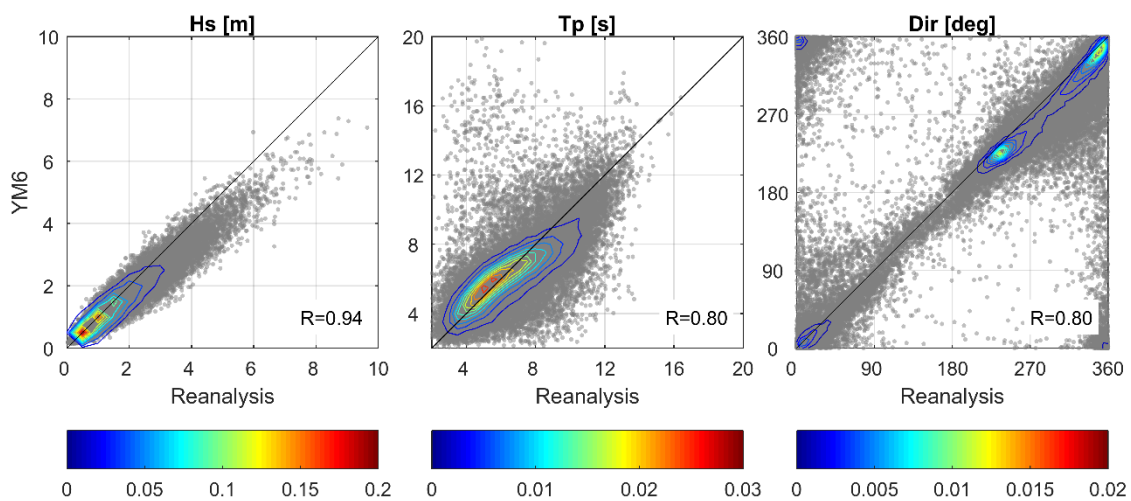
Figure 4-4: Scatter plots of measured and hindcasted values of H_s, T_p and Dir. Correlation coefficient between variables is given at bottom right of each panel. Data density is shown by colored contours.

Relation between measured and hindcasted time series can also be analyzed comparing wave roses of H_s and T_p, as it is depicted in Figure 4-5. In both datasets, two main directions can be identified: waves coming from N and from SW, which are coherent with the generation areas recognized in the outcomes of the ESTELA model. Distributions of H_s and T_p along the directions are similar between measured and hindcasted values, with a larger fraction reaching from N according to the reanalysis.
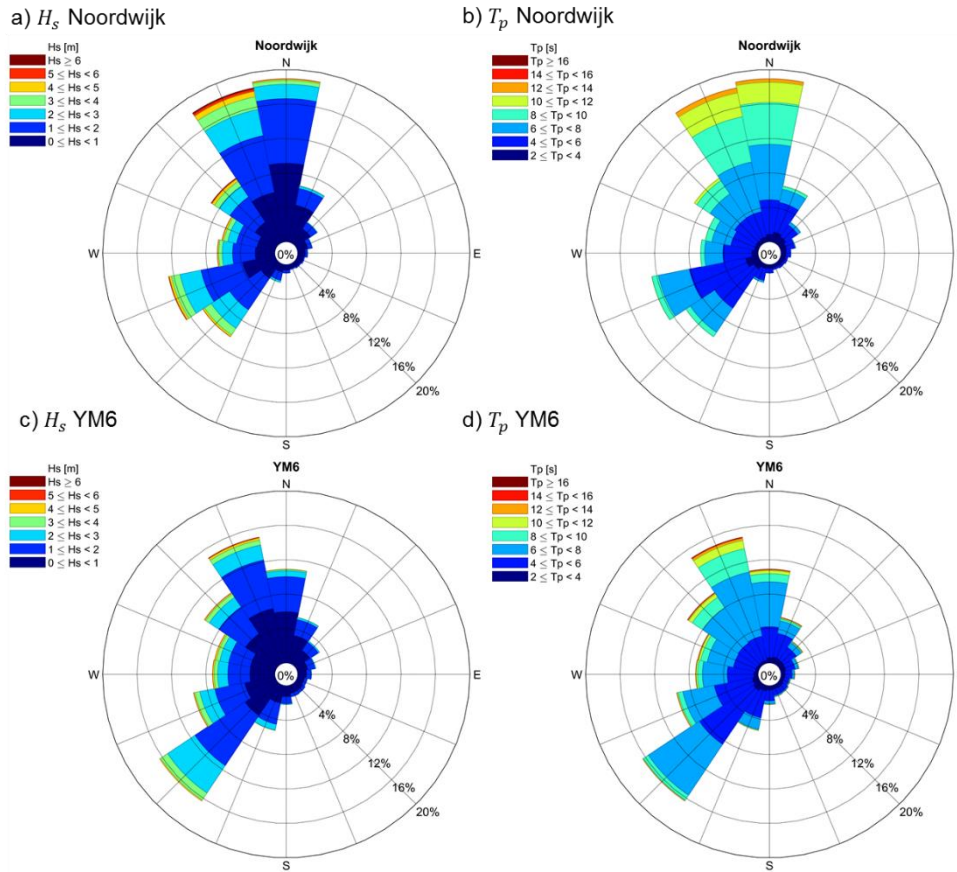

Figure 4-5: Wave roses of H_s and T_p at Noordwijk (IFREMER node, top panels) and observations at YM6 measurement station (bottom panels).

As the ESTELA maps and the wave roses suggest, considering the wave climate at Noordwijk as bimodal may be a more realistic representation than using bulk parameters. For the scope of this work, the swell component is reconstructed from the available partitions using the following expressions (Holthuijsen, 2007):

Significant wave height $H_{s_{swell}}$:

$$H_{s\,swell} = \left(\sum_i H_i^2 \right)^{0.5}$$

(4-1)

Where H_i denotes the significant wave height of swell partition i [m].

Energetic period $T_{e_{swell}}$:

$$T_{e\,swell} = \frac{\sum_i H_i^2}{\sum_i H_i^2 / T_i} \tag{4-2}$$

Where T_i denotes the period of swell partition i [s].

Mean wave direction Dir_{swell}:

$$Dir_{swell} = \text{atan}\left(\frac{\sum_i E_{x_i}}{\sum_i E_{y_i}}\right) \tag{4-3}$$

Where E_i represents the energy of swell partition i, defined as $E_i = \frac{1}{4}\rho g H_i^2$ [J] with ρ denoting the water density and g the acceleration of gravity.

Wave roses for the sea and swell partitions are shown in Figure 4-6, which confirm the results already presented: the North Sea corresponds to a local wave generation area, with higher waves coming from the English Channel and from the Norwegian Sea, and SW – WSW as the prevailing directions. Regarding the swell component, NNW and N are the dominant directions, corresponding to the generation area located north of the North Sea. In the swell partition, easterly waves with small H_s and large T_p are observed, which may correspond to residual energy from wind seas coming from the Danish coasts, identified as swell component by the post-processing algorithm of the reanalysis. Therefore, these easterly waves are considered spurious as these large periods are not identified in Figure 4-5.
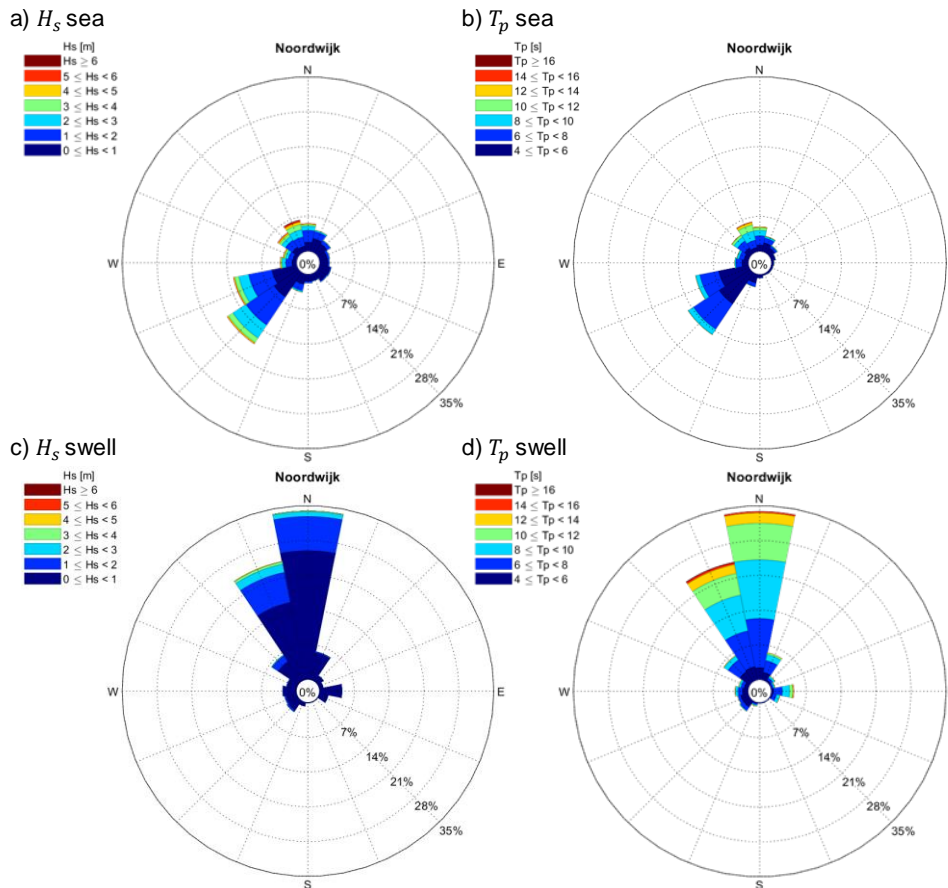

Figure 4-6: Wave roses of H_s and T_p for sea and swell partitions at Noordwijk.

4.3. Weather Types

K-means algorithm (KMA) (Camus et al., 2011c) is applied to the first 52 Principal Components (PCs), as it is explained in Appendix A. The data is grouped in a set of 49 weather types, where the centroids representing each cluster correspond to the closest value to the average over all the data in each cluster. The centroids are shown in the lattices of Figure 4-7. In the left panel, low-pressure systems are depicted on blue color scale and high-pressure systems are presented on a red color scale, where a reference mean SLP pressure of 1,010hPa has been calculated from the available data. Although WTs are presented as SLP fields, it is important to emphasize that each WT does not correspond to a stationary system but they are a representation of the atmospheric dynamics because of the way the predictor is assembled, considering the information from up to 7 previous days.

WTs located at the left on the lattices are characterized by low-pressure systems dominating the whole domain, with different locations of the center of the system. The inverse situation is observed on the top right and bottom center of the lattice, where WTs corresponding to high-pressure systems are located. The rest of the lattice consists of mixed-type WTs, where high and low-pressure systems coexist, varying the location of the center of each system.

Right panel of Figure 4-7 shows the square of the SLP gradients for each weather type. Areas with stronger gradients are responsible of the generation of more intense winds as it was stated in §2.1.2. This information allows to distinguish between weather types that look very similar when are represented as SLP fields, see for instance WT1 and WT8, or WT6 and WT7.

KMA depends on the initial set of centroids given to the algorithm. In order to become independent from the initial seed, 100 random initializations were run and then the average over the 100 samples was selected as the most representative set of prototypes.
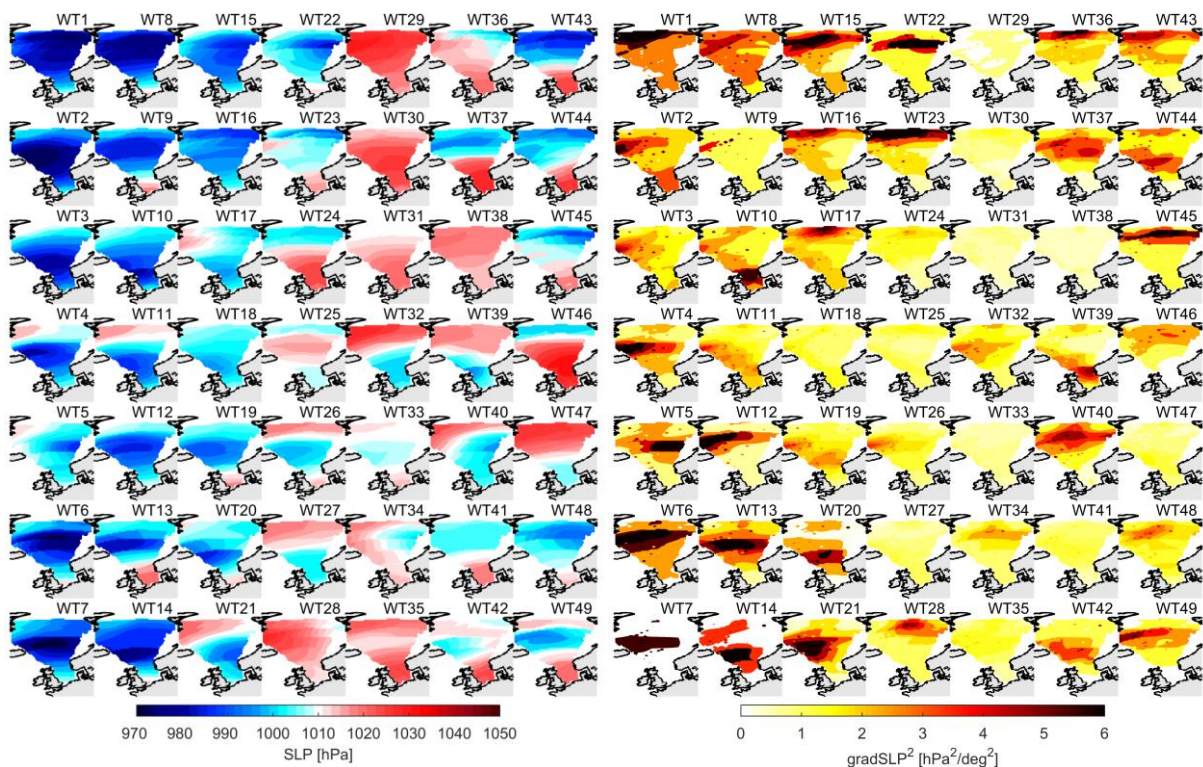

Figure 4-7: 49 Weather Types represented as SLP fields (left panel) and as the square of the SLP gradients (right panel), obtained for Noordwijk using KMA.

Under the KMA classification, the time series of the predictor is translated to a time series of WTs, which represent the historical realization of the climate.

Figure 4-8 shows the occurrence probability of each WT at different time scales. Panel b) presents the probability of occurrence of the WTs estimated over the whole period available (1979-2014), showing that the 49 WTs are present during the 36 years of data, being WT 38, WT 33 and WT 31 the most probable ones. The same analysis but at seasonal and monthly scale reveals that during the summer, not all the WTs are likely to occur, especially the ones related to low-pressure systems.

The number of WTs is selected aiming to ease the implementation, fitting and interpretation of the model results. The procedure undertaken to determine the number of 49 weather types is presented in Appendix B.
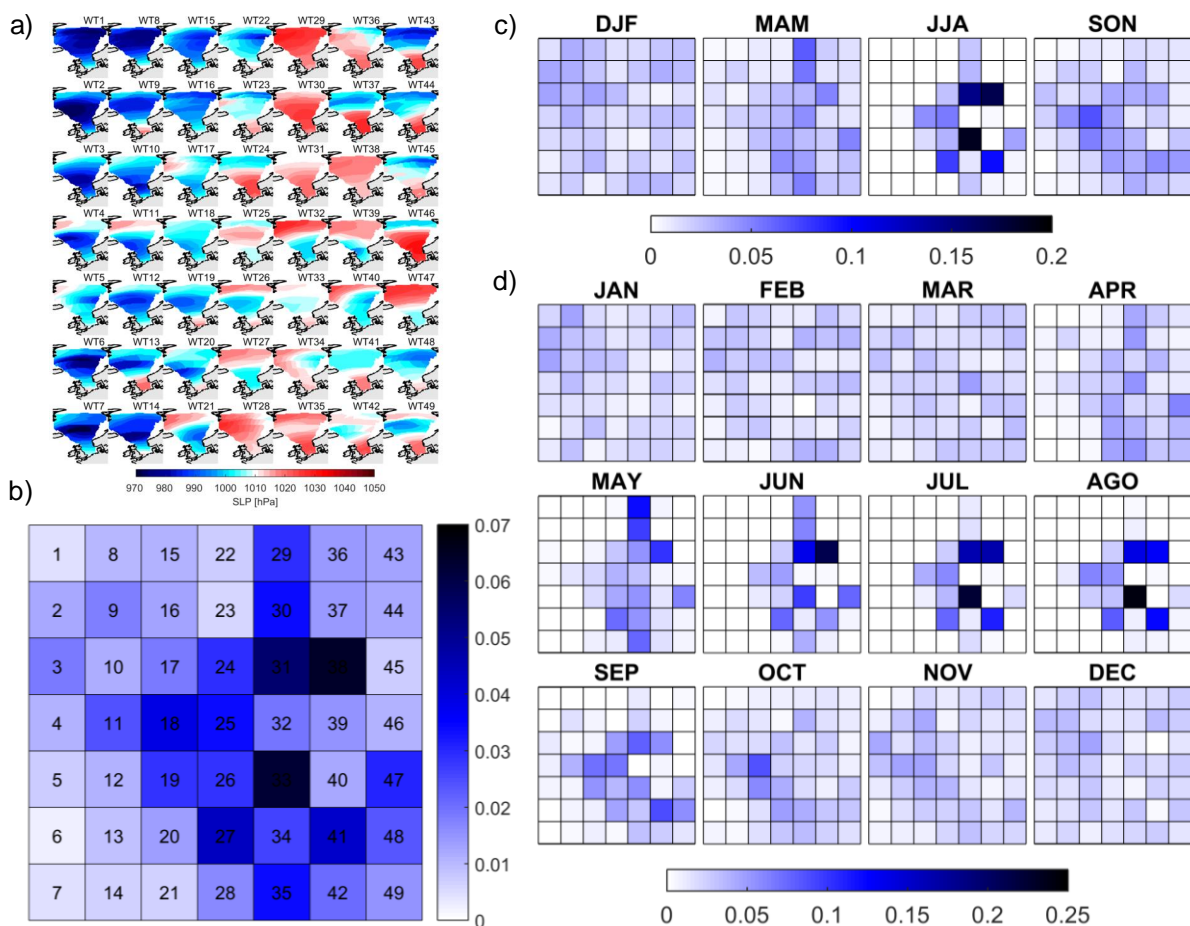

Figure 4-8: a) Set of 49 weather types, b) occurrence probability of WTs over the whole period (1979-2014), c) occurrence probability of WTs at seasonal scale and d) occurrence probability of WTs at monthly scale.

4.4. Chronology of weather types

As it was stated, the time series of the predictor is translated to a time series of WTs under the KMA classification. The collection of 49 WTs represent a categorical variable and the occurrence sequence can be modeled with the Autoregressive Logistic Regression (ALR) model described in §2.1.4.

Figure 4-8 reveals that seasonality must be included in the chronology model for a proper representation of the WT sequence. Therefore, seasonality terms and a Markov chain of order 1 are included in the ALR model, and the parameters are obtained fitting the model using the 36 years of

data. The autorregresive term is introduced to model the persistence of each WT, which is an indicator of the weather dynamics.

Figure 4-9 shows the daily probabilities of each WT within a year, where the colorbars represent cumulative probabilities of occurrence of all the 49 WTs, which are calculated for each day using the 36 values associated with each year. Panel b) presents the cumulative probabilities estimated from fitting the model and panel c) shows the empirical cumulative probabilities within a year for the WTs. The seasonality within the year is clearly captured by the model, where some WTs are more likely on summer (WT 25 to WT 43), while WTs located on the left of the lattice (WT 1 to WT 14) occur during the winter, as it was indicated in Figure 4-8.
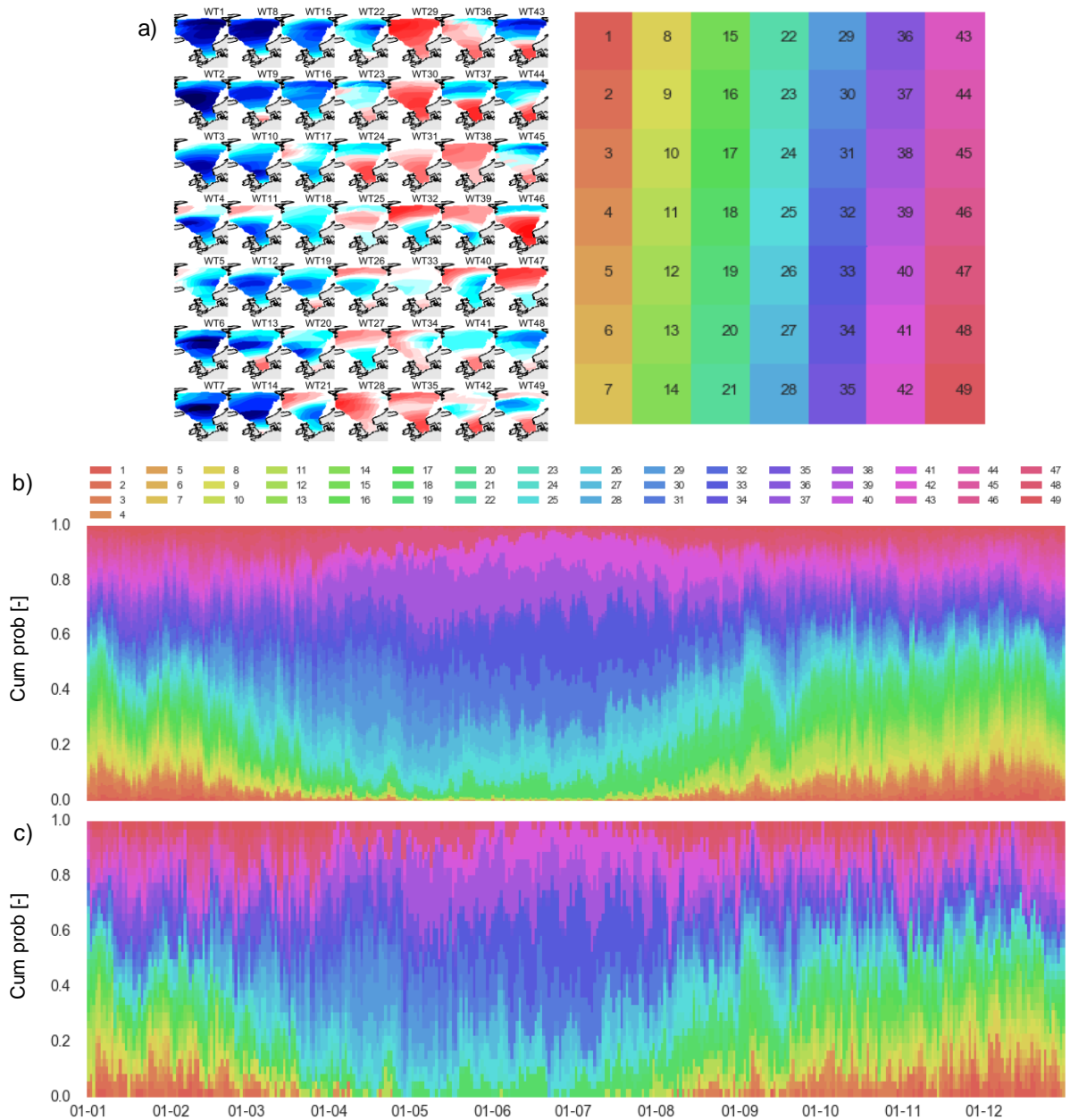

Figure 4-9: a) WTs and corresponding color. b) cumulative probabilities of each WT within a year from model fitting. c) empirical cumulative probabilities of each WT within a year.

4.5. Categorical distribution of sea state types

Following Rueda et al. (2017), the sea state type is represented as a random vector I, which is a sequence of 2 Bernoulli trials:

$$\left. \begin{array}{l} I_{sea} = B(p_{sea}) \\ I_{swell} = B(p_{swell}) \end{array} \right\} I = \{I_{sea}, I_{swell}\} \tag{4-4}$$

Where I_i denotes the occurrence probability of sea state i, with $i = \{sea, swell\}$.

The sample space consists of 4 tuples, $S = \{00, 10, 01, 11\}$, although the event of no waves (00) is highly unlikely, if not impossible. Removing this event, the random variable I follows a categorical distribution with 3 possible outcomes $\{10, 01, 11\}$ conditioned to each weather type. This means that, for each weather type, two unimodal sea states of only sea or only swell and one bimodal sea state are possible.

Figure 4-10 shows the occurrence probabilities of the sea state types for each WT, estimated from the 3-hourly wave time series at Noordwijk. The predominance of the bimodal sea state (referred as "combined") is clearly observed for all the WTs, with probabilities of occurrence larger than 50% of the time. The unimodal sea states share the rest, with a tendency of larger probabilities for the swell in most of the WTs.
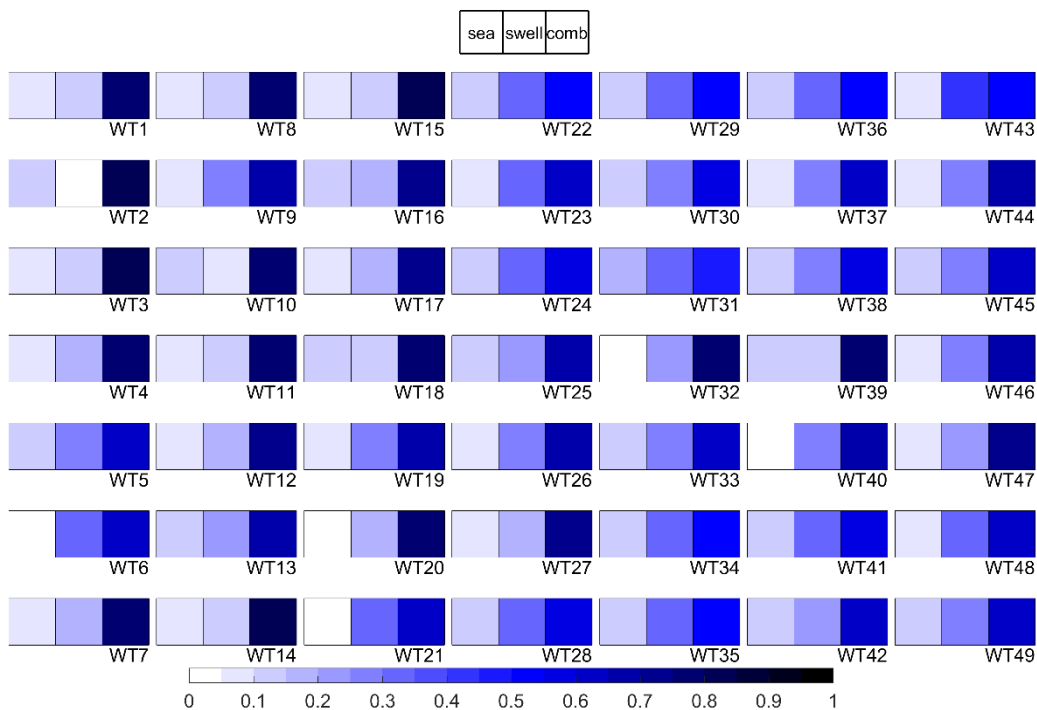

Figure 4-10: Occurrence probability of sea state types for each WT.

4.6. Marginal distributions of sea state parameters

Every sea state corresponds to a multivariate random variable. In the case of unimodal sea states, three variables are relevant: significant wave height, peak period and mean wave direction, while in the bimodal case the number of variables is doubled (3 variables for sea and the same 3 for swell). Accordingly, the multivariate random variable is defined by the joint distribution of the relevant

variables. To model this joint distribution, the first step is obtaining the marginal distributions of each variable associated to each WT.

4.6.1. Marginal distributions of significant wave height and peak period

For H_s and T_p, the marginal distributions are obtained from a mixed model, which consists of a truncated central distribution representative of the central or main-mass regime and two generalized Pareto distributions for the maximum and minimum regimes, representing the upper and lower tails, respectively (Solari & Losada, 2012). The central distribution corresponds to a non-parametric kernel density function (Athanassoulis & Belibassakis, 2002), with a threshold for upper and lower tails of 0.9 and 0.1, respectively. This approach is chosen because it improves the fitting of the upper tail, compared to other distributions, as is explained in Appendix C.

The fitting of the mixed model to the empirical data is shown in the following figure for $H_{s_{sea}}$, and in Appendix C for $T_{p_{sea}}$, $H_{s_{swell}}$ and $T_{p_{swell}}$, respectively. The figures correspond to probability plots, where the vertical axis indicates the cumulative probability, the blue dots correspond to the empirical cumulative probability and the red lines depict the distributions from the mixed model associated to each WT.

These probability plots are tailored for each weather type, explaining the different vertical axes in each panel. It can be seen that for all the variables, the central regime is well represented by the kernel density function, and the match between the fitted GPD and the data is acceptable in the lower and the upper tail of each WT.
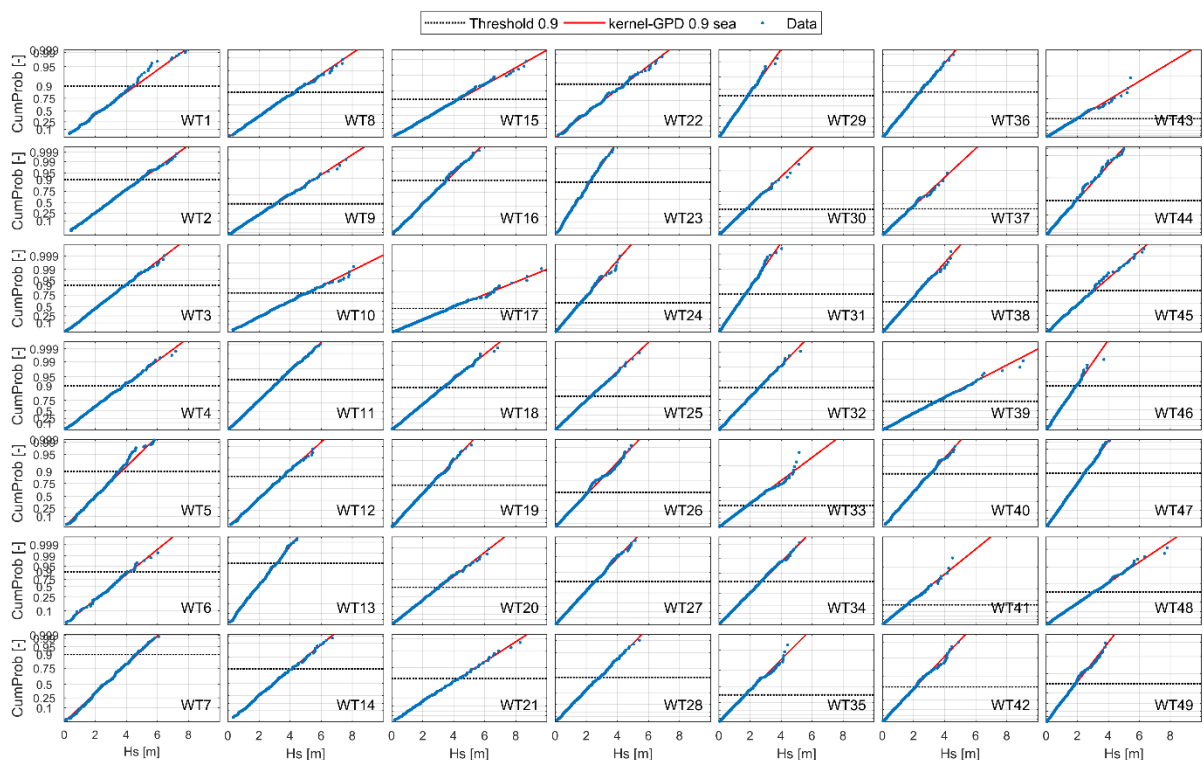

Figure 4-11: Probability plots of the empirical and fitted marginal distributions of $H_{s_{sea}}$ associated to each WT.

Another way to present the marginal distributions obtained for the wave parameters corresponds to the cumulative density functions (CDFs). The following figures aim to compare the fitted and

empirical marginal distributions related to each WT, showing the good match between the distributions.
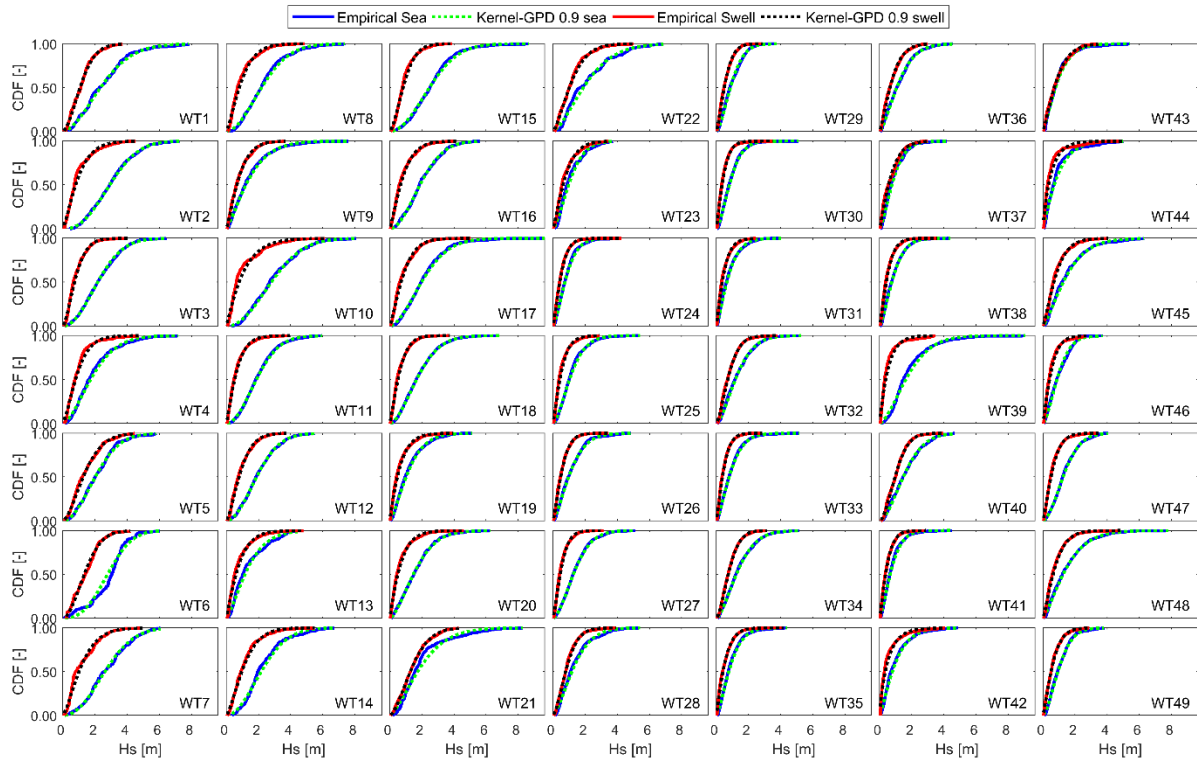

Figure 4-12: Empirical and fitted marginal distributions of H_s for sea and swell associated to each WT.
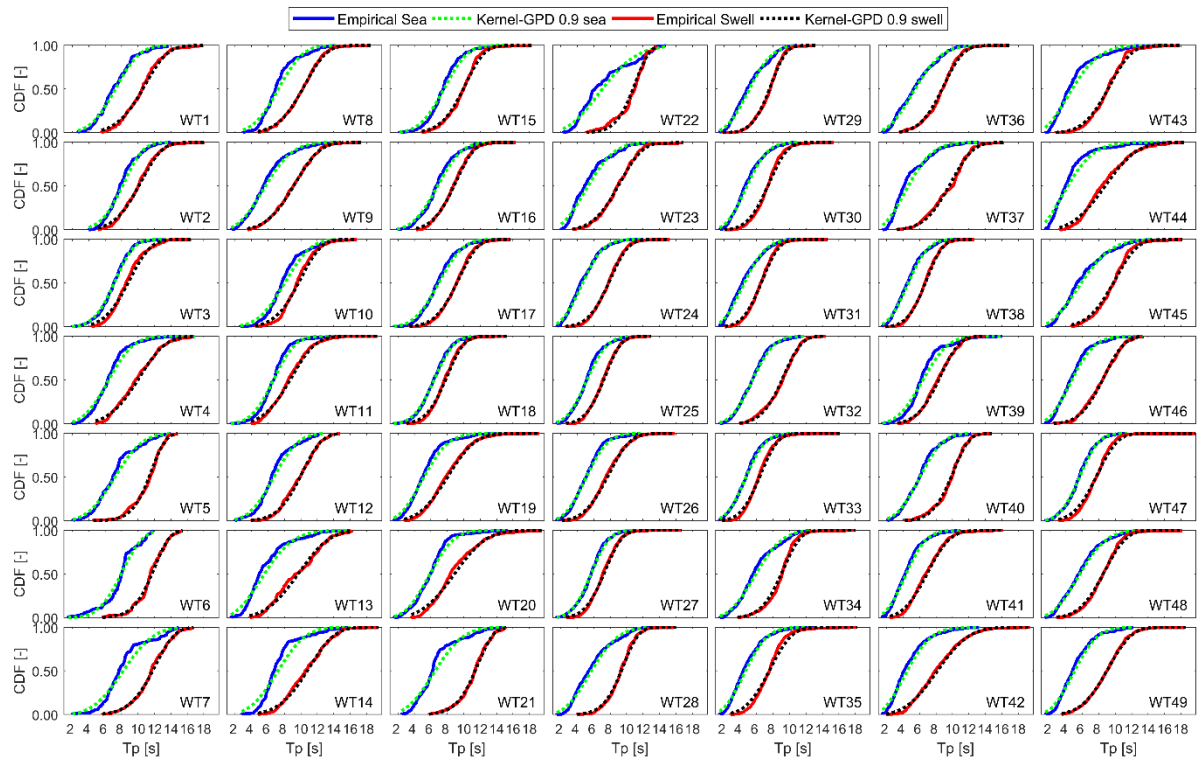

Figure 4-13: Empirical and fitted marginal distributions of T_p for sea and swell associated to each WT.

4.6.2. Marginal distribution of mean wave direction

For the mean wave direction, the empirical distributions are considered. They are shown in Figure 4-14. It can be seen that the swell component is always coming from the north in all the weather types, while the sea component has a predominant south-westerly direction when low-pressure systems are dominant (left side of the lattice), although a fraction of the sea component is coincident with the swell in some weather types. Conversely, this predominance is lost when a high-pressure system is located in the North Sea, as it can be seen in the right side of the lattice from the following figure.

Easterly swell component identified in §4.2 is observed in some weather types located at the left side of the lattice, but these waves are thought to be spurious, caused by issues in the post-processing of the IFREMER data.
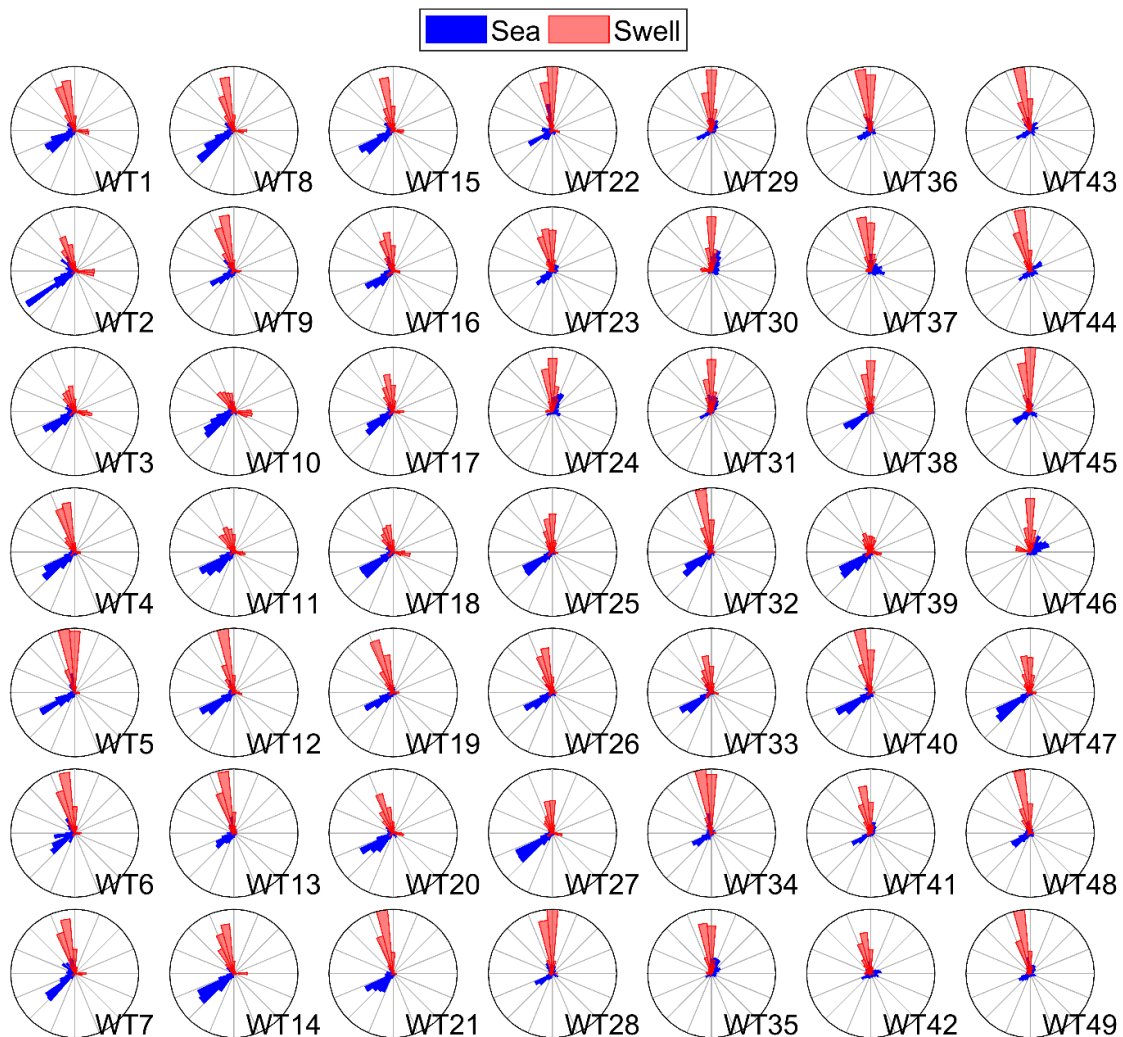

Figure 4-14: Empirical PDF for mean wave direction.

4.7. Multivariate copulas

Wave parameters are usually strongly correlated to each other, and this interdependence can be captured using a multivariate copula. Following Rueda et al. (2017), the joint distributions of H_s, T_p and Dir can be adequately represented using a multivariate Gaussian copula. For unimodal sea

states, the copula has 3 variables and this number is doubled in the bimodal case. This copula can be easily implemented using the multivariate Gaussian distribution.

The recent work of Jäger and Morales Nápoles (2017) has shown that the AC skew-t copula provides a better representation of the bivariate distribution of H_s and T_p, preserving the limiting wave steepness condition. In order to include this copula in the dependence model, a vine-copula approach is proposed, where the bivariate relation between H_s and T_p is modeled using the AC skew-t copula and all the remaining bivariate relations between parameters are considered to be Gaussian.

The general procedure to model the multivariate dependence structure comprises the following steps:

1. Estimate the correlation parameters for the wave variables for all the sea states types.
2. Fit a AC skew-t copula for the pair $H_s - T_p$ for each sea state type.
3. Draw the D-vine for each sea state mode. Among the different types of vines, a D-vine was selected in this thesis in order to ease the implentation of the vine and the sampling procedure.
4. Calculate the partial correlations that define the D-vine and identify the sampling structure.

4.7.1. Correlation between variables

For a unimodal sea state, the rank correlation coefficients between variables can be grouped in the so-called correlation matrix:

$$\Omega = \begin{bmatrix} 1 & \rho_{12} & \rho_{13} \\ \rho_{21} & 1 & \rho_{23} \\ \rho_{31} & \rho_{32} & 1 \end{bmatrix} \tag{4-5}$$

Where ρ_{ij} is the rank correlation between variables i and j, with $i \neq j$. Subindices $i,j = 1,2,3$ represent the variables H_s, T_p, Dir respectively.

In the bimodal case, the subindices $i,j = 1, \dots, 6$ are linked to the variables $H_{s_{sea}}, T_{p_{sea}}, Dir_{sea}, H_{s_{swell}}, T_{p_{swell}}, Dir_{swell}$ respectively and therefore Ω is a 6x6 matrix.

Spearman's rank correlations between observed variables in the unimodal cases are calculated over the whole available data, regardless whether the sea state belongs to a bimodal sea state, in order to provide enough data for the calculation. On the other hand, the Spearman's rank correlations for the bimodal case are computed considering only the simultaneous presence of sea and swell.

Figure 4-15 depicts the Spearman's rank correlations between observed variables estimated for the bimodal case, while the same variables for the unimodal cases are presented in Appendix D. In the figure, positive and negative rank correlations are depicted in cyan and magenta lines, respectively.

As expected, strong positive correlation is observed between $H_{s_{sea}}$ and $T_{p_{sea}}$ in all the weather types for the combined sea state, and the correlation between $H_{s_{swell}}$ and $T_{p_{swell}}$ is much weaker. In general, the figure reveals the interdependence between the variables, especially for the combined sea state, emphasizing the importance of considering the dependence structure in the statistical model.

Although each weather type has its own particular pattern, some similarities can be identified. For the bimodal case, there is a positive correlation between $T_{p_{sea}}$ and $T_{p_{swell}}$ in the WTs from the upper

part of the lattice, while in the bottom left this correlation is almost zero or even negative (see WT6 or WT21).
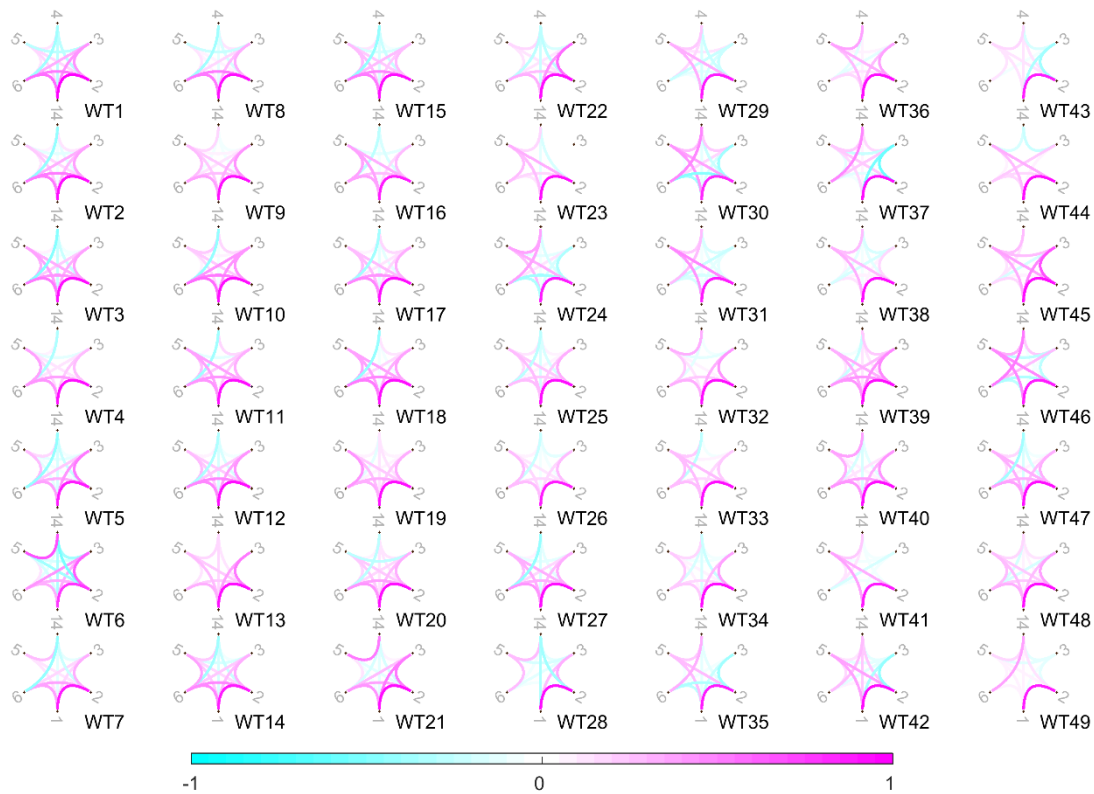

Figure 4-15: Graphical representation of rank correlation coefficients for the bimodal sea state associated to each WT. Numbers from 1 to 6 stand for $H_{s_{sea}}, T_{p_{sea}}, Dir_{sea}, H_{s_{swell}}, T_{p_{swell}}, Dir_{swell}$ respectively. Color scale is defined between -1 (cyan) for negative correlation, 0 (white) for no correlation and 1 (magenta) for positive correlation.

4.7.2. AC skew-t copulas

Four sets of AC skew-t copulas are estimated: one for each unimodal sea state, and two more for the sea and swell components under the bimodal case. Likewise the previous subsection, in the unimodal cases the whole available data is considered, regardless whether the sea state belongs to a bimodal sea state or not, in order to provide enough data for the calculation.

Each set consists of 49 copulas, one per each weather type, and the parameters of the copulas (correlation coefficient ρ, skewness parameters δ_1 and δ_2 and degrees of freedom ν) are estimated using the procedure based on maximum likelihood proposed by Yoshiba (2015), who published the corresponding R code which was modified to be used in this study.

As an example, the two following figures show the set of AC skew-t copulas for the unimodal cases. In the figures, X_1 and X_2 represent the univariate margins of $H_{s_{sea}}$ and $T_{p_{sea}}$, and X_4 and X_5 do the same for $H_{s_{swell}}$ and $T_{p_{swell}}$, respectively. Data in colors (blue for sea and red for swell) represent the univariate margins computed from the empirical CDF of the variables associated to each WT, while the gray dots correspond to 1,000 simulated values using the fitted AC skew-t copula to each WT data.

The skewness of the joint distribution of H_s and T_p is more visible in the sea component, and the best fit is obtained for weather types with more data.
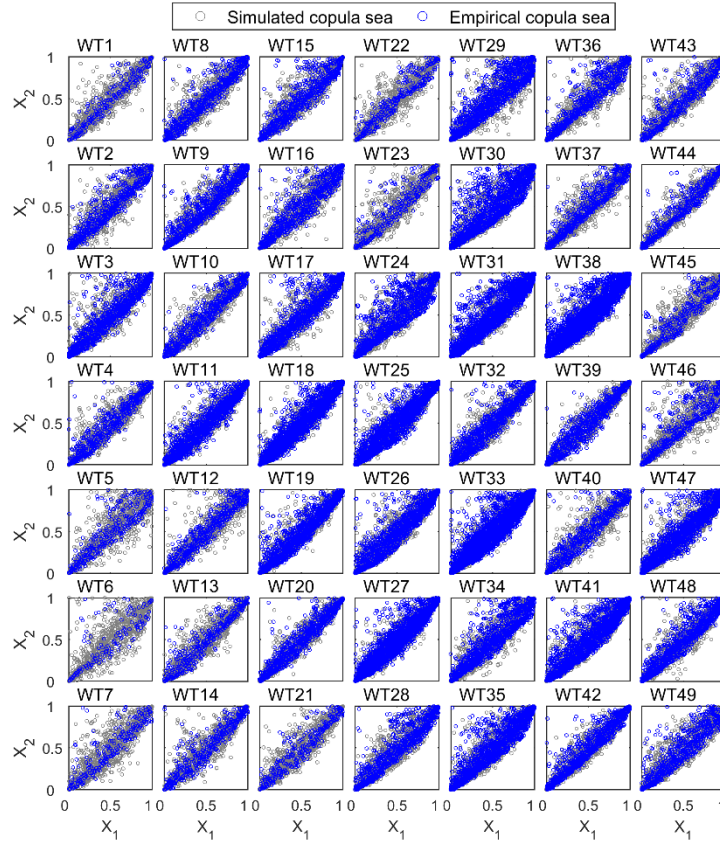
Figure 4-16: Set of skew-t copulas for the sea component. Observations are shown in blue and simulated values from the fitted copulas are shown in gray.
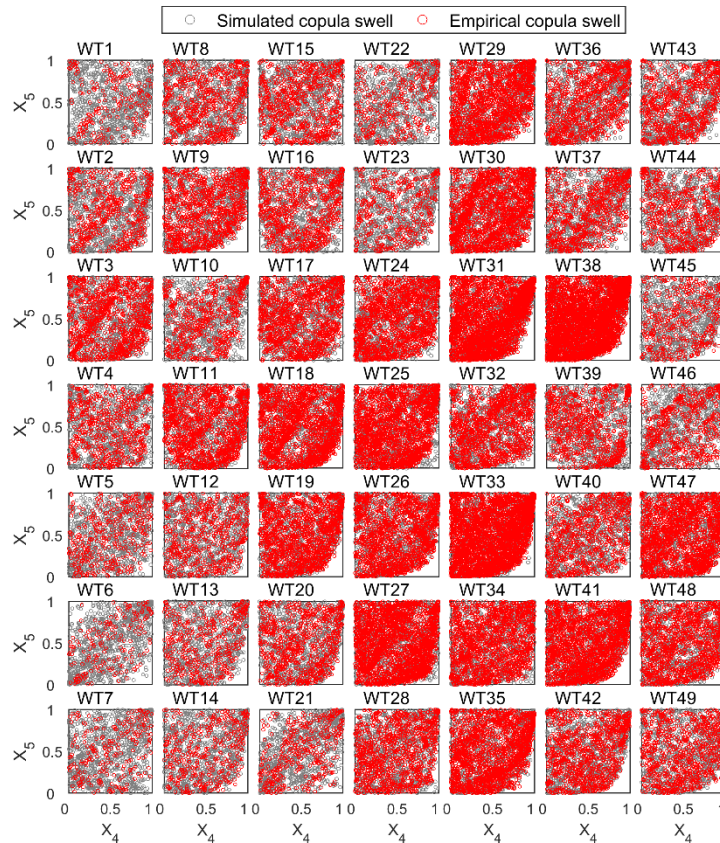

Figure 4-17: Set of skew-t copulas for the swell component. Observations are shown in red and simulated values from the fitted copulas are shown in gray.

4.7.3. Dependence structure

In the case of unimodal sea states, the dependence structure is defined by 3 variables: H_s, T_p and Dir, and the joint distribution between them can be modeled using the vine-copula approach, where bivariate distributions are considered at the first level and then conditional bivariate distributions are needed for the subsequent levels. This structure corresponds to a D-vine on 3 variables and Figure 4-18 shows an example, where the bivariate dependence between H_s and T_p is modeled using a AC skew-t copula (denoted in red) and a Gaussian copula is considered for the pair $T_p - Dir$ (denoted in blue). Afterwards, the relation between H_s and Dir is established by a conditional Gaussian copula (denoted in blue), i.e. the bivariate distribution of H_s and Dir given T_p.

In the figure, the edges indicate the rank correlation between the variables: r_{12} and r_{23} denote the Spearman´s rank correlation between the corresponding variables, and $r_{13|2}$ means the conditional rank correlation between 1 and 3 given 2.
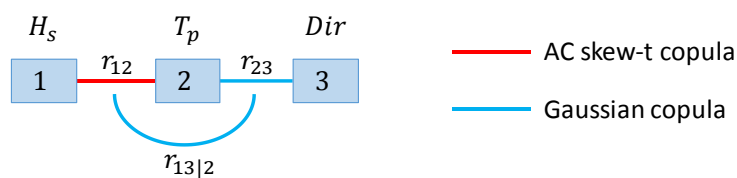

Figure 4-18: D-vine on 3 variables with (conditional) rank correlations.

In the bimodal case, the dependence structure is more complex but the concept is the same, where conditional pair-copulas are added as building blocks of the multivariate distribution, forming a D-vine on 6 variables. The bivariate distribution of H_s and T_p are modeled using the AC skew-t copulas previously described, and the relation between the remaining variables is considered to be Gaussian, as it is schematized in Figure 4-19. AC skew-t copulas are located at the outer positions of the first tree in order to optimize the sampling procedure, as it is explained later in §4.9.
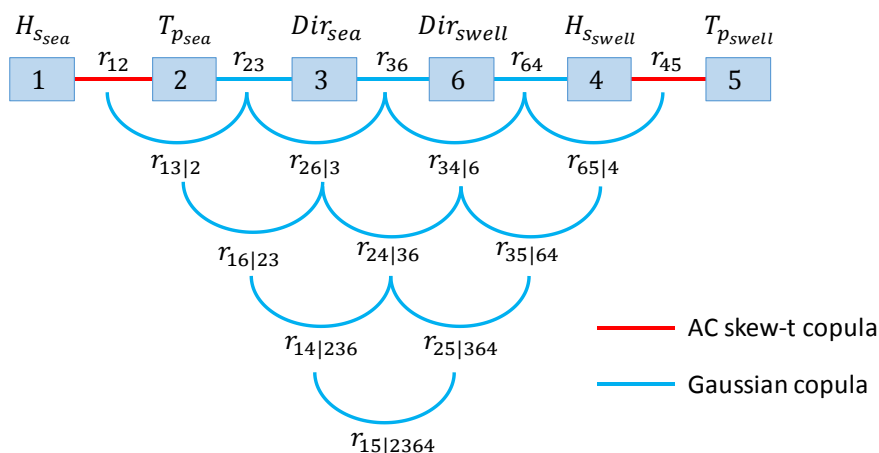

Figure 4-19: D-vine on 6 variables with (conditional) rank correlations.

In the D-vine from the figure, the conditional copulas depend on the partial correlations for each level. For instance, in the last level the partial correlation between 1 and 5 given 2,3,6,4 is needed to define the conditional copula between 14|236 and 25|364, which are conditional copulas depending on the previous level, and so on until the base level is reached. Therefore, all the copulas are defined from the rank correlations shown in §4.7.1.

It is important to recall that bivariate Gaussian copulas are defined by the linear correlation coefficient, thus the rank correlations must be transformed using the relation:

$$\rho = 2 \sin\left(\frac{\pi}{6} r\right) \tag{4-6}$$

Where ρ is the Pearson (linear) correlation coefficient and r is the Spearman's rank correlation coefficient.

4.8. Emulator of daily WTs

As it was mentioned in §2.1.4, the chronology model should be capable to reproduce the historical probability of occurrence of each WT, the transition probabilities between WTs, the persistence of each WT and the seasonal to interannual variability (Guanche et al., 2014). In order to assess these capabilities, synthetic sequences of weather types can be obtained through Monte Carlo simulation, where 100 samples are generated to explore the stochastic nature of the process. Each sample is 36 years long for a fair comparison to the observed data.

The validation of the chronology model is made by a fourfold comparison against the historical sequence of weather types:

1. Mean annual occurrence probabilities of WTs.
2. Mean annual duration of WTs.
3. Transition probability matrix between WTs.
4. Persistence analysis of WTs.

4.8.1. Mean annual occurrence probabilities of WTs

In order to explore the interannual variability of the weather types, the mean annual occurrence probability for each WT is computed over the available 36 years. Then, the mean annual probabilities of each WT are averaged over the whole period and the temporal standard deviations are estimated.

Figure 4-20 shows the comparison between observed and simulated averaged mean annual probabilities on the left panel and the temporal standard deviation of the values for each WT. Results are close to the diagonal in both cases, which demonstrate that the model simulations are capable of reproducing the probability of occurrence associated with each WT appropiately and furthermore preserving the interannual variability observed in the historical data.
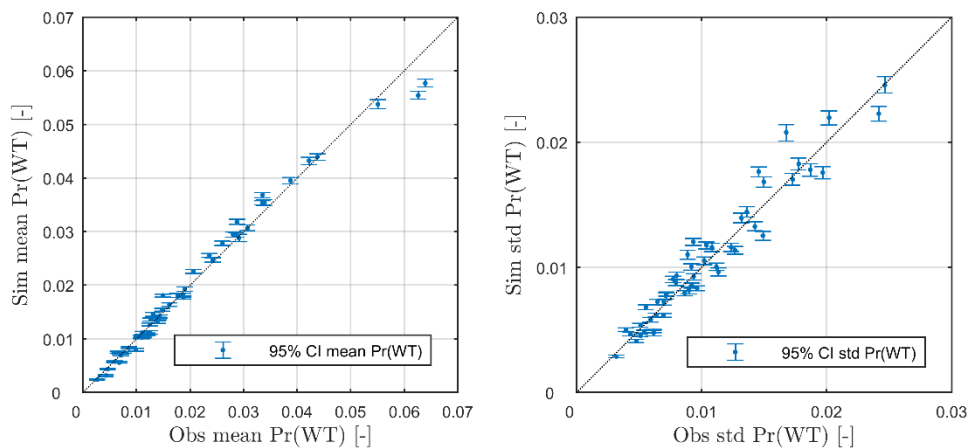

Figure 4-20: Scatter plot of observed and simulated mean annual occurrence probabilities of each WT.

4.8.2. Mean annual duration of WTs

A second way to assess whether the interannual variability is adequately represented in the chronology model is computing the mean annual duration of each weather type. This is also an indicator of the persistence of each WT. Likewise the annual probabilities, the mean annual durations are averaged over the whole period and the temporal standard deviations are estimated.

The comparison between observed and simulated averaged mean annual durations is depicted on the left panel of Figure 4-21, and the corresponding temporal standard deviation for each WT is shown in the right panel. Again, results are close to the diagonal, proving that the simulations reproduce the weather dynamics in terms of the duration of each WT and furthermore the interannual variability observed in the historical data is retained.
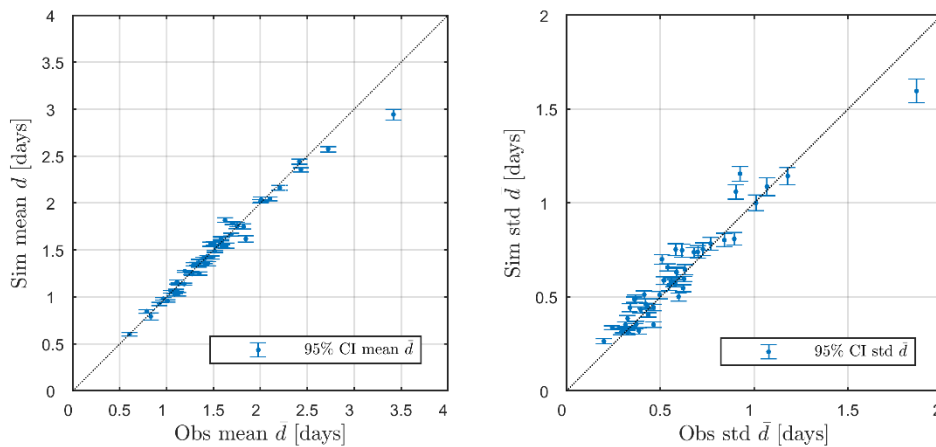

Figure 4-21: Scatter plot of observed and simulated mean annual duration of each WT.

4.8.3. Transition probability matrix between WTs

Figure 4-22 presents the observed and mean simulated transition probability matrices, which show the probability of changing from WT i to WT j between consecutive days. Thus, the diagonal of the transition matrix corresponds to the probability of staying in the same weather type. From panels a) and b), it can be concluded that staying in the same weather type is more likely to occur, because a darker color indicates a higher probability.

Both matrices look very similar, thus the model is effectively reproducing the transition probabilities between weather types, observed in the historical data. This is confirmed in the plot from panel c), where the same matrices are presented as a scatter plot between observed and simulated probabilities. Results are very close to the diagonal and the confidence intervals, estimated over the 100 samples, show little variability among the simulations.
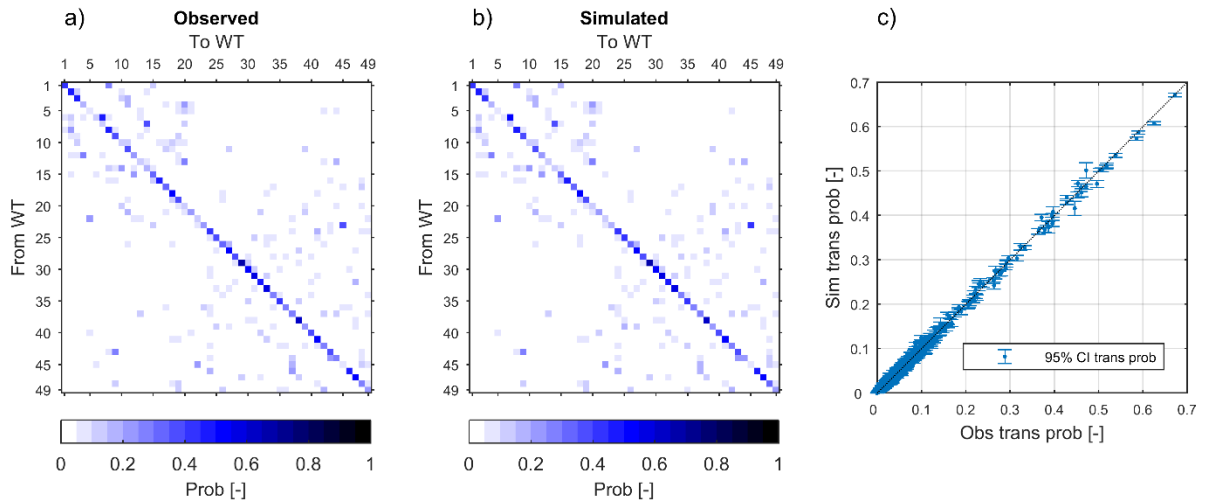
Figure 4-22: a) Observed and b) simulated transition probability matrices. c) Comparison between observed and simulated transition probabilities.

4.8.4. Persistence analysis of WTs

Finally, a persistence analysis of the weather types is performed in order to check the capability of the model to reproduce the weather dynamics. Figure 4-23 shows the cumulative distribution of the persistence associated with each WT. The red line represents the mean simulated distributions over the 100 samples, showing a good matching with the empirical distribution (black line) in all the cases.

In general terms, it can be seen that weather types at the right in the lattice are more persistent than the ones associated to low-pressure systems (left side of the lattice), where the probability of staying just 1 day in the WT is closer to the unity.
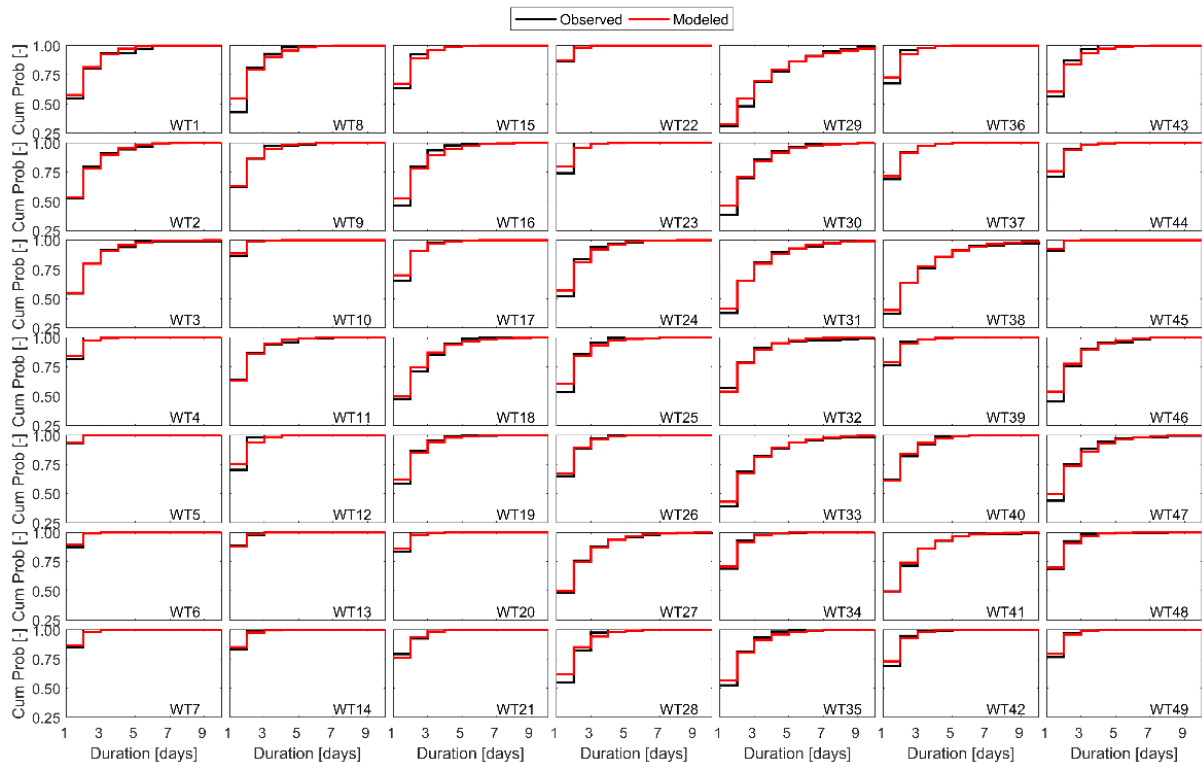

Figure 4-23: Observed and simulated cumulative distribution of the persistence for each WT.

Based on the results from these comparisons, the chronology model is validated and therefore can be used to generate synthetic sequences of weather types.

4.9. Emulator of sea state parameters

Once the synthetic time series of weather types have been constructed, a MonteCarlo simulation can be undertaken in order to generate synthetic time series of multi-modal wave parameters. For each time step, the simulation method is divided in two steps (Rueda et al., 2017):

1. Generation of a sea state type I_i using the empirical probabilities obtained in §4.5.
2. Simulation of the corresponding wave parameters considering the marginal distributions fitted in §4.6 and the multivariate copula associated to each WT described in §4.7.

During the MC simulation, 100 samples are generated to explore the stochastic nature of the process. Each sample is 20 years long (1993 to 2012) with 3-hourly sea states, to ease the comparison to the observed data.

4.9.1. Sampling procedure

The first step of the MC simulation is generating the sea state types. For each weather type, a vector containing values 1, 2 and 3, where each value is related to sea, swell and combined respectively, is randomly generated using the empirical probabilities obtained in §4.5. Then, the second step proceeds, where the length of the samples for each WT depends on the number of sea states generated.

In the case of unimodal sea states, the cumulative sampling procedure for a D-vine on 3 variables is applied, following Kurowicka and Cooke (2006). Let X_1, X_2 and X_3 be the margins of the variables H_s, T_p and Dir, and let U_1, U_2 and U_3 be independent uniform [0,1] variables. Then, the sampling procedure proceeds as follows:

1. Random sampling from U_1, U_2 and U_3, where realizations are denoted u_1, u_2 and u_3.
2. $x_1 = u_1$
3. Calculate x_2 from the inverse conditional AC skew-t copula (conditional on x_1):

$$x_2 = F_{r_{12};x_1}^{-1}(u_2) \tag{4-7}$$

   In this notation, $F_{r_{12};x_1}$ denotes the conditional copula between 1 and 2 given the sample x_1 with rank correlation r_{12}.

4. Calculate x_3 using the conditional Gaussian copula between 1 and 3 given 2, according to the D-vine schematization shown in Figure 4-18:

$$x_3 = F_{r_{23};x_2}^{-1}\left(F_{r_{13|2};F_{r_{12};x_2}(x_1)}^{-1}(u_3) \right) \tag{4-8}$$

As it was explained in §2.1.8, the conditional Gaussian copulas are given by eqs. (2-13) and (2-14). In the case of the AC skew-t copulas, the calculation of the conditional distribution functions must be done numerically, because there is no closed form available. For the sampling procedure, 500,000 values were randomly generated for each fitted AC skew-t copulas associated to each sea state and each weather type, and then the cumulative distributions F and F^{-1} are computed using the corresponding conditional sample.

Once x_1, x_2 and x_3 have been generated, the values for H_s, T_p and Dir can be directly obtained using the inverse cumulative distribution functions fitted for each weather type, as shown in §4.6.

For the bimodal case, the sampling procedure is more complicated because now a D-vine on 6 variables is involved. Extending the preceding approach, the sampling procedure requires the generation of 6 independent uniform [0,1] variables. Keeping the same subindices for the wave parameters shown in Figure 4-19, the sampling procedure can be summarize using a short notation (Kurowicka & Cooke, 2006):

$$x_1 = u_1 \tag{4-9}$$

$$x_2 = F_{2|1:x_1}^{-1}(u_2) \tag{4-10}$$

$$x_3 = F_{3|2:x_2}^{-1}\left(F_{3|12:F_{1|2}(x_1)}^{-1}(u_3)\right) \tag{4-11}$$

$$x_6 = F_{6|3:x_3}^{-1}\left(F_{6|23:F_{2|3}(x_2)}^{-1}\left(F_{6|123:F_{1|23}(x_1)}^{-1}(u_6)\right)\right) \tag{4-12}$$

$$x_4 = F_{4|6:x_6}^{-1}\left(F_{4|36:F_{3|6}(x_3)}^{-1}\left(F_{4|236:F_{2|36}(x_2)}^{-1}\left(F_{4|1236:F_{1|236}(x_1)}^{-1}(u_4)\right)\right)\right) \tag{4-13}$$

$$x_5 = F_{5|4:x_4}^{-1}\left(F_{5|64:F_{6|4}(x_6)}^{-1}\left(F_{5|364:F_{3|64}(x_3)}^{-1}\left(F_{5|2364:F_{2|364}(x_2)}^{-1}\left(F_{5|12364:F_{1|2364}(x_1)}^{-1}(u_5)\right)\right)\right)\right) \tag{4-14}$$

The full terms of the sampling procedure are available to the reader in the Appendix E.

Once again, after $x_1, x_2, x_3, x_4, x_5, x_6$ have been generated, the values for $H_{s_{sea}}, T_{p_{sea}}, Dir_{sea}, H_{s_{swell}}, T_{p_{swell}}, Dir_{swell}$ can be directly obtained using the inverse cumulative distribution functions fitted for each weather type, as shown in §4.6.

4.9.2. Correlation between simulated variables

Validation of the simulated wave climate can be addressed comparing the rank correlations between simulated wave parameters and the rank correlation between the observed variables. Figure 4-24 shows the mean rank correlations, averaged over the 100 samples, related to the bimodal sea state, associated with each weather type. Comparing to the observed values shown in Figure 4-15, it can be seen that the rank correlation between variables is succesfully reproduced by the dependence structure, preserving the statistical relations between the wave parameters. In the unimodal cases, the match is as good as the one presented in Figure 4-24 (not shown).

4.9.3. Joint distributions of simulated variables

Finally, a second validation of the simulated wave climate is carried out in terms of the bivariate distributions between wave parameters. The following set of figures show the joint distribution of the pairs $H_s - T_p$, $Dir - H_s$ and $Dir - T_p$ for the sea component, regardless if the data belong to an unimodal or bimodal sea state. The set of figures for swell is included in Appendix F. In the figures, the observed and simulated wave data is sorted by months, and the wave climate from the 100 samples is plotted at the same time. The colored contours show the joint probability density of each pair of variables.

In general terms, the statistical model for the predictand gives a sound representation of the present wave climate. Joint probability density of simulated values appears much wider and denser than the observed densities because 1 realization of present wave climate is being compared against 100 samples. Nevertheless, the simulated joint densities follow the observed distributions as it can be concluded comparing the contours.
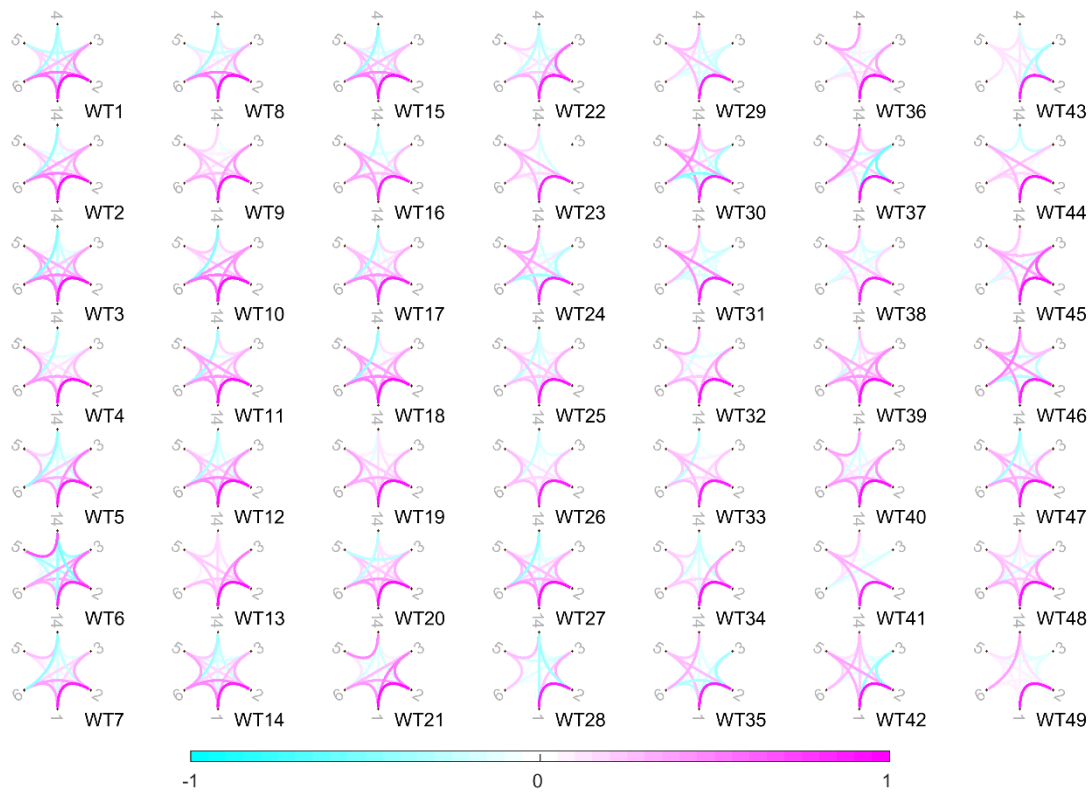
Figure 4-24: Graphical representation of correlation coefficients for the simulated bimodal sea state associated to each WT. Numbers from 1 to 6 stand for $H_{s_{sea}}, T_{p_{sea}}, Dir_{sea}, H_{s_{swell}}, T_{p_{swell}}, Dir_{swell}$ respectively. Color scale is defined between -1 (cyan) for negative correlation, 0 (white) for no correlation and 1 (magenta) for positive correlation.

Looking more in detail, the bivariate distribution of $H_{s_{sea}} - T_{p_{sea}}$ depicts the capability of the AC skew-t copula of representing the skewness observed in the empirical joint distribution. However, this is not that clear when analyzing the swell component, but this can be explained looking at Figure 4-17, where the skewness of the swell copulas is not as notorious as the one of the sea.

Regarding the wave mean direction, the behavior is as expected: sea component is coming mainly from SW and the swell is arriving predominantly from N. Fractions of swell coming from SW are also well represented in the simulated data. Swell coming from E must be treated carefully, as these appear to be spurious, due to issues in the post-processing of the IFREMER data.
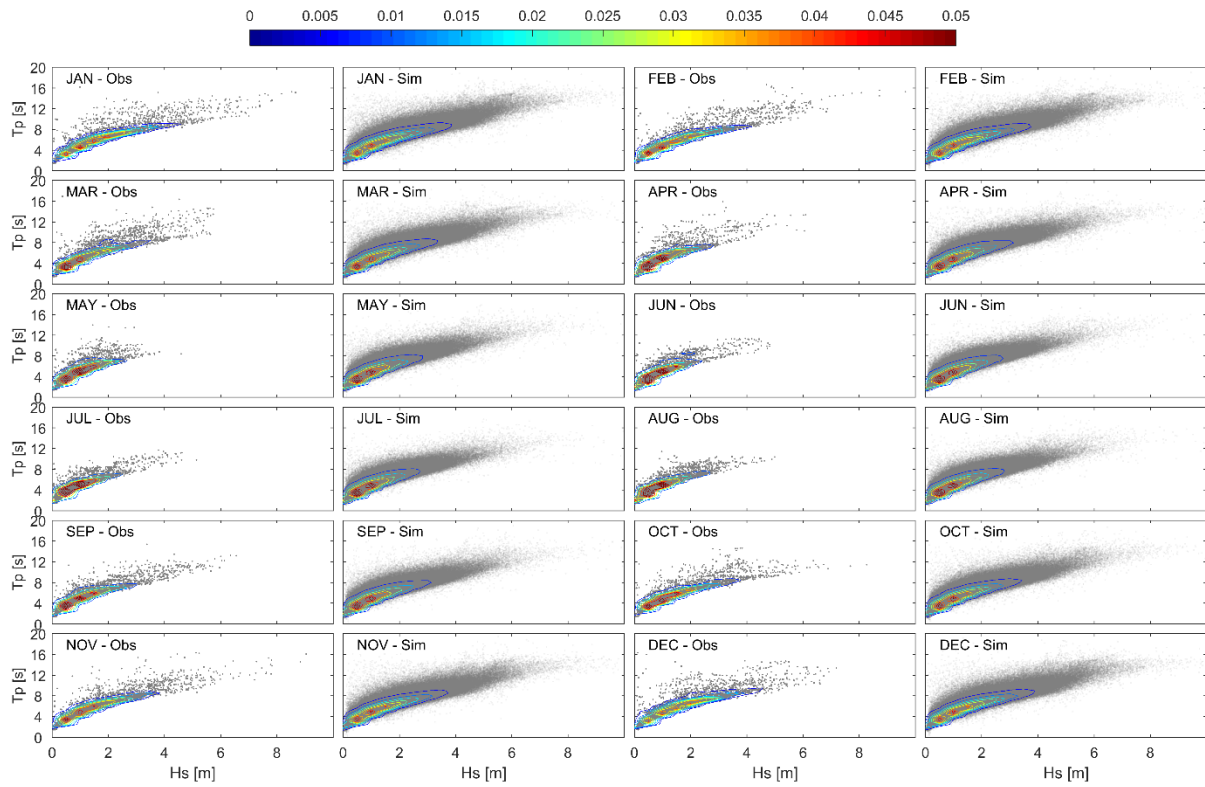
Figure 4-25: Joint probability density of the pair $H_s - T_p$ for the sea component, sorted by months. Simulated values correspond to 100 samples. Joint probability density is shown by colored contours.
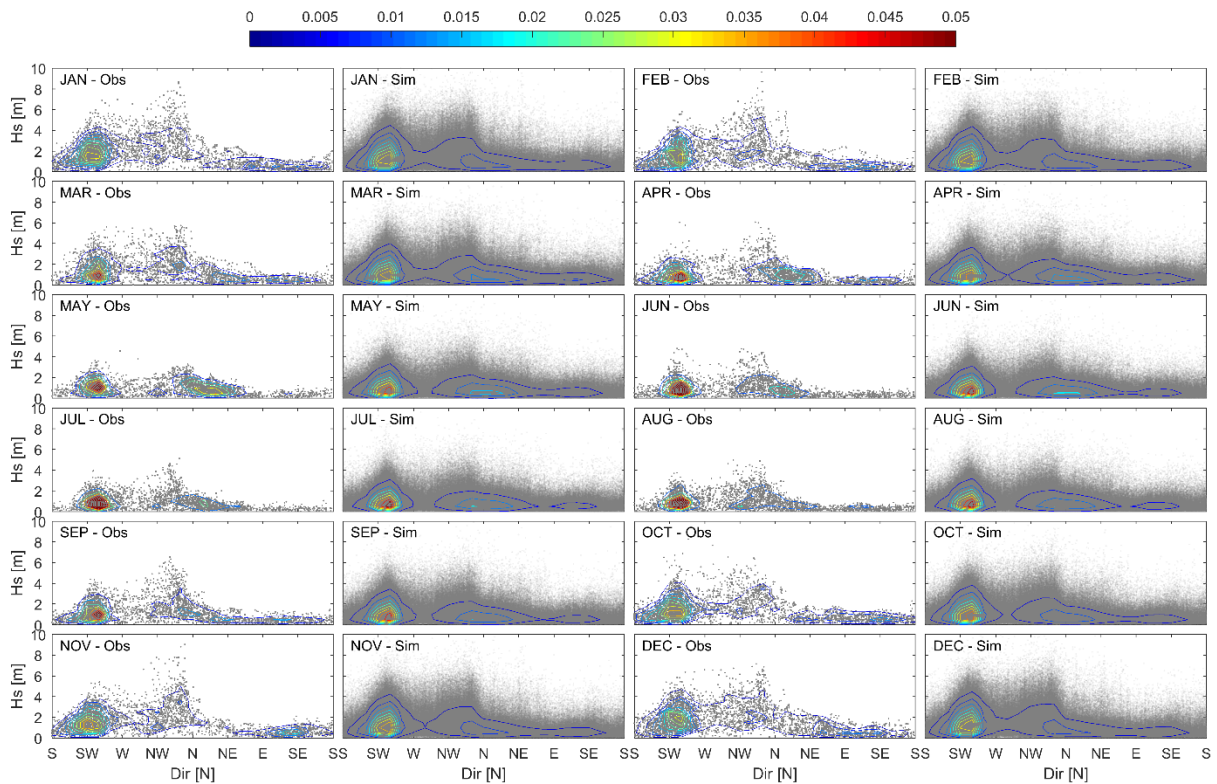

Figure 4-26: Joint probability density of the pair $Dir - H_s$ for the sea component, sorted by months. Simulated values correspond to 100 samples. Joint probability density is shown by colored contours.
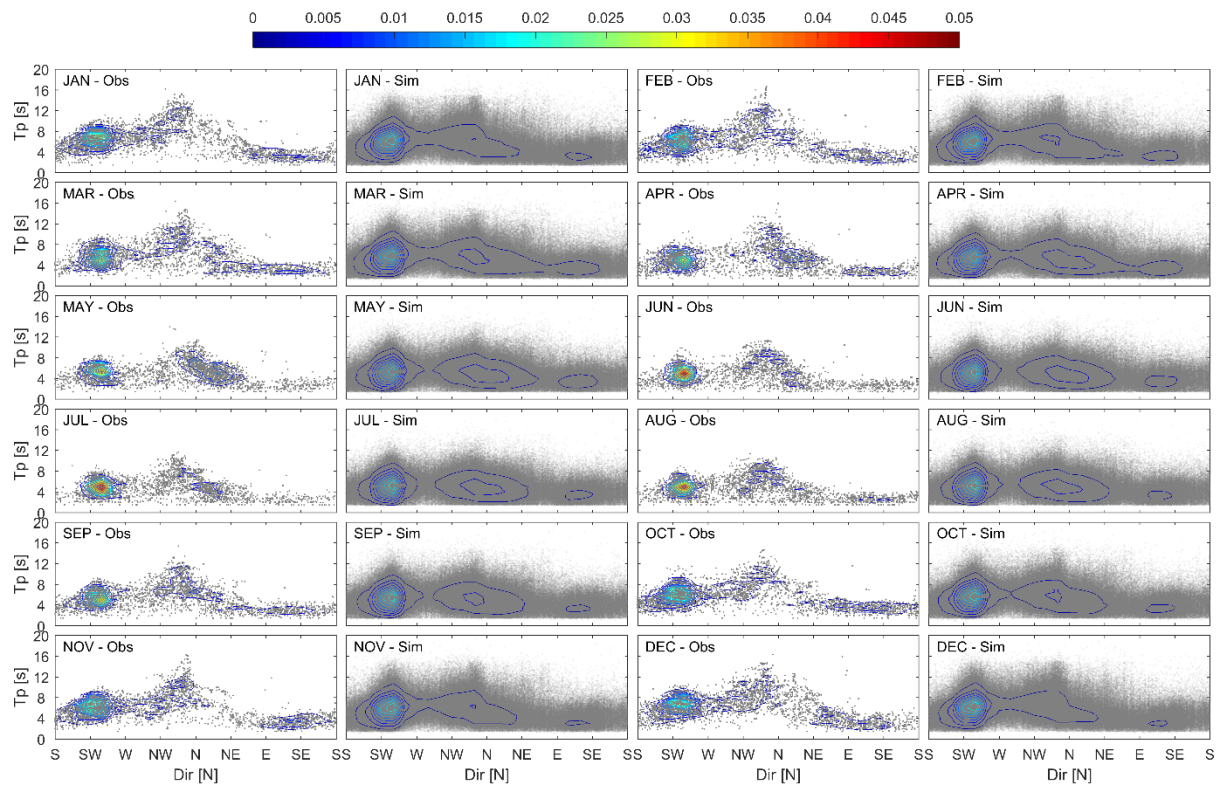
Figure 4-27: Joint probability density of the pair $Dir - T_p$ for the sea component, sorted by months. Simulated values correspond to 100 samples. Joint probability density is shown by colored contours.

5. Future wave climate

This chapter presents the results obtained following the methodology described in §3.3.

5.1. Validation of GCM ACCESS1.0

5.1.1. Weather types

Firstly, the SLP fields and the SSLPGs are considered to build the predictor at daily scale. The SLP fields are extracted from the outcomes of the GCM ACCESS1.0 for the historical scenario, spanning from 1979 to 2005 (27 years) with daily resolution.

The predictor is assembled as explained in §4.1.2 over the area determined using the ESTELA model. Then, the time series of the daily predictor is projected over the 52 EOFs obtained from CFSR reanalysis. Afterwards, KMA is applied to the PCs considering 49 clusters being represented initially by the centroids from CFSR reanalysis. Finally, new centroids are estimated as the closest data value in ACCESS1.0 to the average over the whole data in each cluster, leading to a new set of weather types, which is shown in Figure 5-1.

The set of WTs is similar to the one obtained for the CFSR reanalysis data, shown in Figure 4-7, and the differences may be explained by the spatial and temporal resolution in ACCESS1.0 being different than the reanalysis.
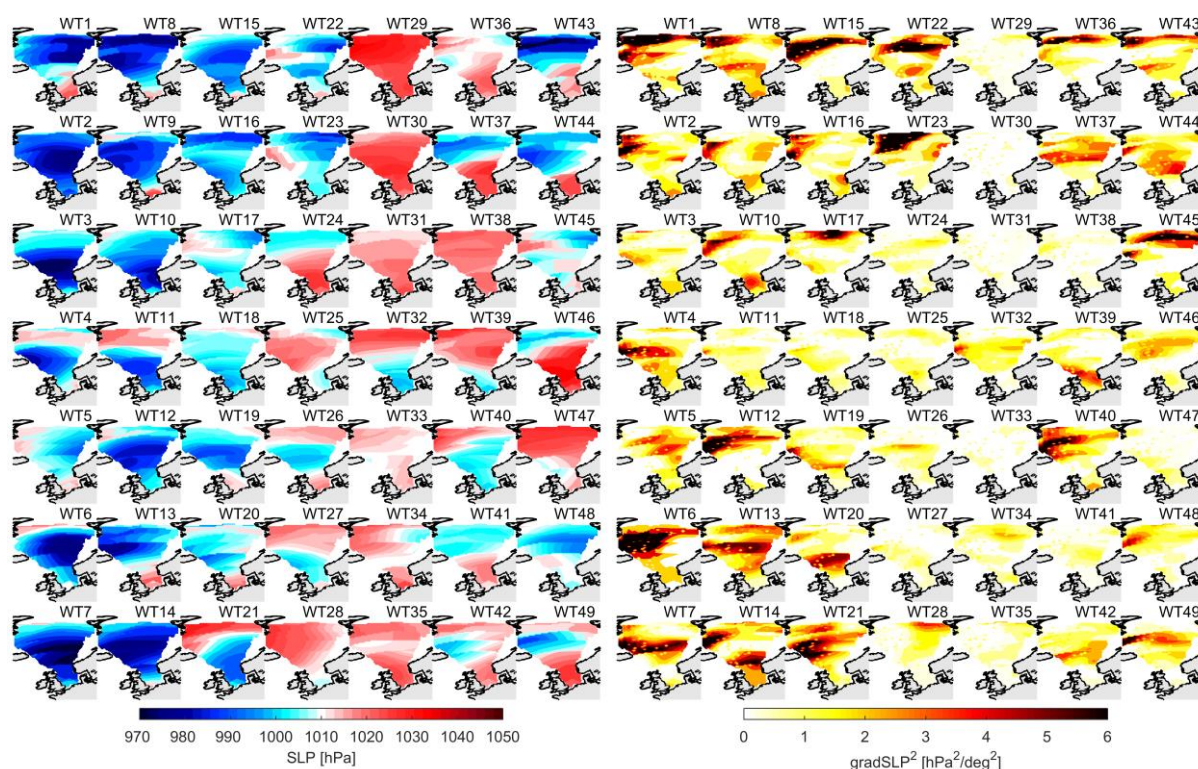

Figure 5-1: 49 Weather Types represented as SLP fields (left panel) and as the square of the SLP gradients (right panel), obtained for Noordwijk using KMA and the predictor from ACCESS1.0 model for the historical period.

50

After the set of weather types have been validated, the analysis of the statistical model for the daily predictor from ACCESS1.0 must be carried out involving 4 tests:

1. Occurrence probability over the whole period, at seasonal and monthly scale.
2. Chronology model of the WTs.
3. Transition probability matrices
4. Persistance associated to each WT.

For a fair comparison, the common period of 27 years (1979 – 2005) are selected from both the CFSR reanalysis and ACCESS1.0 model.

5.1.2. Occurrence probability of weather types

Figure 5-2 shows the probability of occurrence of each weather type, according to the predictor from CFSR data and from the GCM ACCESS1.0. Both lattices look similar, but differences are evidenced in Figure 5-3, where the absolute differences for each WT are shown on the left panel. Differences relative to the CFSR data are shown in the right panel of the latter figure. Although differences in probabilities are small in absolute terms, some of these differences can reach up to 50% in relative terms.
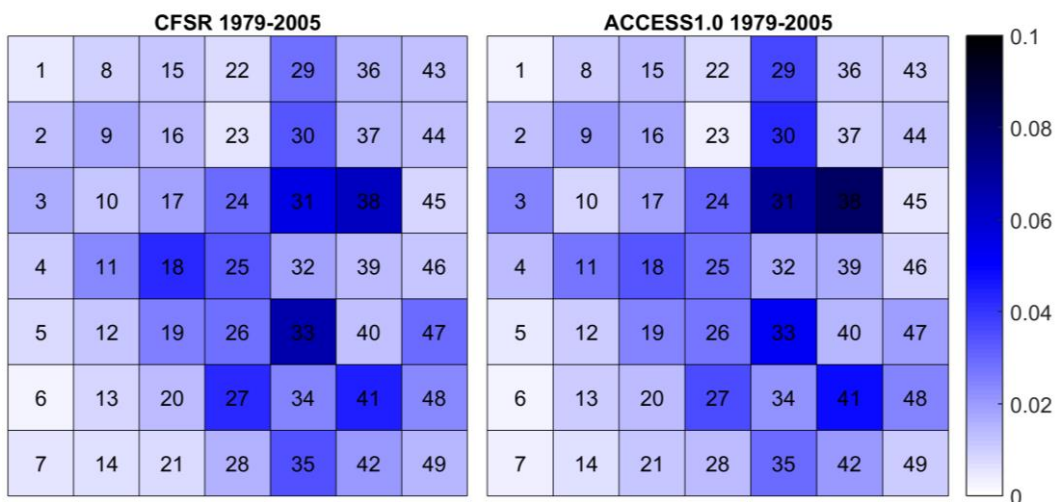

Figure 5-2: Occurrence probability associated to each WT for daily predictor from CFSR (left panel) and ACCESS1.0 (right panel).
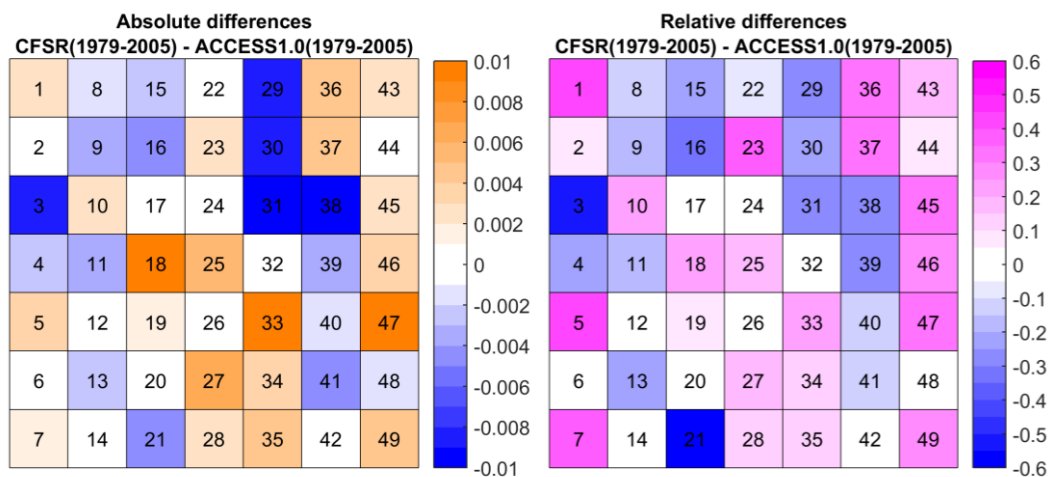

Figure 5-3: Comparison of occurrence probability associated to each WT in terms of absolute differences (left panel) and differences relative to CFSR (right panel).

In order to compare objectively the differences between both occurrence probability lattices from Figure 5-2, the same two metrics considered by Pérez et al. (2014b) to assess the performance of the CMIP5 models are introduced, namely the scatter index and the relative entropy.

The scatter index SI corresponds to the root mean square error normalized by the mean frequency:

$$SI = \frac{\sqrt{\frac{\sum_{i=1}^{N}(p_i - p_i')^2}{N}}}{\frac{\sum_{i=1}^{N} p_i}{N}} \tag{5-1}$$

Where p_i denotes the probability of the weather type i estimated from the CFSR reanalysis, p_i' is the relative frequency for the same weather type from ACCESS1.0 and N is the number of weather types.

The relative entropy is defined using the same variables as:

$$RE = \sum_{i=1}^{N} p_i \left| \log\left(\frac{p_i}{p_i'}\right) \right| \tag{5-2}$$

The scatter index gives more importance to commonly occurring situations, whereas the relative entropy is more suitable to analyze weather types with low occurrence probability, which might be related to extreme events (Pérez et al., 2014b).

Lower values of SI and RE indicate a high degree of similarity between both predictors. In this case, for the historical period values of $SI = 0.27$ and $RE = 0.19$ are obtained, therefore it can be concluded that the relative frequencies of the weather types are well represented by the GCM ACCESS1.0 model.

The same analysis at seasonal and monthly scale is presented in Appendix G, where it can be seen that both the seasonal and monthly structures are well represented in both datasets.

5.1.3. Chronology model of weather types

The empirical cumulative probabilities of each WT within a year are shown in Figure 5-4 for CFSR data (top panel) and ACCESS1.0 data (bottom panel). Both the seasonality and the autorregresive term are well represented, even though some differences are observed especially during the summer, where the probability of the last WTs increases (purple area in the figure).
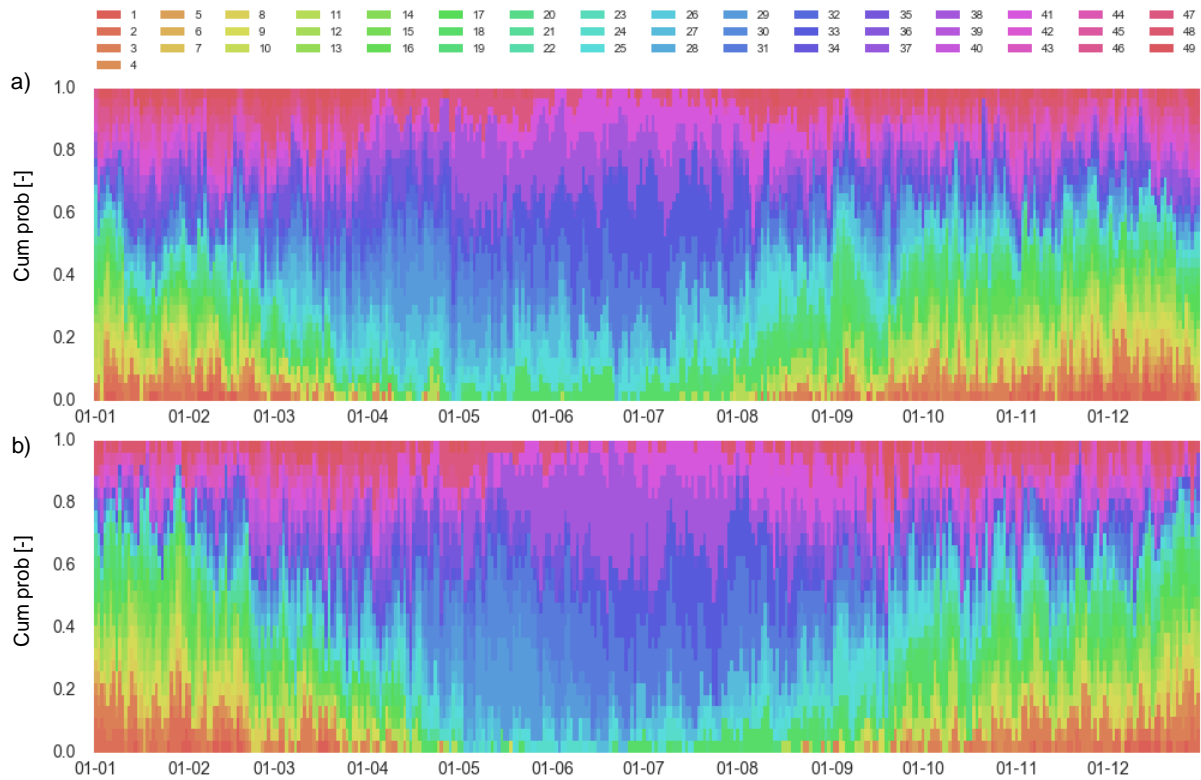
Figure 5-4: Empirical cumulative probabilities of each WT within a year from a) CFSR and b) ACCESS1.0.

5.1.4. Transition probability matrices

Transition probability matrices for both predictors are presented in Figure 5-5. The diagonal predominates in both cases, and differences between the matrices are located mostly outside the diagonal, as it is depicted in panel d) of the figure. Panel c) evidences some differences in the transition probabilities between both predictors, but they do not appear to be significant.
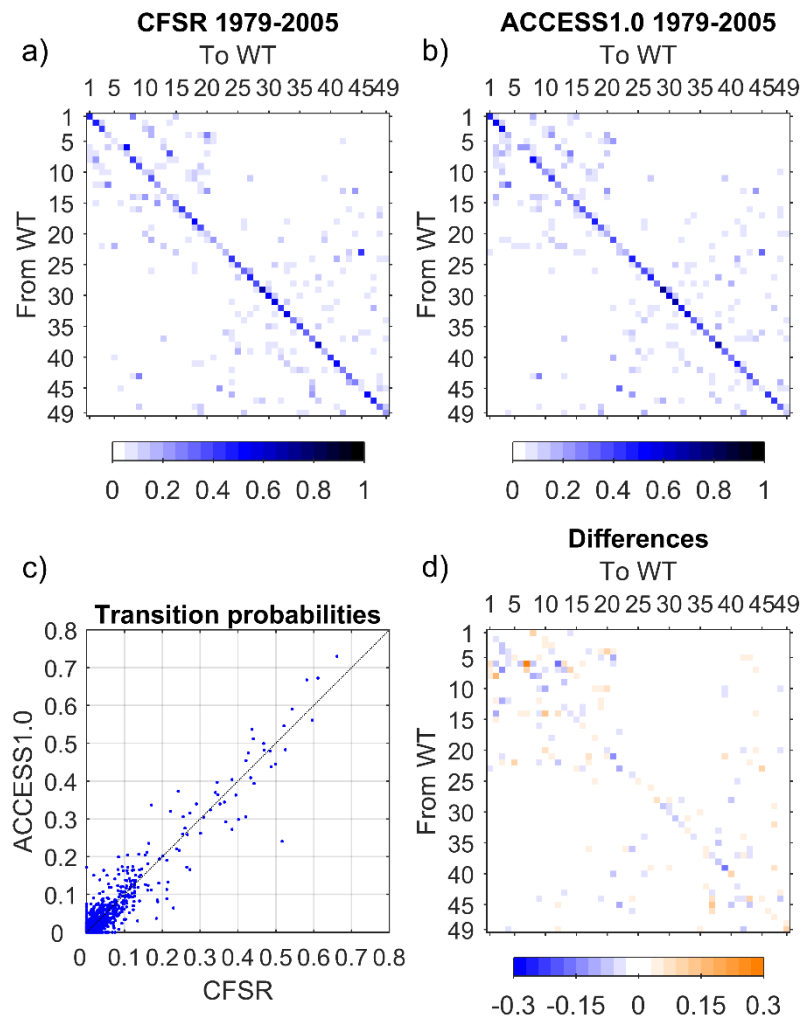
Figure 5-5: a) Transition probability matrix for CFSR, b) transition probability matrix for ACCESS1.0, c) comparison of transition probabilities between both predictors and d) absolute differences between transition probability matrices.

5.1.5. Persistence of each weather type

Finally, a persistence analysis of the WTs using both predictors is performed in order to check how the weather dynamics are reproduced by each predictor. Figure 5-6 shows the cumulative distribution of the persistence associated with each WT. The black line represents the distribution obtained from CFSR reanalysis, showing a good matching with the red line, associated to the ACCESS1.0 model for the same period, in all the cases.
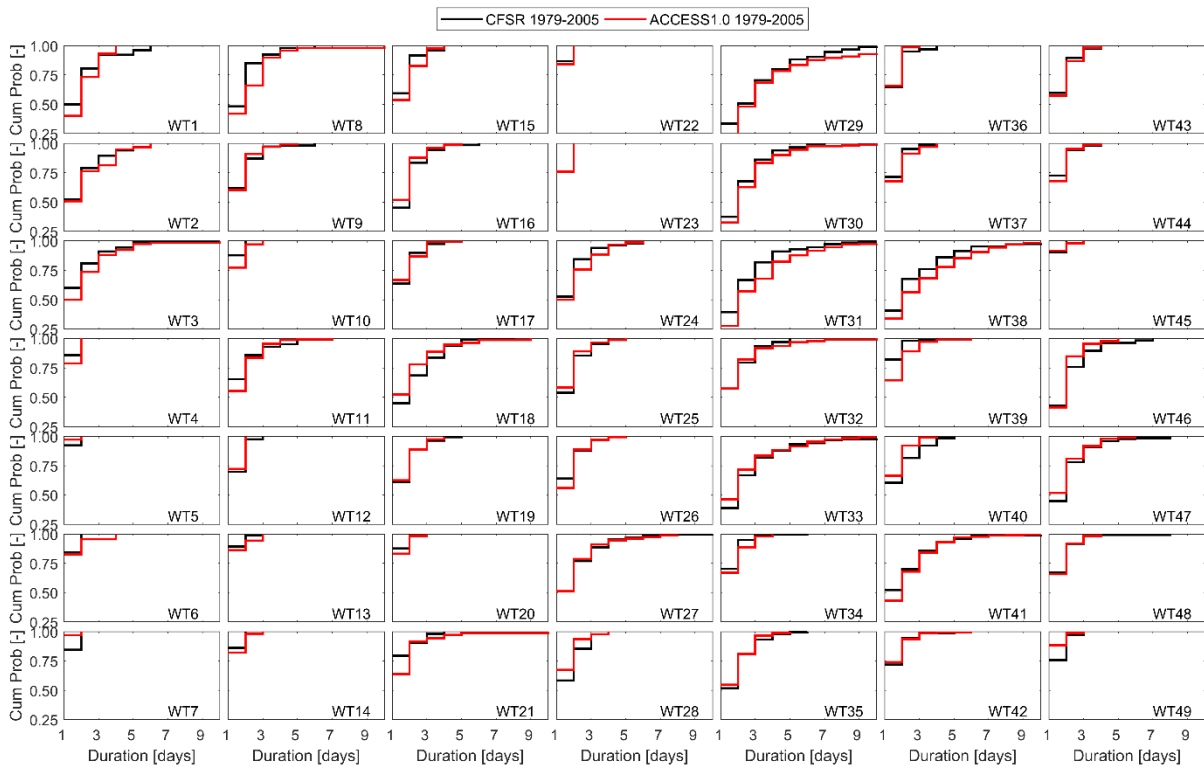
Figure 5-6: Comparison of persistence distribution related to each WT for both predictors.

Although some differences in the statistical model for the predictor between the CFSR and ACCESS1.0 datasets are observed, the agreement between both predictors is considered acceptable and the comparison with climate change projections proceeds.

5.2. Changes in future scenario

Once the GCM ACCESS1.0 has been validated for the historical scenario, the next step corresponds to apply the statistical model of the predictor to the SLPs and SSLPGs from the chosen scenario, being the most severe one (RCP8.5) during the last time slice of the century (2070-2099). This scenario is referred to as "future scenario" hereafter.

In this case, the procedure to obtain the future weather types is as follows:

1. Assemble the daily predictor using future scenario data.
2. Project the predictor data over the EOFs from the CFSR reanalysis.
3. Cluster the PCs using the centroids from the CFSR reanalysis.
4. Estimate new centroids as the closest data value in the future dataset to the average over the whole data in each cluster. This new set of centroids correspond to the future weather types.

The time sequence of WTs in the future scenario can be analyzed using the 4 tests from the previous subsection in order to determine the occurrence of changes in the predictor for the selected scenario.

5.2.1. Occurrence probability of weather types

Figure 5-7 shows the probability of occurrence of the weather types estimated over the whole period, for the historical period (1979-2005) and the future scenario (2070-2099). Changes are

highlighted in Figure 5-8, where small absolute changes in probabilities can be important when compared to the historical values. Changes in some weather types probabilities can reach up to 60% of increase or decrease.
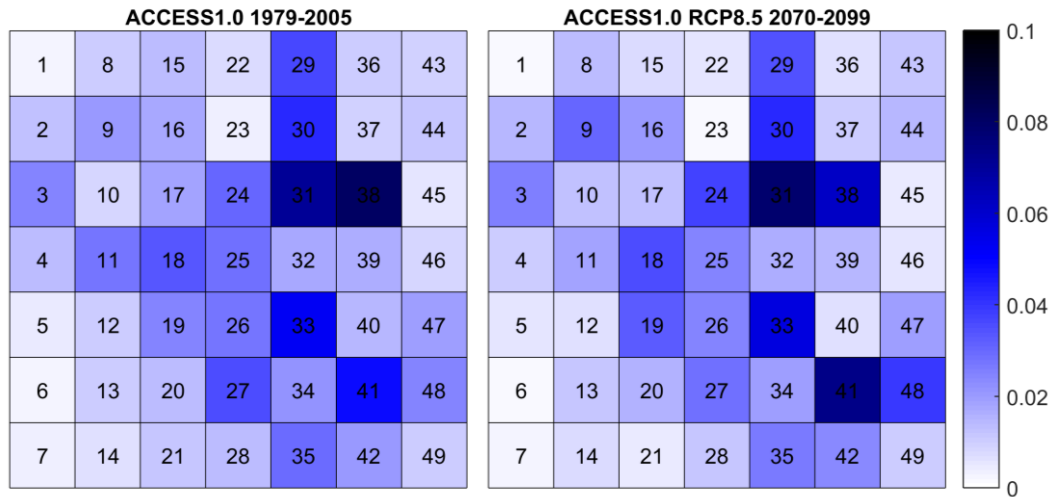

Figure 5-7: Occurrence probability associated to each WT for historical period (left panel) and future scenario (right panel).
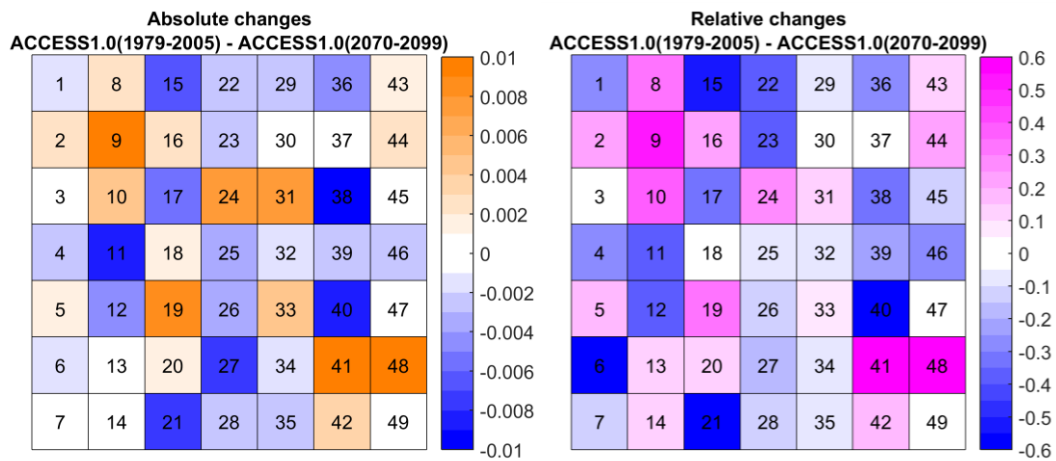

Figure 5-8: Changes in occurrence probability associated to each WT in terms of absolute differences (left panel) and differences relative to historical period (right panel).

The metrics introduced in §5.1.2 may be used to measure the degree of similarity between the present and future probabilities. In this case, the scatter index and the relative entropy are $SI = 0.31$ and $RE = 0.22$ respectively, being slightly higher than the values obtained for the comparison of ACCESS1.0 and the CFSR reanalysis in the historical period ($SI = 0.27$ and $RE = 0.19$) and therefore suggesting the occurrence of changes in the future period.

The same analysis at seasonal and monthly scale is presented in Appendix G, where minor changes in seasonal and monthly probabilities for the WTs are observed.

5.2.2. Chronology model of weather types

The empirical cumulative probabilities of each WT within a year are shown in Figure 5-9 for the historical period (top panel) and the future scenario (bottom panel). The most notorious changes are

identified during the summer, where the increase of WT41 at expenses of the decrease of WT38 is observed in the future projection.
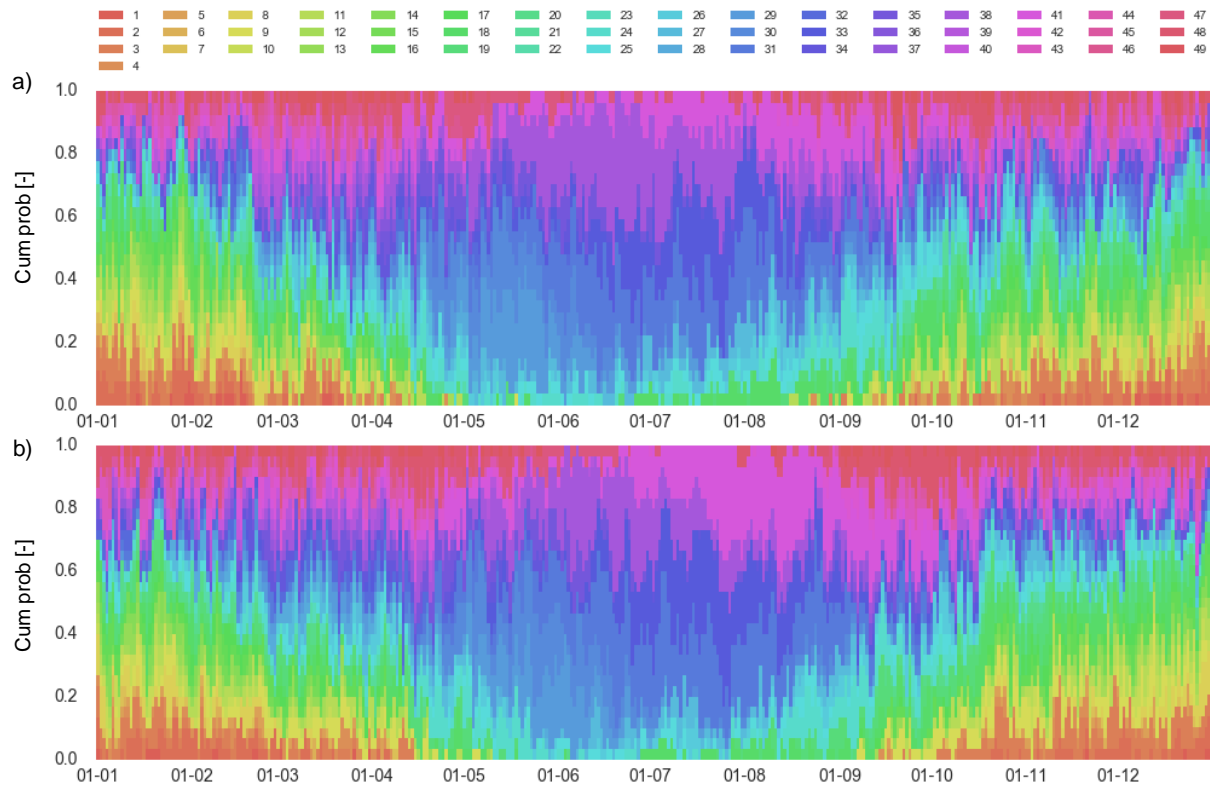
Figure 5-9: Empirical cumulative probabilities of each WT within a year from a) historical period and b) future scenario.

5.2.3. Transition probability matrices

Transition probability matrices for the historical period and the future scenario are presented in Figure 5-10. No significant changes are identified in this part of the projection, as the diagonal predominates in both cases, and differences between the matrices are located mostly outside the diagonal. Panel c) shows that transition probabilities of the same weather type lay near the diagonal of the plot, evidencing small changes between the historical period and the future scenario.
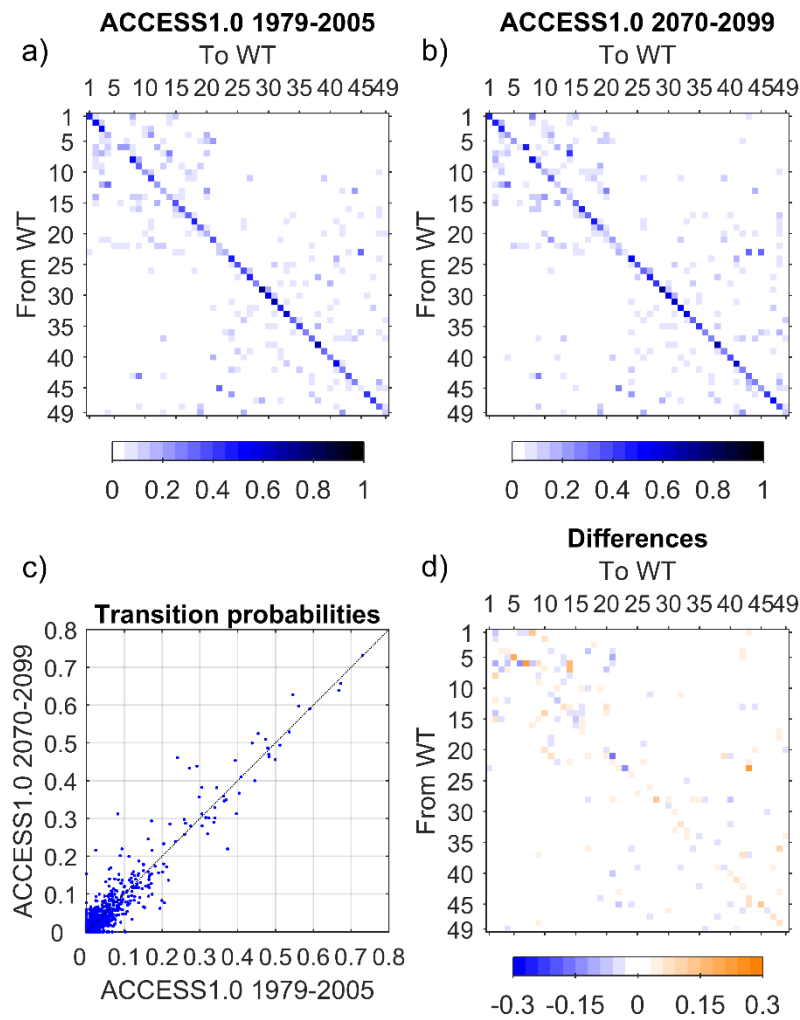
Figure 5-10: a) Transition probability matrix for historical period, b) transition probability matrix for future scenario, c) comparison of transition probabilities between both periods and d) absolute differences between transition probability matrices.

5.2.4. Persistence of each weather type

The last test corresponds to the persistence analysis of the weather types. Figure 5-11 shows the cumulative distribution of the persistence associated with each WT in red for the historical period, and in blue for the future scenario. In general terms, the observed changes do not appear to be significant, however WT21 shows an important reduction in the persistence.

Figure 5-11: Comparison of persistence distribution associated to each WT for both predictors.

6. Morphological simulation

This chapter presents the results obtained following the methodology described in §3.4.
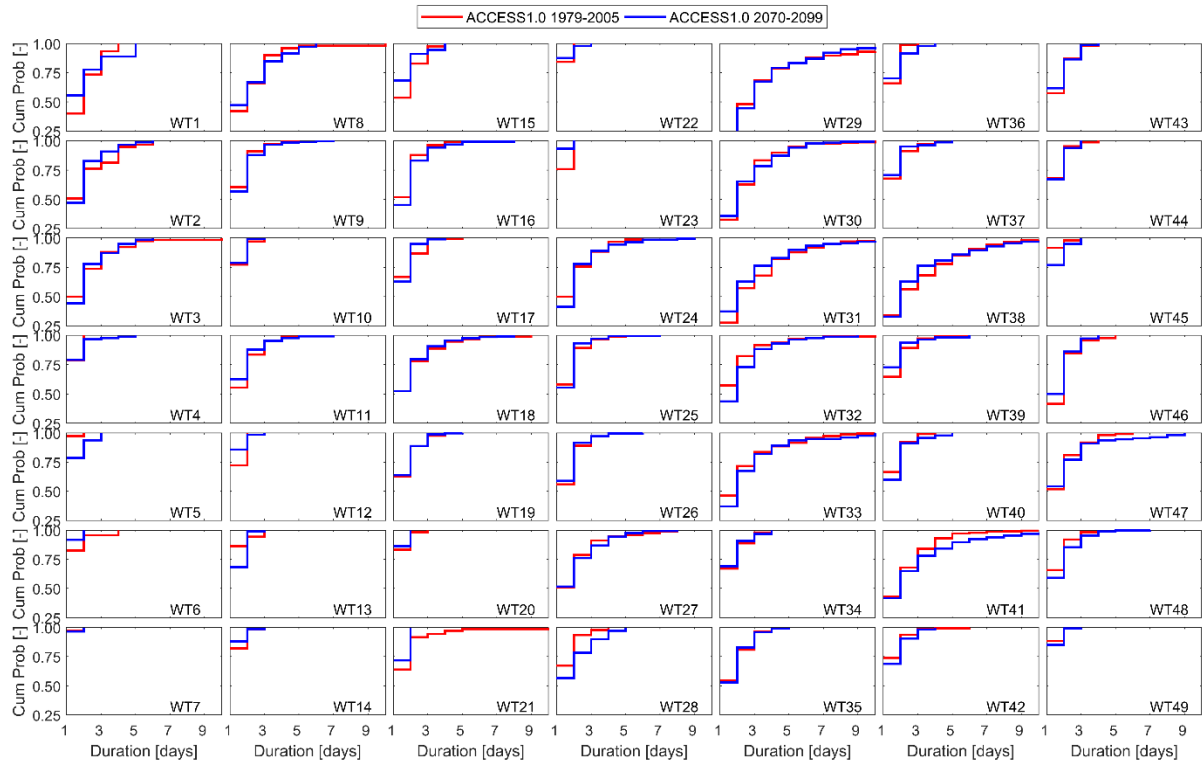
6.1. Model set-up

The same model calibrated and validated by Walstra et al. (2012) is considered to compute the total longshore sediment transport (LST) at Noordwijk, including bed load and suspended load transport. The initial profile is based on a single transect which was measured in 1984 and is interpolated onto a computational grid with a resolution of 200m offshore, gradually decreasing to 2m across the active part of the profile (above −10m water depth). The transect is oriented normal to the shore with an angle of 298°N and the LST is integrated over the active part of the profile.

The model can be forced with a wave time series of up to 3 parameters (H_{rms}, peak period T_p, and mean wave direction), therefore the sea and swell components from the IFREMER reanalysis at Noordwijk are combined in the same way presented in §4.2. The 20 years of wave data are considered as the forcing boundary condition in the calculation. Following Walstra et al. (2012), waves with directions outside the range $\pm70°$ relative to the shore normal are truncated to $\pm70°$.

Tides and storm surges are not included in the model, in order to compute just the wave-induced longshore sediment transport. The bottom updating module is switched off in order to estimate the potential sediment transport, assuming that the sediment is always available to be mobilized.

6.2. Model validation

The yearly-averaged longshore sediment transport is presented in Table 6-1, where positive transport is directed northwards and negative transport goes southwards, respectively. A net transport of 1.58 millions of m³/year directed southwards is obtained, which differs from previous studies. For instance, van Rijn (1997) computed a yearly-averaged net sediment transport at Noordwijk of 250,000m³/year directed northwards. In order to find the origin of this difference, the longshore sediment transport is recomputed using wave time series from 2 measurement stations from Rijkswaterstaat: YM6 and MPN.

Table 6-1: Yearly-averaged longshore sediment transport from IFREMER wave reanalysis.

Transport	Longshore Sediment Transport [Mm³/year]
Gross - Northwards	1.350
Gross - Southwards	-2.933
Net transport	-1.583

The location of the 2 measurement stations is shown in Figure 6-1. YM6 is the closest to the "Noordwijk" node from IFREMER, while MPN is the closest to the shore. Wave time series at YM6 spans from 1979 to 2008, and MPN wave data covers from 1979 to 2002. The wave climate at each station and the corresponding IFREMER wave climate for the common period are shown in Figure

6-2: upper panels present the wave roses in terms of H_s for the IFREMER node in the period 1979-2008 and YM6, while lower panels show the same information of MPN and the IFREMER node in the period 1979-2002. Directions outside the range $\pm70°$ relative to the shore normal are included as $\pm70°$.
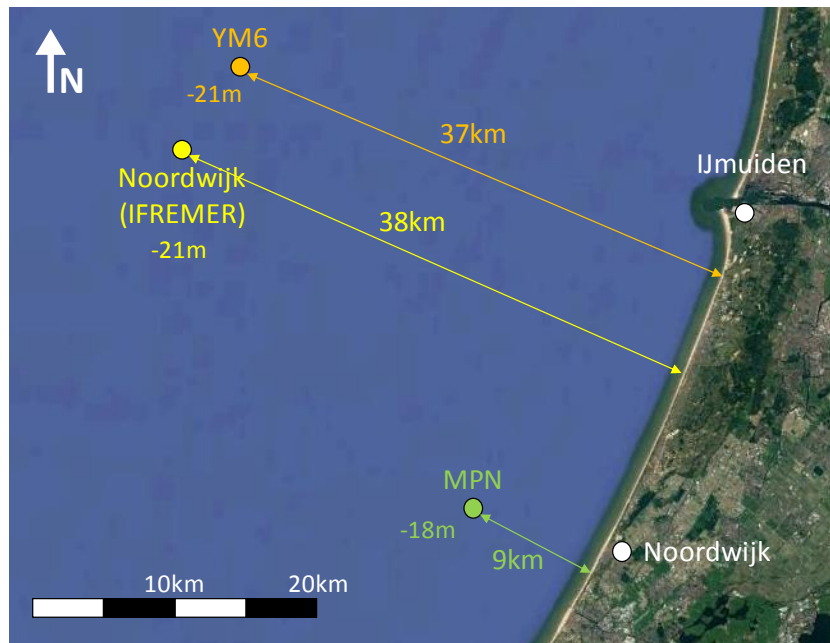

Figure 6-1: Location of measurement stations and IFREMER node.
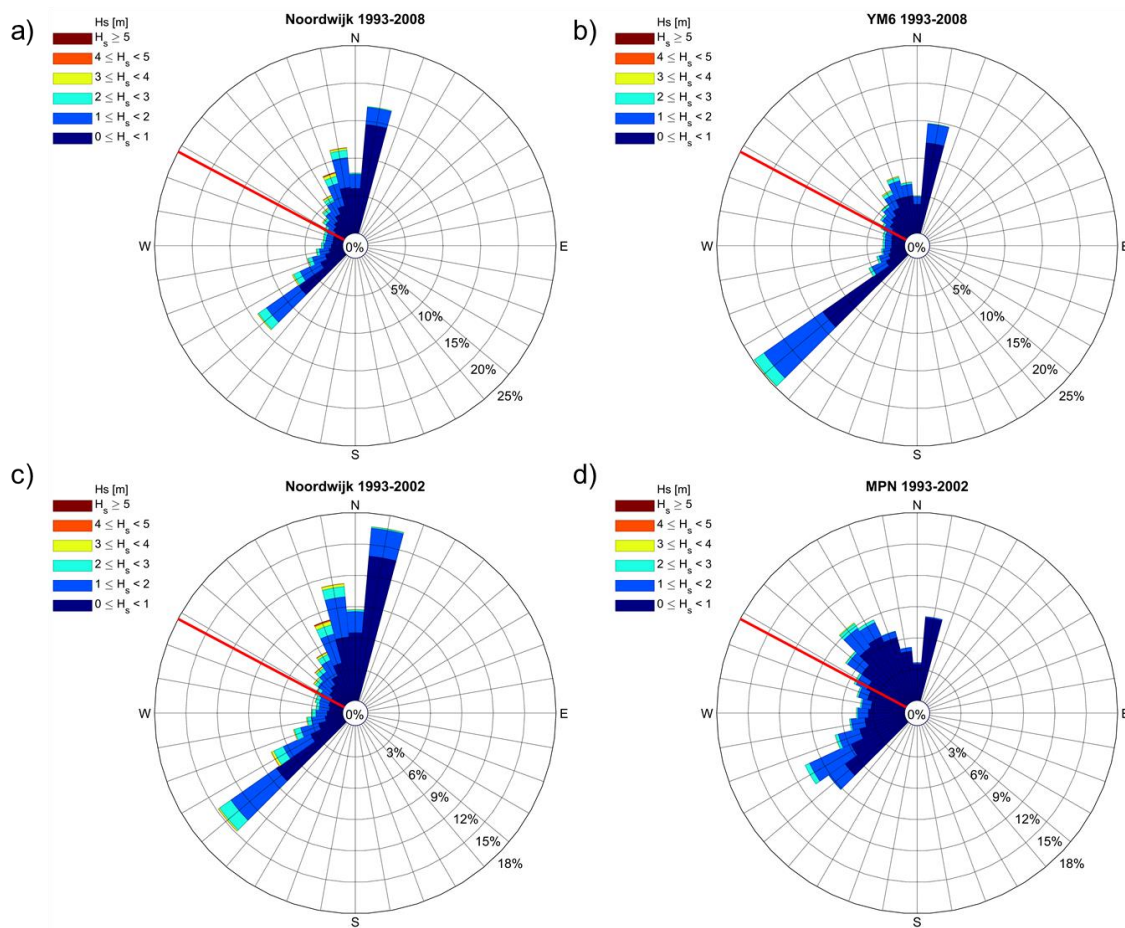

Figure 6-2: Wave roses for common periods for: a) Noordwijk and b) YM6, c) Noordwijk and d) MPN.

From Figure 6-2, it can be seen that northern waves with higher H_s predominate in IFREMER data, explaining the direction of the net longshore sediment transport to the south. This is not that clear in the wave climates from the two stations, where the occurrence of waves relative to the shore normal seems to be more balanced. This behavior can also be observed when computing the yearly-averaged longshore sediment transport using the different wave time series. As it is summarized in Table 6-2, the net sediment transport from IFREMER data is directed southward and the magnitudes are 5-6 times larger than the values obtained for YM6 and MPN.

It is important to notice the directions of the net LST computed from the measurement stations: while the net LST goes northwards at MPN, it is reversed at YM6, being coherent with the direction estimated using the IFREMER data. As YM6 is close to the IFREMER node, this suggests that wave nearshore processes must be taken into account in order to improve the characterization of the wave climate arriving to Noordwijk, especially in the active zone of the profile.

The existence of an inversion point of the longshore sediment transport has also been reported in previous studies and it has been located slightly to the north of IJmuiden (van Rijn, 1997).

Table 6-2: Yearly-averaged LST in millions of m³/year from the different wave climates.

Transport	IFREMER	YM6	IFREMER	MPN
Gross - Northwards	1.457	0.913	1.603	0.579
Gross - Southwards	-3.260	-1.210	-3.021	-0.352
Net transport	-1.803	-0.297	-1.418	0.227

Despite the difference in the net LST direction between the IFREMER node and MPN, the longshore sediment transport for the historical period and the future scenario are estimated using the IFREMER wave data, in order to illustrate the application of the methodology to assess the effect of climate change.

6.3. Distribution of LST per WT

Following Cánovas (2012), the daily cumulative longshore sediment transport for each weather type is computed using the IFREMER reanalysis. Then, the distribution of the daily LST associated to each WT is obtained, as it is presented in Figure 6-3. Weather types with a relevant wind sea component, located at the left side of the lattice, show an important LST directed northwards. On the other hand, when the sea component is less present, swell waves coming from the north dominate and the LST goes southwards, as it is observed in the right side of the lattice.

6.4. Longshore sediment transport as a metric of change

As it was explained in the previous chapter, differences between the occurrence probability of the weather types estimated using different models or time periods may be small in absolute terms, but these small differences can represent changes up to 60% in relative terms. In order to determine whether these differences are significative or not for coastal processes, a metric is needed. One option is considering the longshore sediment transport as a measure of the relevance of the changes in the occurrence of the weather types. Therefore, the calculation of the LST for the historical period and the future scenario are required.
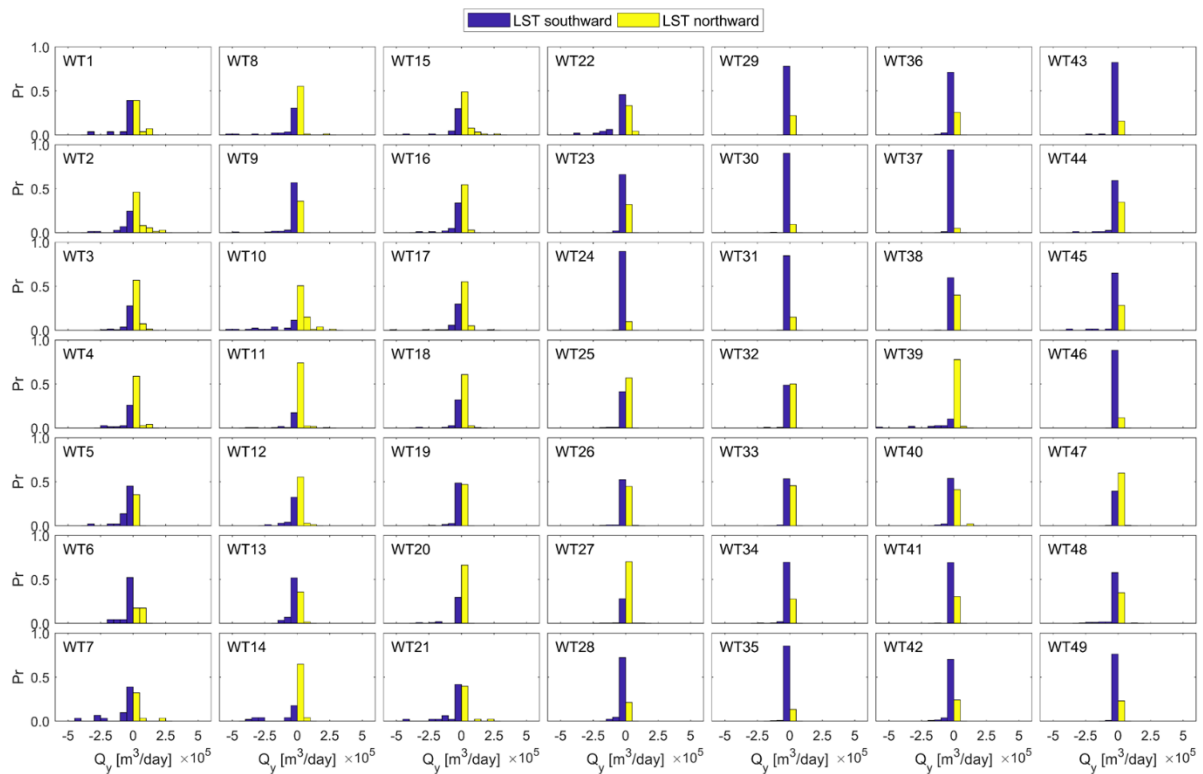
Figure 6-3: Distribution of LST in m³/day related to each WT.

One way to estimate the longshore sediment transport consists of weighting the distribution of LST computed for each weather type by the corresponding probability of each WT, and then integrating over the WTs to come up with yearly-averaged gross and net longshore sediment transports. Two comparison are presented: firstly, LST is computed using the weather types' probabilities from CFSR and ACCESS1.0 to validate the climate model, and secondly, probabilities of WTs from ACCESS1.0 for the historical period and the future scenario are considered in order to determine the magnitude of changes in the gross and net LSTs.

6.4.1. Historical period

Figure 6-4 shows the distribution of total gross LST and the yearly-averaged gross LST related to each WT, considering the occurrence probability of the WTs from CFSR and ACCESS1.0 for the common period. Differences in the weather types, depicted by the black lines in panel b), are more significant for the weather types located at the left of the lattice, related to low-pressure systems which are present during winter. Conversely, weather types associated to summer conditions, located at the right side of the lattice, show smaller gross LSTs and also smaller differences between reanalysis and climate model.

Predominance of LST directed southwards is clearly seen in most of the weather types and confirmed in the total yearly-averaged gross LST shown in panel c). Total gross and net LSTs obtained from CFSR and ACCESS1.0 look similar, and therefore it is concluded that the climate model provides a sound representation of the recent past, to be compared with the future projection.
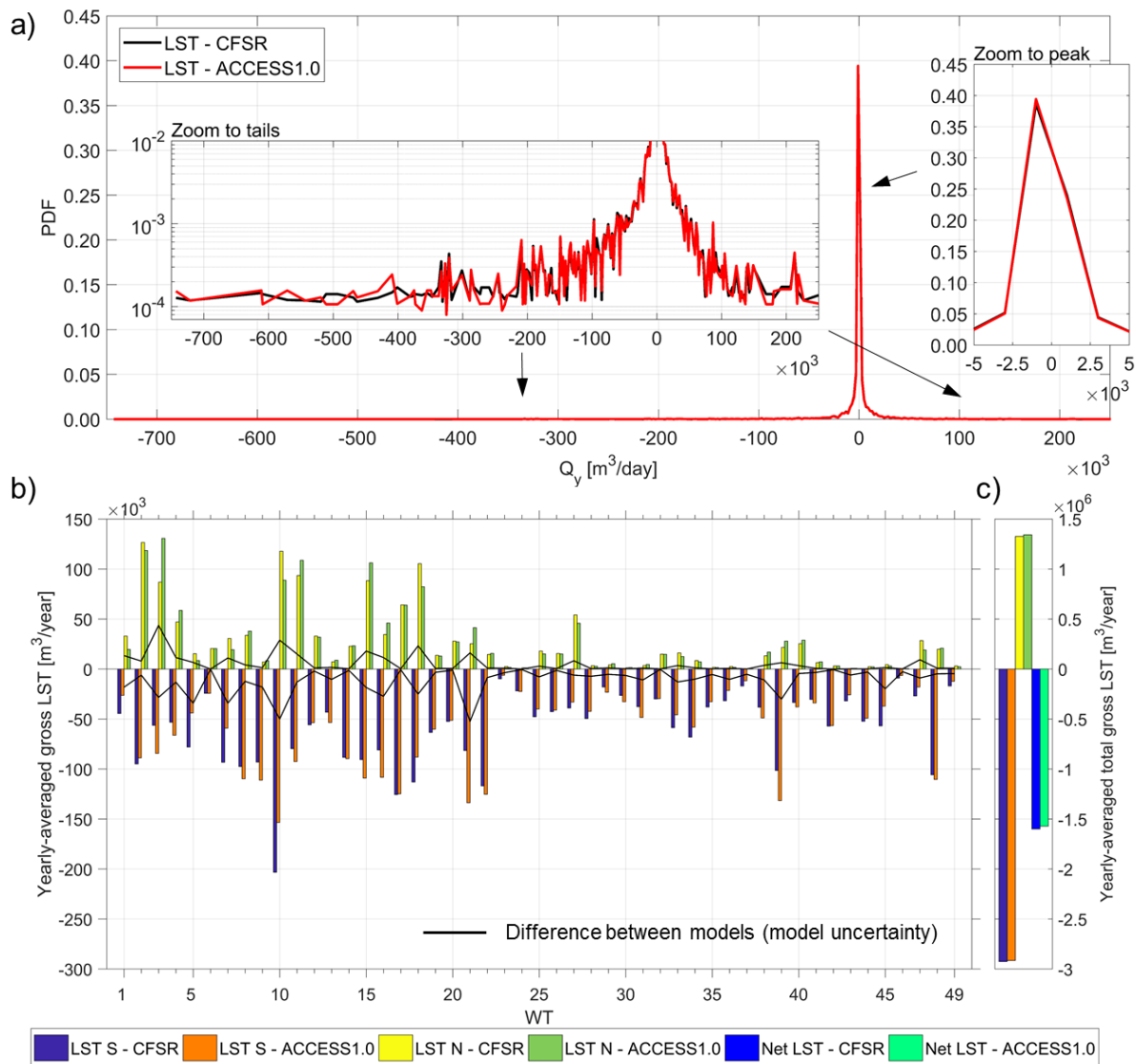
Figure 6-4: a) Distribution of total gross LST in m³/day estimated for CFSR and ACCESS1.0 for the recent past (1979-2005); b) yearly-averaged gross LST associated to each WT and c) yearly-averaged total gross and net LST estimated for CFSR and ACCESS1.0 for the recent past (1979-2005). Black lines indicate the difference between both models for each WT.

6.4.2.   Changes in future scenario

In the same way, Figure 6-5 shows the distribution of total gross LST and the yearly-averaged gross LST associated to each WT, considering the occurrence probability for the historical period and the future scenario, both from ACCESS1.0. Black lines depict the differences between CFSR and ACCESS1.0 for the recent past, as it is shown in Figure 6-4, to provide an idea of the model uncertainty, given the fact that just one climate model has been included in the analysis. Red lines show the differences in gross LST between the historical period and the RCP8.5 scenario during the period 2070-2099. A significative increase of the southwards LST is observed for WT8, WT9, WT10 and WT48, which is counteracted by a decrease in WT15, WT21 and WT22, giving a sligthly smaller total gross LST directed southwards in the future scenario, compared to the recent past, as it is shown in panel c).

Regarding the gross LST directed northwards, a decrease in WT15 is balanced by an increase in WT10. Changes in the rest of the weather types lead to a decrease in future total gross LST directed

northwards, as it is shown in panel b). This decrease is responsible for the increase of the net LST southwards. A detailed explanation of the observed changes is given in the next chapter.
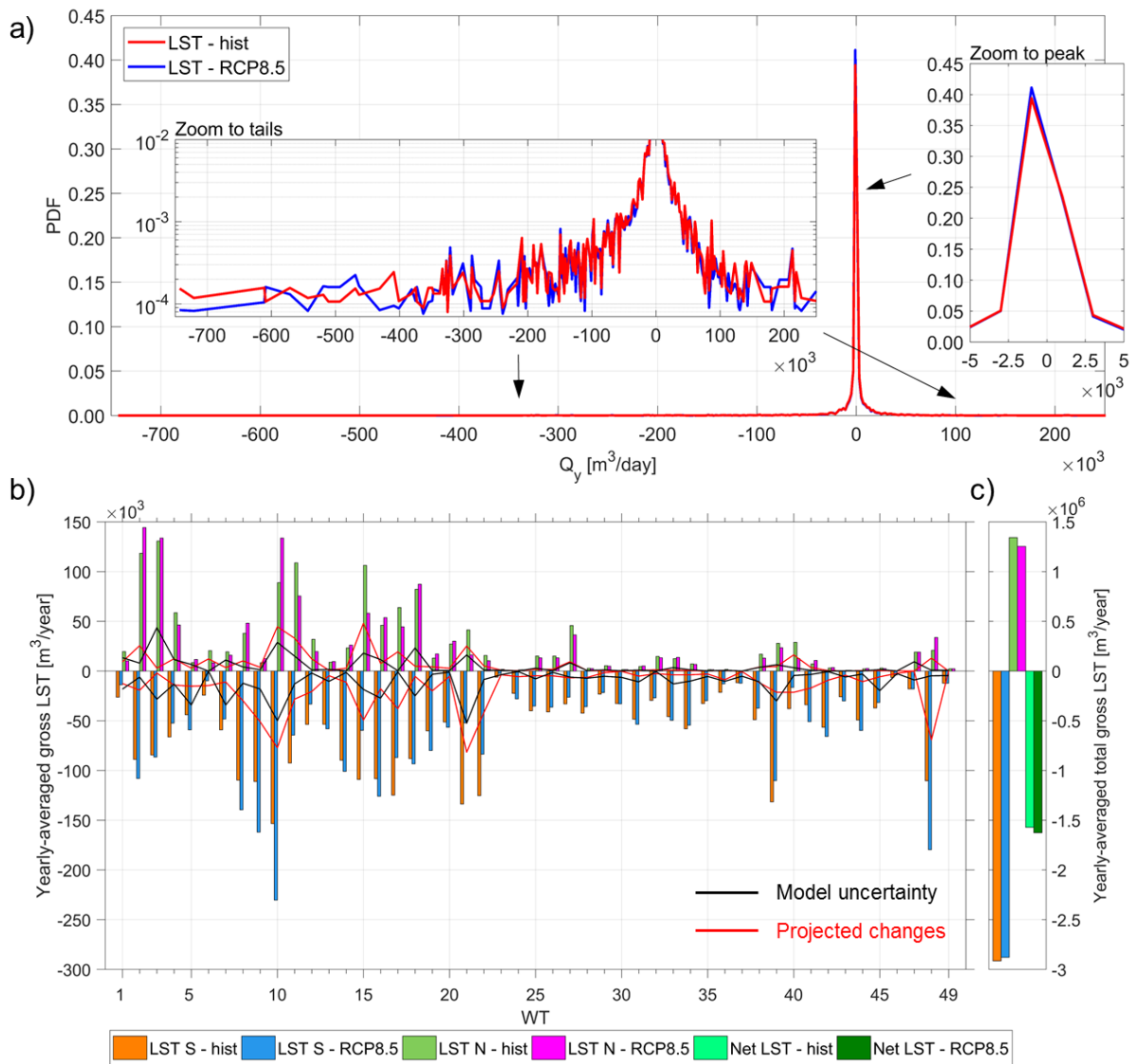
Figure 6-5: a) Distribution of total gross LST in m³/day estimated for historical period and future scenario; b) yearly-averaged gross LST associated to each WT and c) yearly-averaged total gross and net LST estimated for historical period and future scenario. Black lines indicate the difference between both models for each WT for the recent past, and red lines depict the difference between historical period and future scenario.

In this chapter a more detailed explanation is given regarding the results presented in the previous chapters.

7.1. Weather-type based wave climate modeling

7.1.1. Weather types

One of the main advantages of the statistical downscaling approach followed in this work is the relation established between the predictor and the predictand, particularly, the SLP fields and the wave climate, which has been characterized by bulk parameters of different partitions. Grouping the wave climate according to similar atmospheric conditions over the wave generation area, namely weather types, offers a robust tool to understand the wave climate arriving to the location of interest. Of course, the classification is determined by the selected number of weather types, which fulfills the compromise between a significant number of clusters for the predictor and a minimum number of wave data per group.

The relation between the atmospheric patterns and the wave climate is summarized in Figure 7-1 by reproducing some previous figures, where the 49 weather types and the significant wave height, peak period and mean wave direction for the sea and swell component are shown in the different panels. Panel a) presents the dynamic predictor, which shows the spatial and temporal distribution of high and low-pressure systems that are relevant for the generation of waves reaching Noordwijk, as the predictor was built using the isochrones of the wave energy travel time. Weather types on the left side of the lattice correspond to low-pressure systems, with strong SLP gradients over the Greenland and the Norwegian Seas and milder gradients over the North Sea, as it is depicted in the right panel in Figure 4-7. On the other hand, high-pressure systems are located on the right side of the lattice, with smoother SLP gradients over the whole domain except for weather types on the top right corner of the lattice.

According to seasonal occurrence probability of each WT shown in panel e) of Figure 7-1, the weather types from the right side of the lattice are more present in summer, while the weather types located on the left bottom of the grid are likely to occur just during the winter. These results are consistent with the weather types obtained by Camus et al. (2014b) for the North Atlantic region.

Low-pressure systems are associated with important sea component, as it can be inferred from panel b) of Figure 7-1. This component of the wave climate is significantly reduced in weather types from the right side of the lattice. During summer, milder conditions are expected in the whole North Atlantic basin, leading to less generation of waves arriving from the English Channel. Conversely, low-pressure systems located in front of the English and French coasts are responsible of the generation of the waves reaching Noordwijk from the west. The swell component is present in all the weather types, but reduces significantly in WT3, WT10, WT11, WT18 and WT39. This might be explained by the presence of weaker systems near the Arctic.

Panel c) from Figure 7-1 reveals that low-pressure systems on the left side of the weather-type lattice are driving sea states with higher $H_{s_{sea}}$, see for instance WT15 or WT17. WT39 also has important wave heights for the sea component, despite its location on the right side of the lattice. The large values of $H_{s_{sea}}$ and $T_{p_{sea}}$ in WT39 are associated with winter events, as it is concluded from the seasonal occurrence probability of this weather type in panel e) of Figure 7-1. In general terms,

low-pressure systems are associated with more energetic sea waves, as the joint distribution of $H_{s_{sea}}$ and $T_{p_{sea}}$ reveals: the most probable values for the significant wave heigths are in the range $2-4m$ and for the periods lay between $6-8s$ for WTs on the left side of the lattice. Conversely, in the right side of the lattice, the most probable values for the significant wave heights are lower than $2m$ and for the peak periods lay between $4-6s$ respectively.
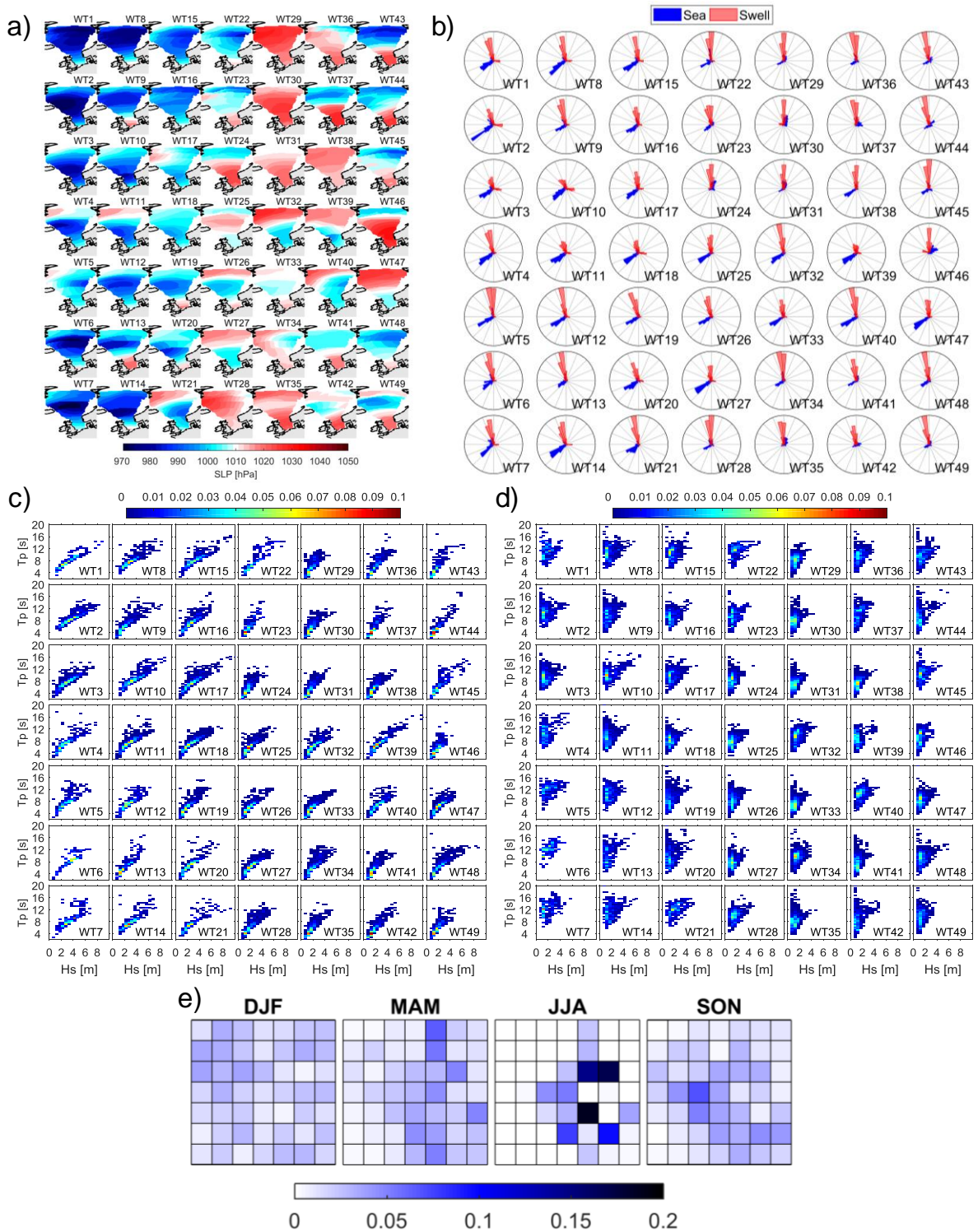

Figure 7-1: a) Weather types for the atmospheric classification, b) empirical distribution of mean wave direction per WT, empirical joint distribution of H_s and T_p per WT for c) sea component and d) swell component, e) seasonal occurrence probability associated to each WT.

Panel d) of Figure 7-1 depicts the joint distribution of $H_{s_{swell}}$ and $T_{p_{swell}}$, where it can be seen that the most probable values for the significant wave heights are in the order of 1-2m, with maximum values up to 6m in WT10. In the case of $T_{p_{swell}}$, the most probable values are ranging between 8s and 12s.

7.1.2. Time scales

7.1.2.1. Intra-daily scale

As it was shown in §4.8, the emulator of daily weather types represents adequately the chronology of WTs at different time scales: inter-annual, seasonal, monthly and daily. The chronology of the weather types determines the chronology of the waves at all the mentioned time scales, but one is missing: the intra-daily scale, as the waves are to be generated every 3hrs.

The way the statistical model has been built, a daily value of a certain weather type defines the copulas and the marginal distributions which have to be used to generate 8 synthetic multivariate vectors of wave parameters (temporal resolution of 3 hrs). In the model, there is no variable that controls the sequencing of the wave parameters at the intra-daily scale, and the generation of a calm sea state followed by a very large H_s in the next 3 hours might happen due to the stochastic character of the wave emulator.

For long-term morphodynamic evolution, the temporal order of the sea states may be relevant, depending on the response of the system to wave forcing. If the same amount of storms are preserved, which is guaranteed by the marginal distribution of each wave parameter and the multivariate dependence given by the vines, then the lack of an intra-daily scale modeling is not undermining the applicability of the weather type based statistical model. Nevertheless, if the study aims to model the impact of storms on the morphology of the coast, then some assumptions about the intra-daily distribution of the wave parameters is required. For instance, one popular but simple approach is assuming a triangular distribution for the variable of interest, as it is shown for instance by Rueda et al. (2016c).

The modeling of the intra-daily scale is a matter of ongoing research. One promising approach is the application of time-varying vine-copulas, where the multivariate dependence between variables is modeled as a stochastic process in time using Markov properties. An interesting review is given by Jäger and Morales Nápoles (2017) with an application for time series of significant wave heights and mean zero-crossing periods in the North Sea.

7.1.2.2. Interannual variability

Validation of the emulator of daily weather types also showed that the interannual variability of the climate is captured by the chronology model. In the particular case of this thesis, a Markov term of order 1 was sufficient, but there are cases where this term (or one of higher order) is not enough and the introduction of covariates is needed, as it was explained in §2.1.4.

One alternative consists of using a set of monthly weather types, which are obtained applying the same classification techniques (K-means algorithm, for instance) to the Principal Components (PCs) of the predictor at a monthly scale. In this sense, the collection of monthly weather types represent synoptic patterns of larger time scale which in turn define the occurrence of the daily weather types. Usually, the monthly weather types represent climate indices such as the North Atlantic Oscillation (NAO) or the East Atlantic Oscillation (EA), to name a few.

An application of monthly weather types is given by Rueda et al. (2017), who considered 9 monthly weather types in a statistical downscaling for a location in Southern California. In their work, the

sequencing of the monthly WT was extracted from the historical realization of the climate during the period 1979-2009. In a deterministic approach, considering the historical sequence of monthly weather types allows to reproduce the interannual variability exactly as it is observed in the historical realization, resembling a hindcast. A fully stochastic approach should consider a chronology model for the monthly weather types, which in turn will drive the chronology model of the daily weather types.

7.1.3. Multivariate copulas

Recent works have shown the good performance of Gaussian copulas to model the multivariate distribution of wave parameters (Rueda et al., 2017) and the ability of the AC skew-t copula to incorporate the skewness of the bivariate distribution of significant wave height and peak period introduced by the physical limit of the wave steepness (Jäger & Morales Nápoles, 2017). One of the main contributions of this thesis is combining the advantages from both approaches through the application of the so-called vine graphical model.

Despite the good results obtained for the multivariate dependence model, it is important to clarify the interpretation of the AC skew-t copula. Jäger and Morales Nápoles (2017) justified the use of the AC skew-t copula because it captures the physical limitation on wave steepness due to wave breaking, and this argument is valid when the random variables correspond to bulk wave parameters. Originally, the wave steepness condition was defined for regular waves and then the concept was extended for sea states, therefore this condition is unique for a given sea state. Consequently, the use of AC skew-t copulas for the sea and swell components may not be justified in terms of a wave steepness condition but indeed as a good representation of the asymmetry found in the empirical joint distributions.

To illustrate the good performance of the AC skew-t copula in the vine-copula approach adopted in this work, a climate-based stochastic simulation was run considering a trivariate vector for each sea state consisting of bulk wave parameters (H_s, T_p, Dir), which was created using the sea and swell components. In this case, the use of the copula is justified in terms of the inclusion of the wave steepness condition and the agreement with the observed distribution is satisfactory, as it is shown in Figure 7-2, where the density of the simulated joint distributions consider 100 samples.

To show the better performance of the AC skew-t copula compared to the Gaussian copula, the same stochastic simulation was carried out using the latter copula for the bivariate distribution of H_s and T_p. The results are shown in Figure 7-3, where it can be seen that the lower envelope of the simulated data is not as sharp as it is appreciated in the observed data.

It is important to highlight that the better results obtained using the AC skew-t copula are at expenses of a higher computational cost due to numerical implementation of the conditional copulas and their related inverse functions. A vine based on Gaussian copulas is equivalent to the multivariate Gaussian distribution and therefore the sampling procedure is straightforward, saving a lot of computational time.
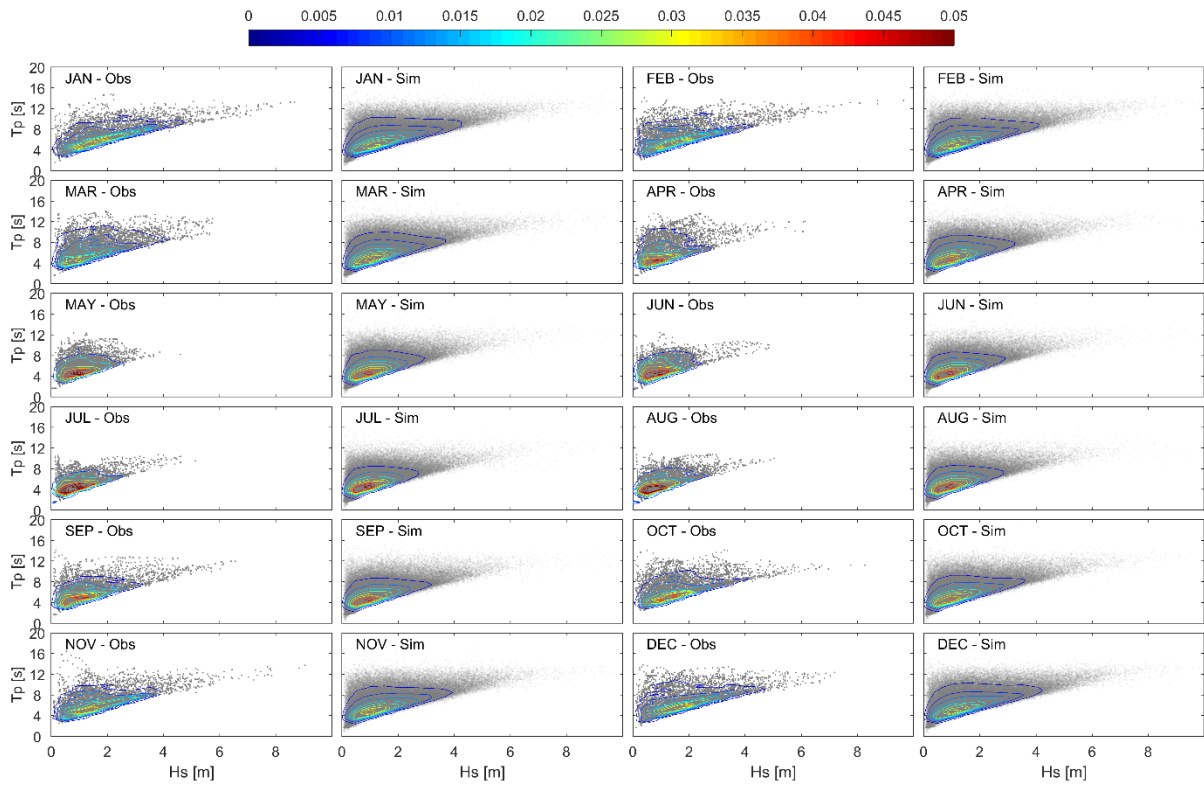
Figure 7-2: Joint probability density of the bulk pair $H_s - T_p$ using the AC skew-t copula, sorted by months. Simulated values correspond to 100 simulations. Joint probability density is shown by colored contours.
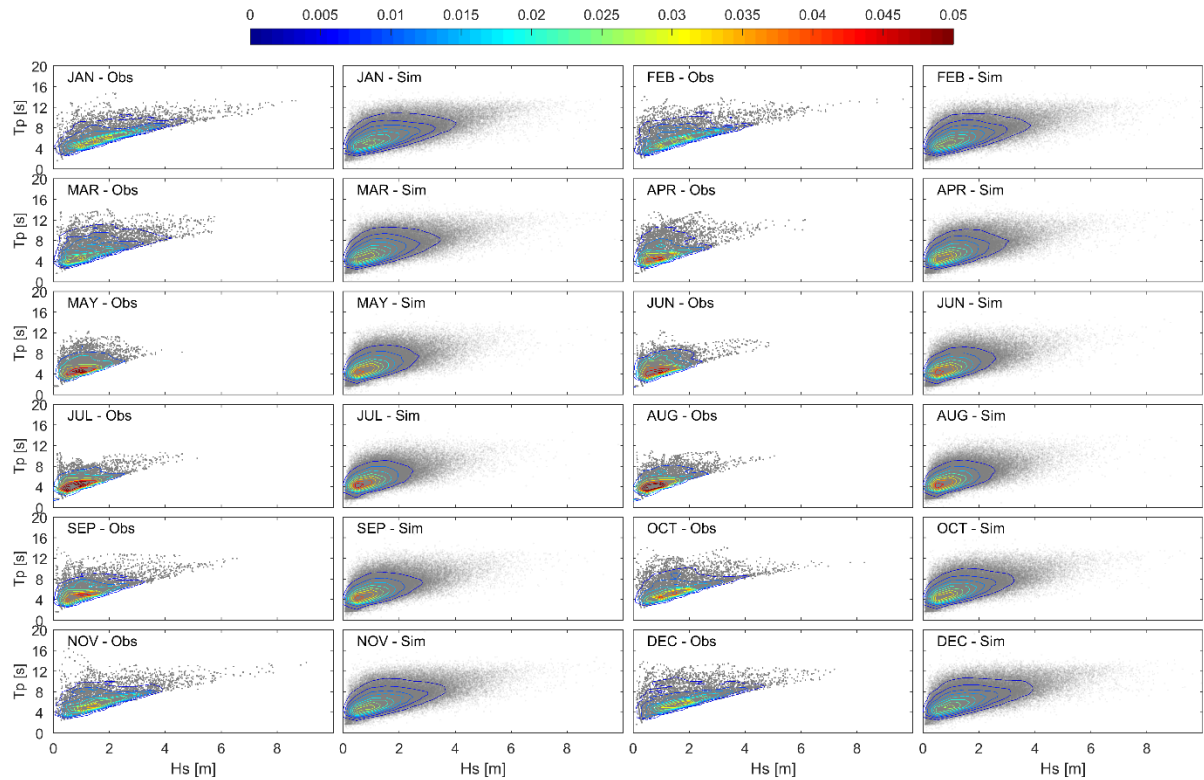

Figure 7-3: Joint probability density of the bulk pair $H_s - T_p$ using the Gaussian copula, sorted by months. Simulated values correspond to 100 simulations. Joint probability density is shown by colored contours.

7.2. Future wave climate

7.2.1. Validation of GCM ACCESS1.0

The GCM ACCESS1.0 has been proposed by Pérez et al. (2014b) as one of the most skilled model, among others, to represent the climate dynamics over the Northeast Atlantic region. Further research from Wang et al. (2014) and Pérez et al. (2015) have succesfully proven the good perfomance of ACCESS1.0 when applied in statistical downscaling of wave climate from atmospheric variables.

According to Pérez et al. (2014b), the CMIP5 model ACCESS1.0 was given a scatter index $SI = 0.33$ and a relative entropy $RE = 0.19$ when compared with atmospheric data from the NCEP/NCAR Reanalysis I for a reference period between 1961 to 1990 and considering 100 weather types. Additionally, the data from the mentioned reanalysis was also compared with ERA-40 reanalysis and with the NOAA-CIRES twentieth Century Reanalysis V2 for the same reference period, resulting in scores of $SI = 0.16$, $RE = 0.10$ and $SI = 0.26$, $RE = 0.14$, respectively, which means that different reanalyses lead to similar characterization of the occurrence rate of synoptic patterns. For further details the reader is referred to Pérez et al. (2014b).

Later, Pérez et al. (2015) repeated the assessment for ACCESS1.0 considering the atmospheric data from the CFSR reanalysis for the reference period $1979 - 2004$, obtaining scores of $SI = 0.49$ and $RE = 0.22$ for a classification comprising 100 weather types over the Northeast Atlantic Ocean and the Mediterranean Sea.

In this thesis, which has considered a reduced spatial domain, the performance of ACCESS1.0 was graded with a scatter index $SI = 0.27$ and relative entropy $RE = 0.19$. These values are in agreement with the scores obtained in the previous studies and therefore the model capability to reproduce the climate dynamics over the North Sea during the recent past is accepted.

7.2.2. Changes in future scenario

The performance of ACCESS1.0 for the future scenario was valued with a scatter index $SI = 0.31$ and a relative entropy $RE = 0.22$, being both values slightly larger than the same metrics for the historical period ($SI = 0.27$ and $RE = 0.19$). It is important to notice that sample sizes are different in both periods: the historical one comprises 27 years and the future scenario, 30 years. This difference of 3 years between both datasets may be statistically relevant and explain the observed increase in both metrics. In order to elucidate this, a test of significance could be undertaken.

Nevertheless, in order to quantify these changes, the longshore sediment transport was considered as a metric. Changes in the estimated gross and net longshore sediment transports are explored in the following section.

7.3. Morphological simulation

7.3.1. Differences in net LST direction

Two important differences arise when comparing the longshore sediment transport computed from IFREMER data and from measurement posts (YM6 and MPN): 1) the magnitudes of gross and net LSTs, and 2) the direction of net LST. The first difference can be explained in terms of the wave heights, which are larger in the IFREMER time series compared to the measured wave time series, and this problem can be solved by calibrating the IFREMER wave climate against the YM6 or MPN information.

The second difference poses a more complex problem, because the net LST from IFREMER is directed southwards, being opposite to the net LST estimated using the MPN wave times series or in previous studies, such as van Rijn (1997). The location of the IFREMER node respect to the coast (38km offshore) suggests that there is enough fetch for the development of additional wind sea waves, which in turn could enhance the transport northwards. One way to confirm this hypothesis corresponds to the application of a hybrid approach [see for instance Antolínez et al. (2016b) or Antolínez et al. (2016c)], where the downscaled wave climate is used as input for a wave model (like SWAN, for instance), in order to improve the characterization of the nearshore processes and include the potential wind sea arriving to the coast. This is very important as the wave-induced longshore sediment transport is concentrated in the surf-zone, close to the shore.

Although Unibest-TC already incorporates wave nearshore processes, some spatial (2DH) features might play a rol and Unibest-TC is unable to reproduce them accurately. Despite this limitation, the work presented in this thesis is a valuable methodology to quantify the potential changes in wave climate induced by a global-warming forced climate change.

7.3.2.   Changes in future LST

A simplified approach was selected to quantify the effect of climate change in the longshore sediment transport, in which the distribution of LST related to each WT was weighted by the probability of occurrence of each WT estimated using the predictor from ACCESS1.0 for the recent past and the RCP8.5 scenario during 2070-2099.

Figure 7-4 aims to summarize the analysis by reproducing previously presented figures, to provide a comprehensive explanation of the changes in longshore sediment transport. In panel a), the yearly-averaged gross LST associated to each WT is shown. Black lines depict the differences between CFSR and ACCESS1.0 for the recent past, to give an idea of the model uncertainty. Red lines show the differences in gross LST between the historical period and the future scenario. Panel d) show the empirical distribution of the overall mean wave direction, as this parameter was considered for the runs in Unibest-TC.

A significative increase of the southwards LST is observed for WT8, WT9, WT10 and WT48, which are linked with the larger increases in occurrence probability, as it is derived from panel e). These WTs show an increase of probability in the order of 50%, which is relevant for the southwards LST. On the other hand, WT15, WT17, WT21 and WT22 are characterized by a decrease in the LST directed southwards, explained by a decrease in probability in the order of 30–50%. Both weather types have waves coming mainly from the north, explaining the reduction in the southwards LST.

Regarding the gross LST directed northwards, WT2 and WT10 exhibit the largest increases in magnitude, explained by the increase in corresponding occurrence probabilities (around 20% and 40%, respectively). Looking at panel d), it can be seen that both weather types have an important westerly component, related to wind sea. Conversely, the more significative decreases in northwards LST are observed for WT15, WT21 and WT22, which are less likely to occur in the future scenario, as it is deducted from panel e). Waves from WT15 also have an important wind sea component, which could explain the reduction observed in the northwards LST.

The total yearly-averaged gross and net transports are presented in panel b), where a slightly increase in the net LST is observed, due to a larger reduction of the total gross northwards LST compared to the decrease in the total gross southwards LST.
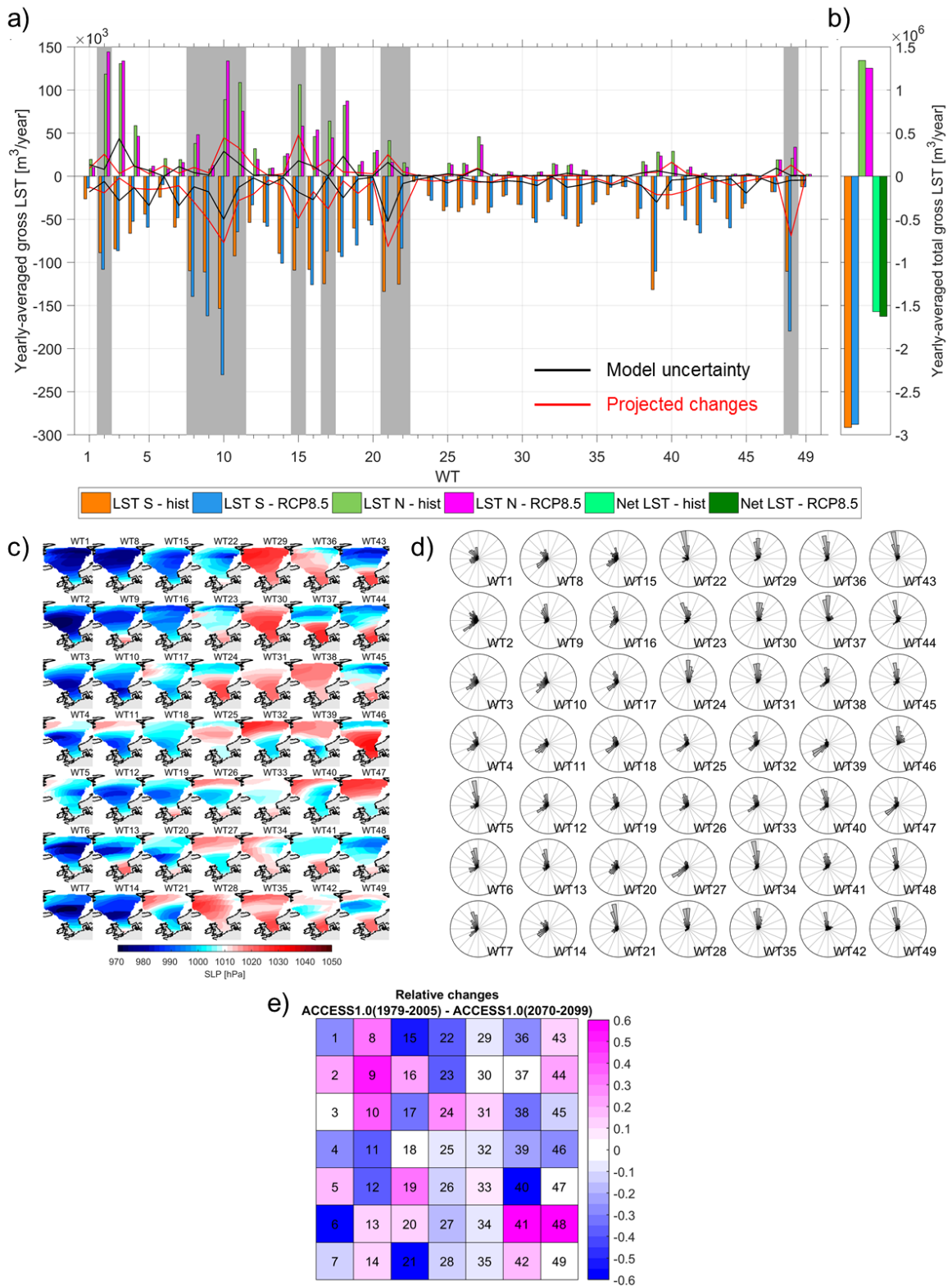
Figure 7-4: a) Yearly-averaged gross LST associated to each WT. b) yearly-averaged total gross and net LST estimated for historical period and future scenario. Black lines indicate the difference between both models for each WT for the recent past, and red lines depict the difference between historical period and future scenario. c) Weather types for the atmospheric classification. d) Empirical distribution of overall mean wave direction per WT. e) Changes in occurrence probability of each WT relative to historical period.

The red lines in panel a) also confirm that the most important changes in yearly-averaged LST are observed for WT2, WT8, WT9, WT10, WT11, WT15, WT17, WT21, WT22 and WT48 (highlighted in gray in the figure). The first four weather types show an increase in the occurrence probability and they represent waves with a wind sea component from the west, suggesting an increase of westerly waves which are relevant for longshore sediment transport. This result is in line with recent studies, which have demonstrated that annual extreme wind events are coming more often from western directions in the future scenario, compatible with a poleward shift of the North Atlantic storm track (de Winter et al., 2012; de Winter et al., 2013; Haarsma et al., 2013).

Black lines in panel a) represent the difference in gross LSTs between CFSR and ACCESS1.0 for the historical period, giving an idea of the model uncertainty present in the modeling (as it was previously mentioned, just one climate model has been considered and this is the only possible way to estimate the model uncertainty up to this point). When comparing the changes in the future scenario, it can be seen that the red lines lay close to the black lines in some weather types, suggesting that potential changes in the future might be comparable to the model uncertainty instead of representing a real change in the signal. Accordingly, it is important to identify the sources of uncertainty in order to reduce them and improve the confidence on the methodology.

In the proposed methodology, model uncertainty come from 4 different sources:

1) Models for the predictor.
2) Models for the predictand.
3) Morphodynamic models.
4) Natural variability of the climate.

Regarding the predictor, the statistical model was developed using the information from CFSR reanalysis and the comparison with the future scenario was performed considering the outcomes from one global circulation model. As it was shown in chapter 5, the representation of the recent past from both models are similar but not identical, introducing differences in the results. This problem may be overcome considering an ensemble of CMIP5 models, in order to quantify the differences between climate models and the CFSR reanalysis for the historical period. Even the model uncertainty can be quantified using another reanalyses for the statistical model of the predictor, like NCEP/NCAR Reanalysis or ERA-Interim.

The same situation can be observed for the predictand. IFREMER reanalysis was selected for the statistical model of the predictand, and the uncertainty could be quantified comparing with another sources of information.

The third source of uncertainty is related to the formulation of sediment transport included in the process-based model, in this case Unibest-TC. Other models with different formulations may lead to different values for the computed longshore sediment transport, and usually the spreading between sediment transport formulations is large. This source of uncertainty can be counteracted by calibration of the selected model and it is thought to be of less importance compared to the two previous uncertainty sources, as the predictor describes the climate which in turn drives the forcing waves, responsible of the longshore sediment transport.

Another source of uncertainty present in the problem is the natural variability of the climate. In this work, a simplified deterministic approach was selected to estimate the distribution of LST associated to each WT, corresponding to the historical realization of the climate, and therefore the natural variability of the climate has not been fully incorporated. A more comprehensive approach should include a fully stochastic simulation of weather types and hence waves, using the climate emulator formulated in chapter 4. de Winter et al. (2012) have found no significant changes in H_s and T_m of extreme waves arriving to the central Dutch coast for the period 2070-2100, suggesting that wave

climate will be similar in a future scenario and then the chronology of events becomes relevant. In this sense, the chronology of weather types may play an important role driving changes in longshore sediment transport, and a fully stochastic simulation may help to identify the influence of the natural variability of the system.

7.3.3. Morphology vs morphodynamics

In this work, the longshore sediment transport has been chosen as a proxy for changes induced by climate change, and the selected approach consisted of running the process-based model Unibest-TC not allowing for bed changes, in order to estimate the potential longshore sediment transport along the coast. This represents a morphological approach, as a morphodynamic simulation would include the calculation of erosion/deposition in the sea bottom.

Results from a morphodynamic simulation may be different, because of the inclusion of the feedback between the hydrodynamic conditions and the bathymetric changes, which drives the bed level evolution. These bathymetric changes can, for instance, modify the wave breaking point due to bar migration, affecting the location and magnitude of the wave-induced currents and therefore the longshore sediment transport.

The relationship between the bed level evolution and the wave climate plays an important role in the morphology of a coastal system. Changes in erosion/deposition areas along the coast may modify the location of wave breaking and therefore the surf zone width, inducing gradients in the alongshore sediment transport. Moreover, these gradients may enhance the erosion/deposition processes, leading to changes in the orientation of the coast, modifying the shore normal and therefore the angle of obliquity of the incoming waves, thus altering the longshore sediment transport and finally the morphological evolution of the coast. This effect may not be significant for straight stretches as the central Dutch coast, but may be very relevant for bays or curved coastlines.

A similar behavior may be expected in presence of disturbances along the coast, such as natural features as rivers, deltas or tidal basins, or human interventions such as coastal structures, namely harbour moles, shore protection structures, river regulation works, nourishments schemes or maintenance dredging (Bosboom & Stive, 2015).

7.4. Applicability of a weather-type based methodology

Several previous works and the results from this thesis have demonstrated that the weather-type based climate classification is a reliable tool to analyze the wave climate at the location of interest. This methodology may be applied in any location where the following criteria may be fulfilled:

- Find a location for the definition of the predictand, offshore enough to avoid the effects of wave propagation in shallow waters (shoaling, refraction, bottom friction, breaking). This processes will add noise to the statistical relationship, making it not "clean". Also wave diffraction due to sheltering by obstructions shall be avoided.
- The node where the predictand is defined should also be close enough to the shore in order to assume that the wave climate is representative of the coastal conditions, i.e., there is no time lag between the offshore conditions and the surf zone.

The climate emulator developed in this thesis is a powerful tool to hindcast historical wave climate or project future wave climate at the location of interest. The emulator could also be used to generate synthetic wave climate for stochastic simulation in offshore an coastal projects.

8. Conclusions

8.1. Conclusions

The main objective of this thesis was to assess the impact of climate change on the long-term longshore sediment transport at Noordwijk, selected as a representative location of the central Dutch coast. With this premise in mind, the main effort was concentrated in formulating a reliable tool to characterize the present wave climate and project the future wave climate at Noordwijk.

In this thesis, a statistical downscaling approach was followed to establish a relation between atmospheric variables at regional scale, namely the predictor, and local scale met-ocean variables, known as the predictand. The model is based on a classification procedure of the predictor into similar atmospheric patterns over the wave generation areas, namely the weather types. Then, the wave data is grouped according to the occurrence of the weather types.

The predictor was built from the SLP fields and the squared SLP gradients extracted from the CFSR reanalysis. Wave data was obtained from IFREMER reanalysis in front of Noordwijk. Analyses of these databases led to conclude that bimodality dominates the wave climate at the location of interest, with a wind sea component arriving from the English Channel and a swell component reaching from the Greenland and Norwegian Seas.

The temporal evolution of the weather types was modeled using an autoregressive logistic model, which incorporates the seasonality, the interannual variability and the persistence of the weather types, observed from the historical data. On the other hand, the wave climate was parameterized in terms of bulk wave parameters H_s, T_p and Dir for the two wave systems (wind sea and swell), resulting in unimodal or bimodal sea states. Mixed-models, consisting of a non-parametric kernel density function for the central-mass regime and two generalized Pareto distributions for the lower and upper tails, respectively, were fitted to the marginals of H_s and T_p for each wave system in each weather type. This approach was chosen because it improved the representation of the upper tail, compared to other distributions.

The statistical dependence between wave parameters for each sea state was taken into account using a vine-copula approach, where the multivariate dependence structure is modeled using bivariate copulas as building blocks. Based on previous studies, the bivariate dependence between H_s and T_p was modeled using the AC skew-t copula, whereas the rest of the pairs of random variables were considered as Gaussian.

Both statistical models for the predictor and predictand were tested for stochastic simulation. Synthetic series of daily weather types showed a good representation of the seasonality, interannual variability and persistence observed in the historical realization, and synthetic series of 3-hourly bulk wave parameters for sea and swell preserved the statistical structure from the observed data.

After the statistical relation was formulated, the SLP fields from the GCM ACCESS1.0 were processed to generate a future predictor. Comparison of the outcomes of ACCESS1.0 for the historical period (1979-2005) with the CFSR reanalysis demonstrated that the climate model was able to represent the recent past climate and the comparison with projections for the last time slice of the 21st century (2070-2099) under the most severe scenario (RCP8.5) proceeded.

The statistical model was applied to identify changes in the occurrence probability of the weather types in the future, and the importance of these changes was quantified in terms of the

wave-induced longshore sediment transport. A simplified, deterministic approach was chosen to estimate the LST distribution for each WT and afterwards compute changes in gross and net transports given the present and future probabilities of the weather types.

From the work carried out at this point, the research questions can be addressed:

1. *Will the probability of occurrence of atmospheric synoptic patterns (weather types) change in the future? How will it change?*

The results of this thesis suggest that, conditionally on the considered climate model time series, the occurrence probability of the weather types will change in the future, with some occurrence probabilities varying in the range ±60%. On the other hand, changes in the sequence of weather types, in terms of the transition probability matrix and the persistence of each WT are found to be not relevant. The reported shift in wind directions to more westerly directions may explain the increase in the probability of some weather types with an important wind sea component from the west.

2. *How will the longshore sediment transport be affected in the future?*

According to the results and the considered climate model, the most important changes in LST are concentrated in some of the weather types, with changes in the yearly-averaged gross LST explained by changes in the ocurrence probability of the corresponding WTs. For the remaining weather types, the changes are in the order of the model uncertainty. Regarding the yearly-averaged net LST, an increase of the southward directed net LST is observed with respect to the historical period, driven by a decrease in both yearly-averaged total gross LSTs, being the decrease in northward directed LST larger than the decrease of southwards LST.

The results from this thesis have demonstrated that the weather-type based climate classification is a reliable tool to analyze the wave climate at the location of interest. The statistical downscaling also provide a climate emulator that captures the climate dynamics at different time scales (inter-annual, seasonal, monthly and daily scale), which can be used to generate stochastic simulations of the atmospheric and wave climate.

8.2. Further research

Two different but complementary branches for further research are proposed: improving the methodology or assessing the uncertainty involved in the modeling.

Regarding the first branch, the methodology presented in this thesis could be improved addressing the following topics:

- Applying a hybrid approach, where the results from the statistical downscaling are used as offshore hydrodynamic boundary conditions for wave models, in order to obtain a better representation of the nearshore wave climate. This may help to improve the representation of the yearly-averaged gross and net longshore sediment transports.
- As it was discussed in §7.1.2.1, the chronology model lacks of the intra-daily scale, as the weather types are given at daily scale and the waves are to be generated every 3hrs. Solving the intra-daily time scale appears to be a very challenging area of research, as highly sophisticated statistical tools are required in order to get rid of any assumption on the shape of the marginal distributions, for instance, the traditionally assumed triangular distribution of wave height for storms. Advances in this area may contribute to a better modeling of time series of several parameters, especially during storms.

Quantifying the model uncertainty represents a key challenge to improve the confidence on the methodology developed in this thesis. In this sense, the following ideas may be explored:

- An ensemble of global circulations models (GCMs) should be included in order to reduce the model uncertainty and quantify the differences between the recent past and the future scenario. Moreover, an ensemble of realizations from a single model could also be considered to account for the internal climate variability. The relatively low computational requirements of the statistical approach allow a large number of GCMs and climate realizations to be studied. In this thesis, only the most severe scenario was considered, but also additional climate change scenarios might be included.
- Model uncertainty regarding the predictand may be analyzed comparing to different wave reanalysis or measured wave time series.
- The chronology of weather types is thought to be of crucial importance in the future longshore sediment transport, as not important changes are expected in terms of wave height or wave period. This may be assessed through a fully stochastic simulation, where the natural variability of the climate is included, in order to explore the different sources of uncertainty in the modeling. It is important to stress the limitation of the intra-daily time scale in the model when analyzing the results from the stochastic simulations, unless a solution is successfully introduced in the climate emulator.

Aas, K., Czado, C., Frigessi, A., & Bakkend, H. (2009). Pair-copula constructions of multiple dependence. *Insurance: Mathematics and Economics, 44*, 182-198.

Antolínez, J. A. A., Méndez, F. J., Camus, P., Vitousek, S., González, E. M., Ruggiero, P., & Barnard, P. (2016a). A multiscale climate emulator for long-term morphodynamics (MUSCLE-morpho). *Journal of Geophysical Research: Oceans, 121*, 1-17. doi:10.1002/2015JC011107

Antolínez, J. A. A., Murray, B., Méndez, F. J., Medrano, Y., & Cofiño, A. S. (2016b). *A hybrid downscaling approach for the analysis of coastline response to changing climate forcing in the period 1900-2010*. Paper presented at the Ocean Sciences Conference, Winter Meeting, New Orleans, USA.

Antolínez, J. A. A., Murray, B., Moore, L. J., Wood, J., & Méndez, F. J. (2016c). *A hybrid framework for downscaling time-dependent multivariate coastal boundary conditions*. Paper presented at the AGU Fall Meeting, San Francisco, USA.

Athanassoulis, G. A., & Belibassakis, K. A. (2002). Probabilistic description of metocean parameters by means of kernel density models 1. Theoretical background and first results. *Applied Ocean Research, 24*(1), 1-20. doi:https://doi.org/10.1016/S0141-1187(02)00009-3

Azzalini, A., & Capitanio, A. (2003). Distributions generated by perturbation of symmetry with emphasis on a multivariate skew t-distribution. *Journal of the Royal Statistical Society: Series B (Statistical Methodology), 65*(2), 367-389.

Bedford, T., & Cooke, R. M. (2002). Vines - a new graphical model for dependent random variables. *Annals of Statistics, 30*(4), 1031-1068.

Bermejo, M., & Ancell, R. (2009). Observed changes in extreme temperatures over Spain during 1957–2002 using Weather Types. *Revista de Climatología, 9*, 45-61.

Bosboom, J., & Stive, M. J. F. (2015). *Coastal Dynamics I* (0.5 ed.).

Breymann, W., Dias, A., & Embrechts, P. (2003). Dependence structures for multivariate high-frequency data in finance. *Quantitative Finance, 3*(1), 1-14. doi:http://dx.doi.org/10.1080/713666155

Caires, S., Sterl, A., Bidlot, J.-R., Graham, N., & Swail, V. (2004). Intercomparison of Different Wind-Wave Reanalyses. *Journal of Climate, 17*(10), 1893-1913. doi:10.1175/1520-0442(2004)017<1893:IODWR>2.0.CO;2

Caires, S., Swail, V., & Wang, X. L. (2006). Projection and Analysis of Extreme Wave Climate. *Journal of Climate, 19*, 5581-5605.

Camus, P., Cofiño, A. S., Méndez, F. J., & Medina, R. (2011a). Multivariate wave climate using Self-Organizing Maps. *Journal of Atmospheric and Ocean Technology, 28*, 1554-1568. doi:10.1175/JTECH-D-11-00027.1

Camus, P., Méndez, F. J., Losada, I. J., Menéndez, M., Espejo, A., Pérez, J., Rueda, A., & Guanche, Y. (2014a). A method for finding the optimal predictor indices for local wave climate conditions. *Ocean Dynamics, 64*, 1025-1038. doi:10.1007/s10236-014-0737-2

Camus, P., Méndez, F. J., & Medina, R. (2011b). A hybrid efficient method to downscale wave climate to coastal areas. *Coastal Engineering, 58*, 851-862. doi:10.1016/j.coastaleng.2011.05.007

Camus, P., Méndez, F. J., Medina, R., & Cofiño, A. S. (2011c). Analysis of clustering and selection algorithms for the study of multivariate wave climate. *Coastal Engineering, 58*, 453-462. doi:10.1016/j.coastaleng.2011.02.003

Camus, P., Méndez, F. J., Medina, R., Tomás, A., & Izaguirre, C. (2013). High resolution downscaled ocean waves (DOW) reanalysis in coastal areas. *Coastal Engineering, 72*, 56-68. doi:http://dx.doi.org/10.1016/j.coastaleng.2012.09.002

Camus, P., Menéndez, M., Méndez, F. J., Izaguirre, C., Espejo, A., Cánovas, V., Pérez, J., Rueda, A., Losada, I. J., & Medina, R. (2014b). A weather-type statistical downscaling framework for ocean wave climate. *Journal of Geophysical Research: Oceans, 119*, 1-17. doi:10.1002/2014JC010141

Cánovas, V. (2012). *Análisis estadístico del transporte longitudinal de sedimentos en el corto, medio y largo plazo.* (PhD Thesis), Universidad de Cantabria.

Casas-Prat, M., & Sierra, J. P. (2013). Projected future wave climate in the NW Mediterranean Sea. *Journal of Geophysical Research: Oceans, 118*, 3548-3568. doi:10.1002/jgrc.20233

Casas-Prat, M., Wang, X. L., & Sierra, J. P. (2014). A physical-based statistical method for modeling ocean wave heights. *Ocean Modelling, 73*, 59-75. doi:http://dx.doi.org/10.1016/j.ocemod.2013.10.008

Cavaleri, L., & Sclavo, M. (2006). The calibration of wind and wave model data in the Mediterranean Sea. *Coastal Engineering, 53*, 613-627.

Cazenave, A., & Le Cozannet, G. (2014). Sea level rise and its coastal impacts. *Earth's Future, 2*, 15-34. doi:10.1002/2013EF000188

Collier, M., & Uhe, P. (2012). *CMIP5 datasets from the ACCESS1.0 and ACCESS1.3 coupled climate models*. Retrieved from

Cooke, R. M., Joe, H., & Aas, K. (2011). Vines Arise. In D. Kurowicka & H. Joe (Eds.), *Dependence Modeling - Vine Copula Handbook* (pp. 37-71): World Scientific.

de Winter, R. C., & Ruessink, B. G. (2017). Sensitivity analysis of climate change impacts on dune erosion: case study for the Dutch Holland coast. *Climatic Change, 141*, 685-701. doi:10.1007/s10584-017-1922-3

de Winter, R. C., Sterl, A., de Vries, J. W., Weber, S. L., & Ruessink, B. G. (2012). The effect of climate change on extreme waves in front of the Dutch coast. *Ocean Dynamics, 62*, 1139-1152. doi:10.1007/s10236-012-0551-7

de Winter, R. C., Sterl, A., & Ruessink, B. G. (2013). Wind extremes in the North Sea Basin under climate change: An ensemble study of 12 CMIP5 GCMs. *Journal of Geophysical Research, 118*, 1601-1612. doi:10.1002/jgrd.50147

Dee, D. P., Uppala, S. M., Simmons, A. J., Berrisford, P., Poli, P., Kobayashi, S., Andrae, U., Balmaseda, M. A., Balsamo, G., Bauer, P., Bechtold, P., Beljaars, A. C. M., van de Berg, L., Bidlot, J., Bormann, N., Delsol, C., Dragani, R., Fuentes, M., Geer, A. J., Haimberger, L., Healy, S. B., Hersbach, H., Hólm, E. V., Isaksen, L., Kållberg, P., Köhler, M., Matricardi, M., McNally, A. P., Monge-Sanz, B. M., Morcrette, J.-J., Park, B.-K., Peubey, C., de Rosnay, P., Tavolato, C., Thépaut, J.-N., & Vitart, F. (2011). The ERA-Interim reanalysis: configuration and performance of the data assimilation system. *Quaternaly Journal of the Royal Meteorological Society, 137*, 553-597. doi:10.1002/qj.828

Espejo, A., Camus, P., Losada, I. J., & Méndez, F. J. (2014). Spectral ocean wave climate variability based on atmospheric circulation patterns. *Journal of Physical Oceanography, 44*, 2139-2152. doi:10.1175/JPO-D-13-0276.1

Giardino, A., Santinelli, G., & Bruens, A. (2012). *The state of the coast (Toestand van de kust) Case study: North Holland* (1206171-003). Retrieved from

Giorgi, F., Hewitson, B., Christensen, J., Hulme, M., von Storch, H., Whetton, P., Jones, R., Mearns, L. O., & Fu, C. (2001). Regional climate information-Evaluation and projections. In J. T. H. e. al. (Ed.), *Climate Change 2001. The Scientific Basis. Contribution of Working Group to the Third Assessment Report of the IPCC: Contribution to Working Group I* (First Edition ed., pp. 583-638). Cambridge, United Kingdom and New York: Cambridge University Press.

Guanche, Y., Mínguez, R., & Méndez, F. J. (2014). Autoregressive logistic regression applied to atmospheric circulation patterns. *Climate Dynamics, 42*(1-2), 537-552. doi:DOI 10.1007/s00382-013-1690-3

Gulev, S. K., & Grigorieva, V. (2006). Variability of the winter wind waves and swell in the North Atlantic and North Pacific as revealed by the voluntary observing ship data. *Journal of Climate, 19*, 5667-5685.

Haarsma, R. J., Hazeleger, W., C., S., de Vries, H., Sterl, A., Bintanja, R., van Oldenborgh, G. J., & van den Brink, H. W. (2013). More hurricanes to hit western Europe due to global warming. *Geophysical Research Letters, 40*, 1783–1788. doi:10.1002/grl.50360

Haas, C. N. (1999). On modeling correlated random variables in risk assessment. *Risk Analysis, 19*(6), 1205-1214. doi:10.1023/A:1007047014741

Hegermiller, C., Antolínez, J. A. A., Rueda, A., Camus, P., Pérez, J., Erikson, L. H., Barnard, P., & Méndez, F. J. (2017). A multimodal wave spectrum–based approach for statistical downscaling of local wave climate. *Journal of Physical Oceanography, 47*, 375-386. doi:10.1175/JPO-D-16-0191.1

Holthuijsen, L. H. (2007). *Waves in oceanic and coastal waters*: Cambridge University Press.

Huth, R. (2000). A circulation classification scheme applicable in GCM studies. *Theoretical and Applied Climatology, 67*(1), 1-18. doi:10.1007/s007040070012

IPCC-DDC. (2013). What is a GCM? Retrieved from http://www.ipcc-data.org/guidelines/pages/gcm_guide.html

IPCC. (2013). *Climate Change 2013: The Physical Science Basis. Contribution of Working Group I to the Fifth Assessment Report of the Intergovernmental Panel on Climate Change* (T. F. Stocker, D. Qin, G.-K. Plattner, M. Tignor, S. K. Allen, J. Boschung, A. Nauels, Y. Xia, V. Bex, & P. M. Midgley Eds.). Cambridge, United Kingdom and New York, NY, USA: Cambridge University Press.

Jäger, W. S., & Morales Nápoles, O. (2017). A Vine-Copula model for time series of significant wave heights and mean zero-crossing periods in the North Sea. *Journal of Risk and Uncertainty in Engineering Systems, Part A: Civil Engineering, Accepted*.

Kalnay, E., Kanamitsu, M., Kistler, R., Collins, W., Deaven, D., Gandin, L., Iredell, M., Saha, S., White, G., Woollen, J., Zhu, Y., Leetmaa, A., & Reynolds, R. (1996). The NCEP/NCAR 40-Year Reanalysis Project. *Bulletin of the American Meteorological Society, 77*(3), 437-471. doi: http://dx.doi.org/10.1175/1520-0477(1996)077<0437:TNYRP>2.0.CO;2

Katsman, C. A., Sterl, A., Beersma, J. J., van den Brink, H. W., Church, J. A., Hazeleger, W., Kopp, R. E., Kroon, D., Kwadijk, J., Lammersen, R., Lowe, J., Oppenheimer, M., Plag, H.-P., Ridley, J., von Storch , H., Vaughan, D. G., Vellinga, P., Vermeersen, L. L. A., van de Wal, R. S. W., & Weisse, R. (2011). Exploring high-end scenarios for local sea level rise to develop flood protection strategies for a low-lying delta - the Netherlands as an example. *Climatic Change, 109*, 617-645. doi:10.1007/s10584-011-0037-5

Kurowicka, D. (2011). Introduction: Dependence Modeling. In D. Kurowicka & H. Joe (Eds.), *Dependence Modeling - Vine Copula Handbook* (pp. 1-17): World Scientific.

Kurowicka, D., & Cooke, R. M. (2006). *Uncertainty analysis with high dimensional dependence modelling* (J. W. Sons Ed.).

Kurowicka, D., & Joe, H. (2011). *Dependence Modeling - Vine Copula Handbook*: World Scientific.

Laugel, A., Menéndez, M., Benoit, M., Mattarolo, G., & Méndez, F. J. (2014). Wave climate projections along the French coastline: Dynamical versus statistical downscaling methods. *Ocean Modelling, 84*, 35-50. doi:http://dx.doi.org/10.1016/j.ocemod.2014.09.002

Leontaris, G., Morales Nápoles, O., & Wolfert, A. R. M. (2016). Probabilistic scheduling of offshore operations using copula based environmental time series – An application for cable installation management for offshore wind farms. *Ocean Engineering, 125*, 328-341. doi:https://doi.org/10.1016/j.oceaneng.2016.08.029

Mínguez, R., Espejo, A., Tomás, A., Méndez, F. J., & Losada, I. J. (2011). Directional calibration of wave reanalysis databases using instrumental data. *Journal of Atmospheric and Ocean Technology, 28*, 1466-1485. doi:10.1175/JTECH-D-11-00008.1

Morales Nápoles, O. (2011). Counting Vines. In D. Kurowicka & H. Joe (Eds.), *Dependence Modeling - Vine Copula Handbook* (pp. 189-218): World Scientific.

Mulder, J. P. M., Hommes, S., & Horstman, E. M. (2011). Implementation of coastal erosion management in the Netherlands. *Ocean & Coastal Management, 54*, 888-897.

Nelsen, R. B. (2006). *An Introduction to Copulas* (Second ed.): Springer Science & Business Media.

NOAA. (2008). Teleconnection Introduction. Retrieved from http://www.cpc.ncep.noaa.gov/data/teledoc/teleintro.shtml

Pérez, J., Méndez, F. J., Menéndez, M., & Losada, I. J. (2014a). ESTELA: A method for evaluating the source and travel time of the wave energy reaching a local area. *Ocean Dynamics, 64*(8), 1181-1191. doi:DOI 10.1007/s10236-014-0740-7

Pérez, J., Menéndez, M., Camus, P., Méndez, F. J., & Losada, I. J. (2015). Statistical multi-model climate projections of surface ocean waves in Europe. *Ocean Modelling, 96*, 161-170. doi:http://dx.doi.org/10.1016/j.ocemod.2015.06.001

Pérez, J., Menéndez, M., Méndez, F. J., & Losada, I. J. (2014b). Evaluating the performance of CMIP3 and CMIP5 global climate models over the Northeast Atlantic region. *Climate Dynamics, 43*(9-10), 2663-2680. doi:10.1007/s00382-014-2078-8

Rascle, N., & Ardhuin, F. (2013). A global wave parameter database for geophysical applications. Part 2: Model validation with improved source term parameterization. *Ocean Modelling, 70*, 174-188. doi:http://dx.doi.org/10.1016/j.ocemod.2012.12.001

Reguero, B. G., Menéndez, M., Méndez, F. J., Mínguez, R., & Losada, I. J. (2012). A Global Ocean Wave (GOW) calibrated reanalysis from 1948 onwards. *Coastal Engineering, 65*, 38-55. doi:10.1016/j.coastaleng.2012.03.003

Rueda, A., Camus, P., Méndez, F. J., Tomás, A., & Luceño, A. (2016a). An extreme value model for maximum wave heights based on weather types. *Journal of Geophysical Research: Oceans, 121*, 1-12. doi:10.1002/2015JC010952

Rueda, A., Camus, P., Tomás, A., Vitousek, S., & Méndez, F. J. (2016b). A multivariate extreme wave and storm surge climate emulator based on weather patterns. *Ocean Modelling, 104*, 242-251. doi:http://dx.doi.org/10.1016/j.ocemod.2016.06.008

Rueda, A., Gouldby, B., Méndez, F. J., Tomás, A., Losada, I. J., Lara, J. L., & Díaz-Simal, P. (2016c). The use of wave propagation and reduced complexity inundation models and metamodels for coastal flood risk assessment. *Journal of Flood Risk Management, 9*(4), 390-401. doi:10.1111/jfr3.12204

Rueda, A., Hegermiller, C., Antolínez, J. A. A., Camus, P., Vitousek, S., Ruggiero, P., Barnard, P., Erikson, L. H., Tomás, A., & Méndez, F. J. (2017). Multiscale Climate Emulator of Multimodal Wave Spectra: MUSCLE-Spectra. *Journal of Geophysical Research: Oceans, Accepted*. doi:10.1002/2016JC011957

Ruessink, B. G., Kuriyama, Y., Reniers, A. J. H. M., Roelvink, J. A., & Walstra, D. J. R. (2007). Modeling cross-shore sandbar behavior on the timescale of weeks. *Journal of Geophysical Research, 112*(F03010), 1-15. doi:doi:10.1029/2006JF000730

Saha, S., Moorthi, S., Pan, H.-L., Wu, X., Wang, J., Nadiga, S., Tripp, P., Kistler, R., Woollen, J., Behringer, D., Liu, H., Stokes, D., Grumbine, R., Gayno, G., Wang, J., Hou, Y.-T., Chuang, H.-y., Juang, H.-M. H., Sela, J., Iredell, M., Treadon, R., Kleist, D., van Delst, P., Keyser, D., Derber, J., Ek, M., Meng, J., Wei, H., Yang, R., Lord, S., van den Dool, H., Kumar, A., Wang, W., Long, C., Chelliah, M., Xue, Y., Huang, B., Schemm, J.-K., Ebisuzaki, W., Lin, R., Xie, P., Chen, M., Zhou, S., Higgins, W., Zou, C.-Z., Liu, Q., Chen, Y., Han, Y., Cucurull, L., Reynolds, R. W., Rutledge, G., & Goldberg, M. (2010). The NCEP Climate Forecast System Reanalysis. *Bulletin of the American Meteorological Society, 91*(8), 1015-1057. doi:10.1175/2010BAMS3001.1

Saha, S., Moorthi, S., Wu, X., Wang, J., Nadiga, S., Tripp, P., Behringer, D., Hou, Y.-T., Chuang, H.-Y., Iredell, M., Ek, M., Meng, J., Yang, R., Mendez, M. P., van den Dool, H., Zhang, Q., Wang, W., Chen, M., & Becker, E. (2014). The NCEP Climate Forecast System Version 2. *Journal of Climate, 27*(6), 2185–2208. doi:10.1175/JCLI-D-12-00823.1

Schölzel, C., & Friederichs, P. (2008). Multivariate non-normally distributed random variables in climate research - Introduction to the copula approach. *Nonlinear Processes in Geophysics, 15*, 761-772. doi:10.5194/npg-15-761-2008

Solari, S., & Losada, I. J. (2012). A unified statistical model for hydrological variables including the selection of threshold for the peak over threshold method. *Water Resources Research, 48*(10), 1-15. doi:10.1029/2011WR011475

Sterl, A., van den Brink, H., de Vries, H., Haarsma, R. J., & van Meijgaard, E. (2009). An ensemble study of extreme storm surge related water levels in the North Sea in a changing climate. *Ocean Science, 5*, 369-378.

Taylor, K. E., Stouffer, R. J., & Meehl, G. A. (2012). An Overview of CMIP5 and the Experiment Design. *Bulletin of the American Meteorological Society, 93*(4), 499–515. doi:http://dx.doi.org/10.1175/BAMS-D-11-00094.1

Uppala, S. M., KÅllberg, P. W., Simmons, A. J., Andrae, U., Bechtold, V. D. C., Fiorino, M., Gibson, J. K., Haseler, J., Hernandez, A., Kelly, G. A., Li, X., Onogi, K., Saarinen, S., Sokka, N., Allan, R. P., Andersson, E., Arpe, K., Balmaseda, M. A., Beljaars, A. C. M., Berg, L. V. D., Bidlot, J., Bormann, N., Caires, S., Chevallier, F., Dethof, A., Dragosavac, M., Fisher, M., Fuentes, M., Hagemann, S., Hólm, E., Hoskins, B. J., Isaksen, L., Janssen, P. A. E. M., Jenne, R., Mcnally, A. P., Mahfouf, J.-F., Morcrette, J.-J., Rayner, N. A., Saunders, R. W., Simon, P., Sterl, A., Trenberth, K. E., Untch, A., Vasiljevic, D., Viterbo, P., & Woollen, J. (2005). The ERA-40 re-analysis. *Quaternaly Journal of the Royal Meteorological Society, 131*, 2961–3012. doi:10.1256/qj.04.176

van Rijn, L. C. (1997). Sediment transport and budget of the central coastal zone of Holland. *Coastal Engineering, 32*, 61-90.

van Vuuren, D. P., Edmonds, J., Kainuma, M., Riahi, K., Thomson, A., Hibbard, K., Hurtt, G. C., Kram, T., Krey, V., Lamarque, J.-F., Masui, T., Meinshausen, M., Nebojsa Nakicenovic, N., Smith, S. J., & Rose, S. K. (2011). The representative concentration pathways: an overview. *Climate Change, 109*, 5-31. doi:10.1007/s10584-011-0148-z

Walstra, D. J. R., Hoekstra, R., Tonnon, P. K., & Ruessink, B. G. (2013). Input reduction for long-term morphodynamic simulations in wave-dominated coastal settings. *Coastal Engineering, 77*, 57-70. doi:http://dx.doi.org/10.1016/j.coastaleng.2013.02.001

Walstra, D. J. R., Reniers, A. J. H. M., Ranasinghe, R., Roelvink, J. A., & Ruessink, B. G. (2012). On bar growth and decay during interannual net offshore migration. *Coastal Engineering, 60*, 190-200. doi:10.1016/j.coastaleng.2011.10.002

Walstra, D. J. R., Ruessink, B. G., Reniers, A. J. H. M., & Ranasinghe, R. (2015). Process-based modeling of kilometer-scale alongshore sandbar variability. *Earth Surface Processes and Landforms, 40*, 995-1005. doi:10.1002/esp.3676

Wang, X. L., Feng, Y., & Swail, V. (2012). North Atlantic wave height trends as reconstructed from the 20th century reanalysis. *Geophysical Research Letters, 39*, L18705. doi:10.1029/2012GL053381

Wang, X. L., Feng, Y., & Swail, V. (2014). Changes in global ocean wave heights as projected using multimodel CMIP5 simulations. *Geophysical Research Letters, 41*, 1026–1034. doi:10.1002/2013GL058650

Wang, X. L., Swail, V., & Cox, A. (2010). Dynamical versus statistical downscaling methods for ocean wave heights. *International Journal of Climatology, 30*, 317-332. doi:10.1002/joc.1899

Wilby, R. L., Charles, S. P., Zorita, E., Timbal, B., Whetton, P., & Mearns, L. O. (2004). *Guidelines for use of Climate Scenarios developed from Statistical Downscaling methods*. Retrieved from http://www.ipcc-data.org/guidelines/dgm_no2_v1_09_2004.pdf

Yoshiba, T. (2015). Maximum likelihood estimation of skew-t copulas with its applications to stock returns. *The Institute of Statistical Mathematics Research Memorandum, 1195*.

Appendix A: Principal Component Analysis

PCA, described in §2.1.3, is a statistical technique that allows to reduce the dimensionality of the data retaining a high percentage of the variance. In this case, the first 52 Empirical Orthogonal Functions (EOFs) (from a total of 4 380) and their corresponding Principal Components (PCs) explain the 95% of the variance. The first 4 EOFs are shown in Figure A-1.

A multivariate linear regression between the 52 PCs of the predictor and the predictand is applied as a preliminary test of the skill of the predictor. For this quick assessment, two parameters representing the predictand are chosen: the daily mean overall significant wave height and the cubic root of the daily mean bulk energy flux. The cubic root is considered here to smooth the peaks which are usually observed in this variable.
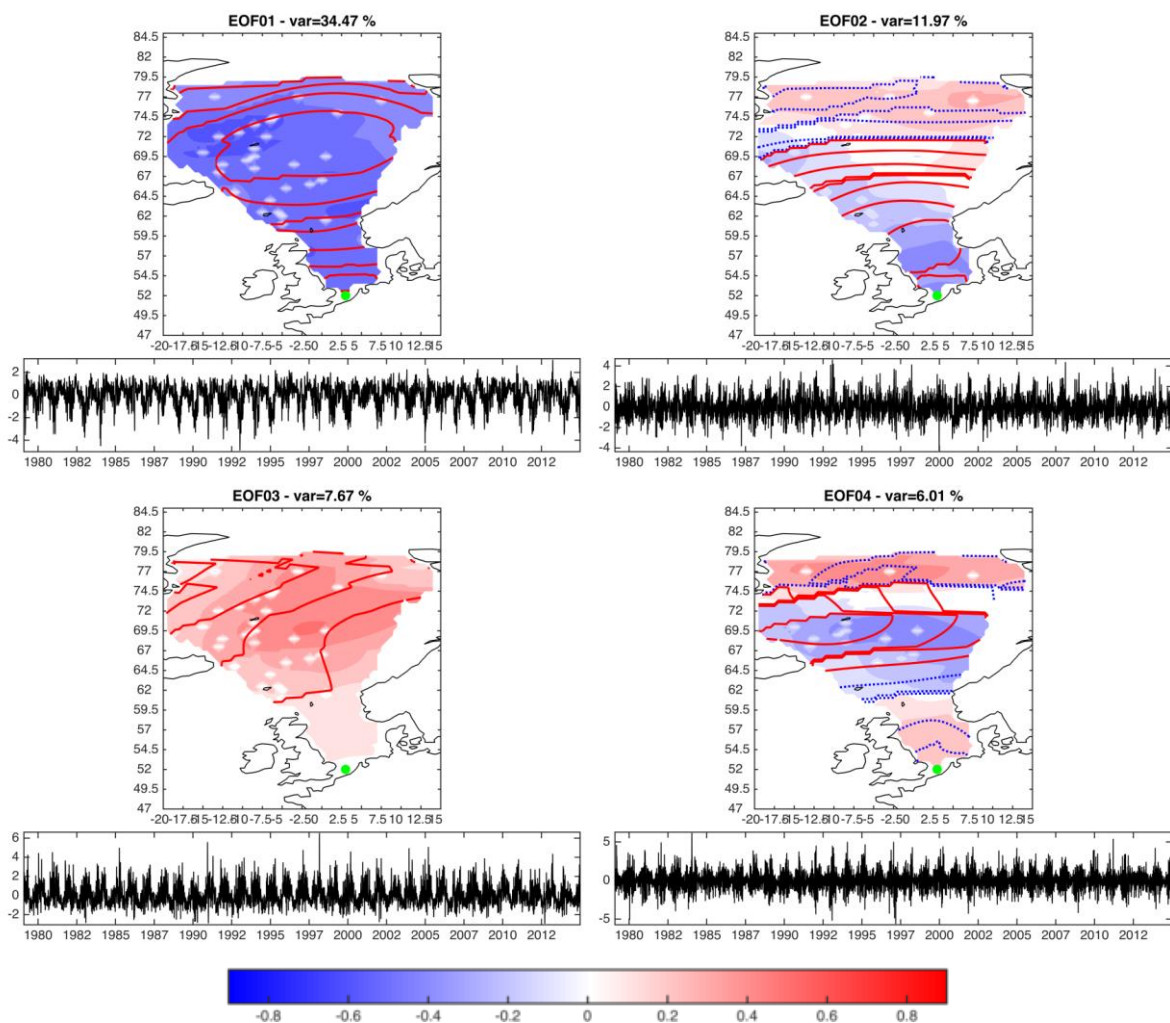
Figure A-1: First 4 EOFs and PCs of the predictor. SLP anomalies are represented by contour lines and squared SLP gradients anomalies are represented by the colored areas.

The energy flux is defined as:

$$EF = \frac{\rho g^2}{64\pi} T_p H_s^2 \qquad\qquad (A\text{-}1)$$

Where ρ is the water density, g is the acceleration of gravity [m/s^2], T_p denotes the peak period [s] and H_s denotes the significant wave height [m].

For the sake of simplicity, constants are dropped in the calculation. The available time series of PCs are divided into calibration (1993-2006) and validation period (2006-2012) in order to fit the multivariate linear regression. Results are shown in the following figures, where a good match between the selected PCs and the overal significant wave height and the cubic root of the bulk energy flux is observed. In both cases, correlation coefficients are close to unity.

Three different estimations of the errors are given in the figures: Root Mean Square (RMS), Scatter Index (SI) and BIAS. In both cases, these values are small thus confirming that the predictor is able to explain the predictand at daily scale.
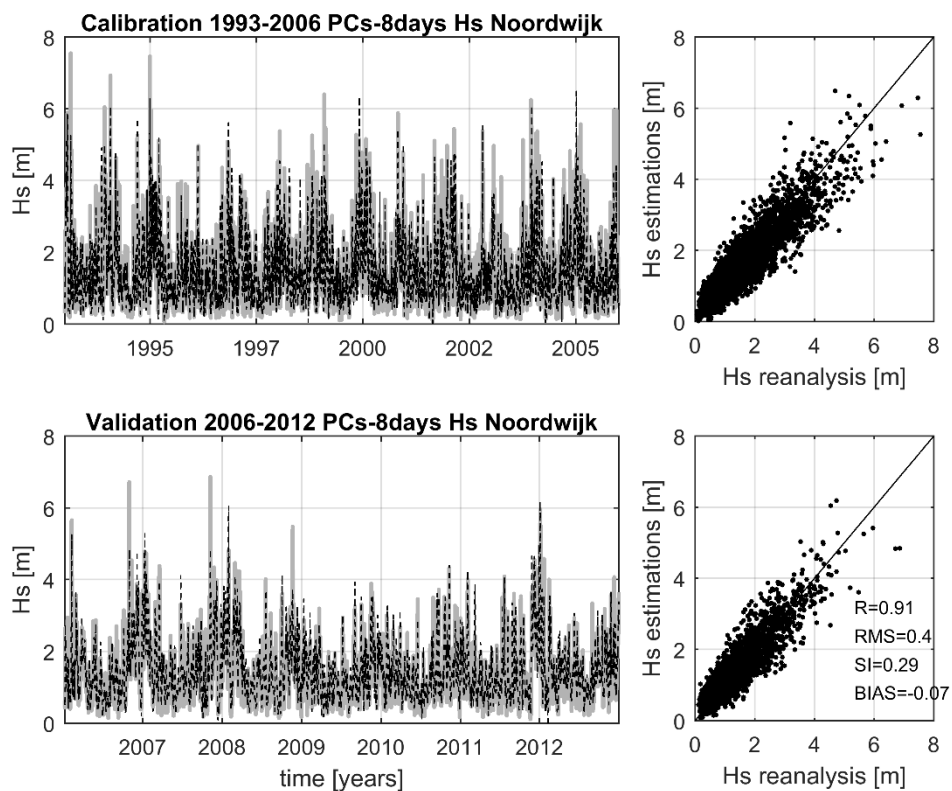
Figure A-2: Multivariate regression model of the daily mean H_s at Noordwijk. Observed values in gray thick line and estimations in dashed black line. Upper panel: calibration period. Lower panel: validation period.
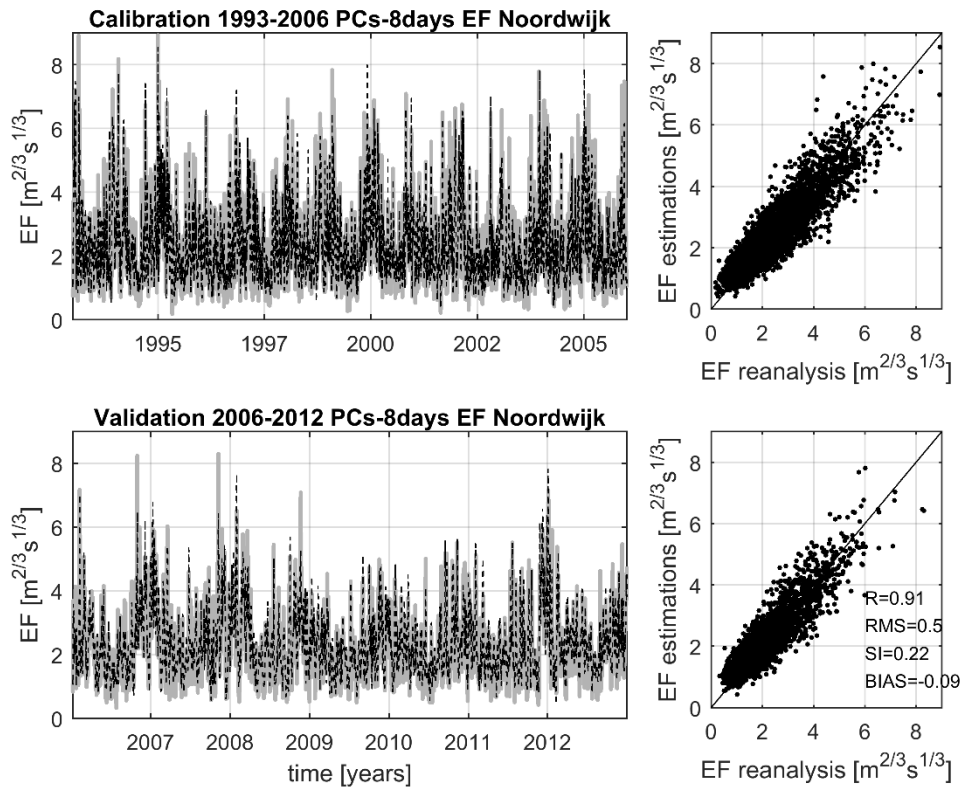
Figure A-3: Multivariate regression model of the cubic root of the daily mean energy flux at Noordwijk. Observed values in gray thick line and estimations in dashed black line. Upper panel: calibration period. Lower panel: validation period.

Appendix B: Number of weather types

The number of WTs is selected aiming to ease the implementation, fitting and interpretation of the model results. In order to explore the influence of the number of WTs in the classification and the relation with the predictand, the monthly mean bulk energy flux time series is computed as the sum of the mean bulk energy flux for each WT weighted by the occurrence probability of each WT.

Firstly, the mean bulk energy flux for each WT is calculated as follows:

$$\overline{EF_i} = \frac{1}{N_i} \sum_t EF(t) \mid WT_i \tag{B-1}$$

Where $\overline{EF_i}$ is the mean bulk energy flux of WT i [m²/s], $i = 1, \dots, N_{WT}$; N_{WT} is the number of WTs, N_i denotes the number of observations during WT i and $EF(t) \mid WT_i$ represents the observations of energy flux during WT i [m²/s].

Then, the monthly mean bulk energy flux is computed as:

$$\overline{EF_{j,y}} = \sum_i p_{i,j,y} \, \overline{EF_i} \tag{B-2}$$

Where $\overline{EF_{j,y}}$ is the monthly mean bulk energy flux of month j, year y [m²/s] and $p_{i,j,y}$ is the occurrence probability of WT i in month j, year y.

The comparison between the computed bulk energy flux and the monthly mean values from the observed time series is shown in Figure B-1. The same calculation was undertaken varying the number of WTs between 25 up to 144, where square number are chosen to ease the visualization of the WTs in a lattice. Energy flux values are normalized by $64\pi/\rho g^2$.

For each time series, the correlation coefficient and 3 different errors are given at the right side. It can be seen that the correlation coefficient increases while increasing the number of WTs, while the errors slightly decrease. This is happening because the larger the number of WTs, the larger the amount of elements in the WT set, adding more terms to explain the same variable. This can be interpreted as a mathematical fact without any physical added value. Furthermore, there is no important difference between the estimated time series after visual inspection. Finally, the chosen number of 49 WTs is confirmed.
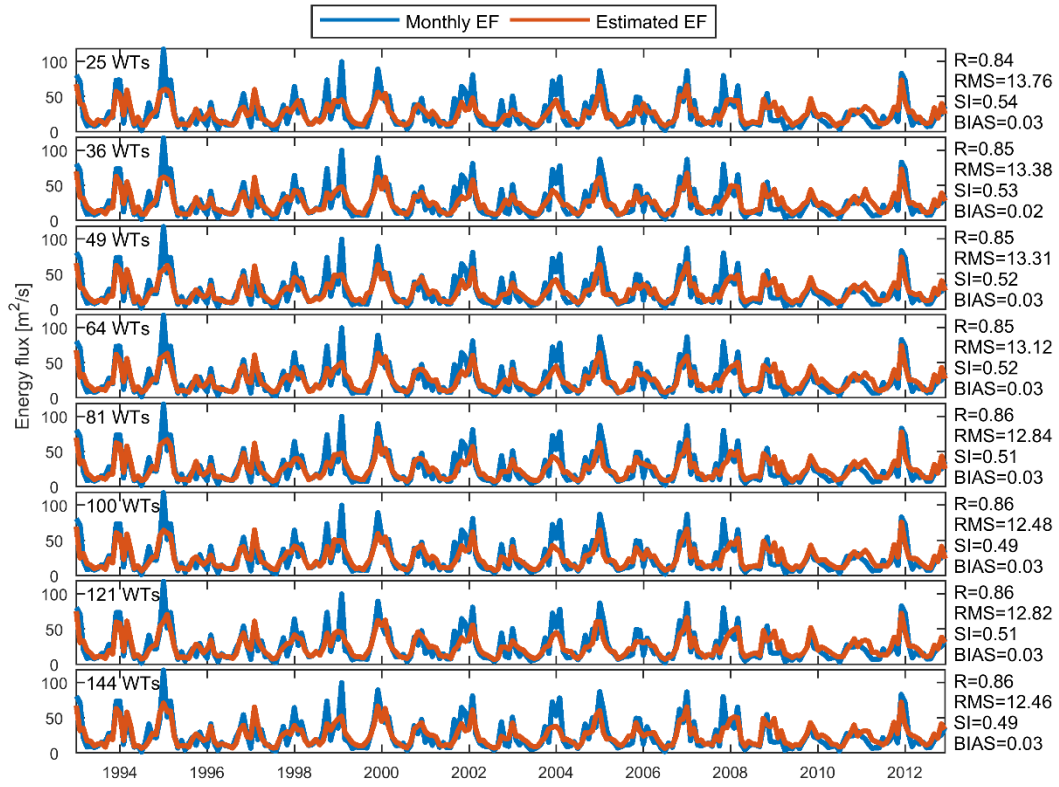
Figure B-1: Monthly mean bulk energy flux for different number of WTs.

Appendix C: Fitting marginal distributions

C.1. Marginal distributions for H_s

For each weather type, different theoretical distributions are fitted to the empirical distributions of H_s and T_p for the sea and swell components. In the case of the significant wave height, 4 distributions are considered:

- Weibull
- Kernel density function
- Mixed model of kernel density function and Generalized Pareto Distributions for the lower and upper tail with a threshold of 0.1 and 0.9, respectively.
- Mixed model of kernel density function and Generalized Pareto Distributions for the lower and upper tail with a threshold of 0.05 and 0.95, respectively.

The fitting of the mentioned distributions to the empirical data is shown in Figure C-1 for the sea component and in Figure C-2 for the swell. The figures correspond to Weibull probability plots, where the vertical axis indicates the cumulative probability, the blue dots correspond to the empirical cumulative probability and the lines depict the fitted distributions.

It can be seen that central regime is well represented by the 4 fitted distributions, but important differences are observed in the upper tail, where the generalized Pareto distribution seems to give a better fitting than the other distributions. In some weather types, the kernel density function provides a sound fitting to the data, but in most of the cases it tends to overestimate the values for the significant wave height. Something similar happens with the weibull distribution, which has little flexibility to represent the upper tail, under or overestimating depending on the WT.

Based on these results, the mixed model with thresholds 0.1-0.9 has been adopted for the representation of the marginal distributions of H_s for both sea and swell components.

C.2. Marginal distributions for T_p

For this variable, several distributions are considered as candidates:

- Weibull
- Generized Extreme Value (GEV), with no restriction on the shape parameter
- Gumbel
- Kernel density function
- Mixed model of kernel density function and Generalized Pareto Distributions for the lower and upper tail with a threshold of 0.1 and 0.9, respectively.
- Mixed model of kernel density function and Generalized Pareto Distributions for the lower and upper tail with a threshold of 0.05 and 0.95, respectively.

The fitting of the these distributions to the empirical data is shown in Figure C-3 and Figure C-4 for the sea and swell component, respectively. In this case, the figures correspond to Gumbel probability plots, where the vertical axis indicates the cumulative probability, the blue dots correspond to the empirical cumulative probability and the lines depict the fitted distributions.

Once again, it can be seen that central regime is well represented by all the fitted distributions, but important differences are observed in the upper tail, where the mixed model seems to give a better fitting than the other distributions. For instance, the Weibull distribution tends to underestimate the

extreme values, while the Gumbel distribution overestimate them. The GEV distribution and the kernel density function show some more flexibility, but still give an under or overestimation (depending on the WT) of the values in the upper tail.
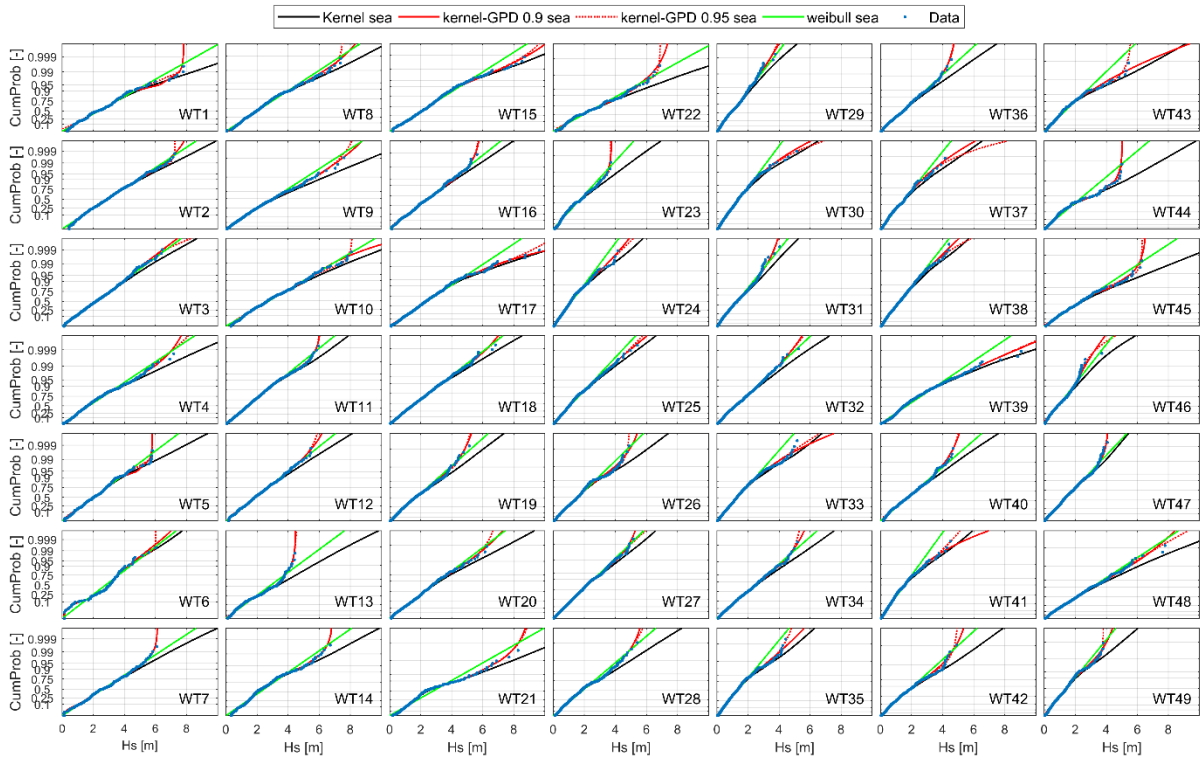

Figure C-1: Weibull probability plots of the empirical and fitted marginal distributions of $H_{S_{sea}}$ associated to each WT.
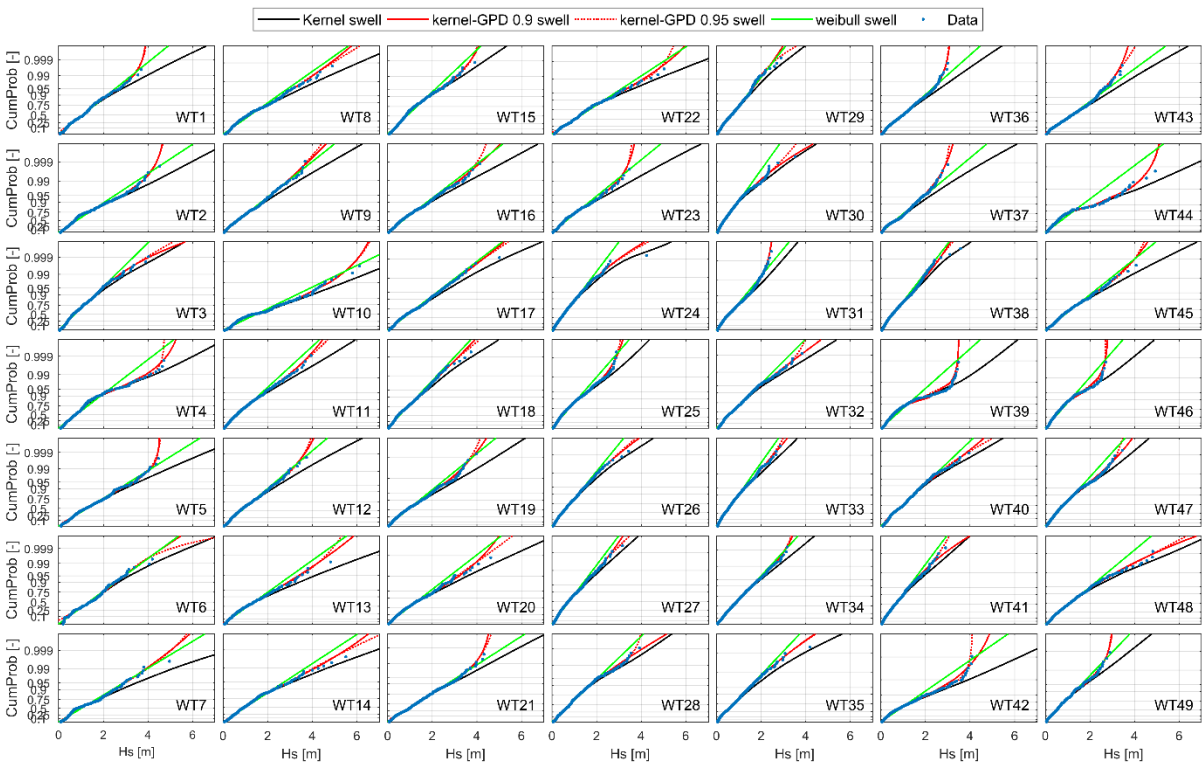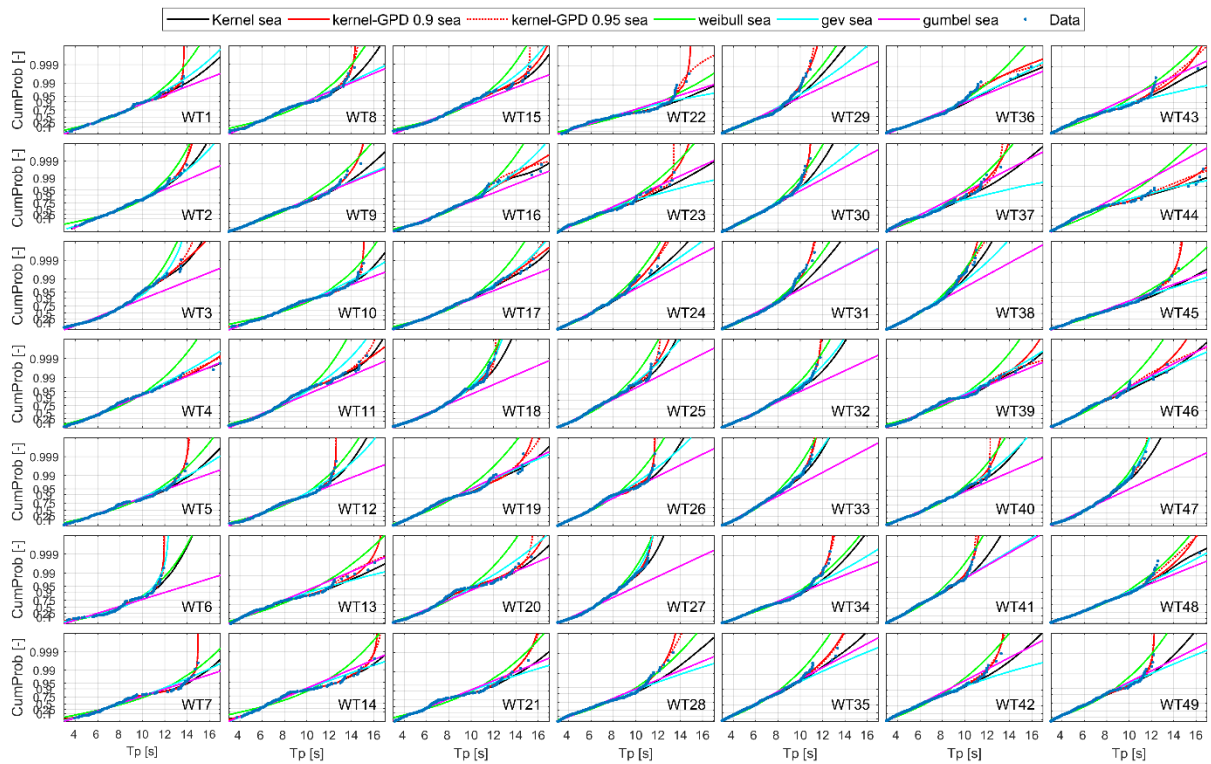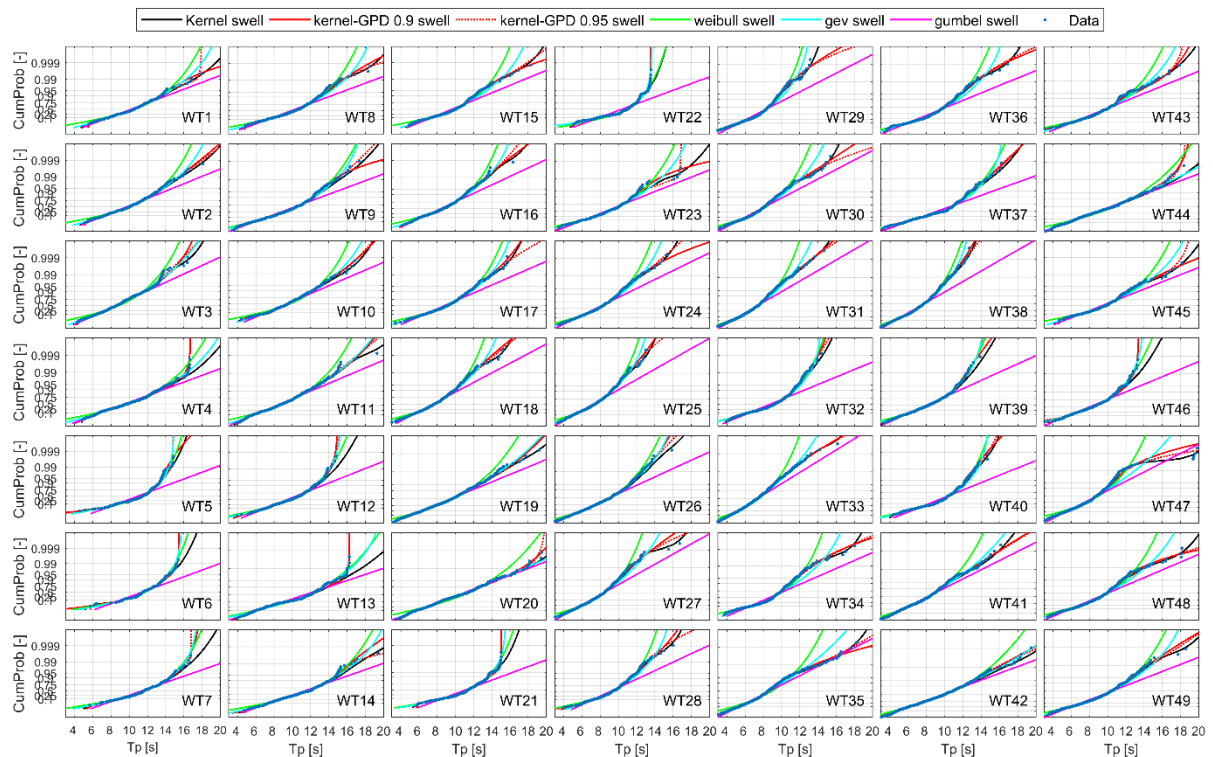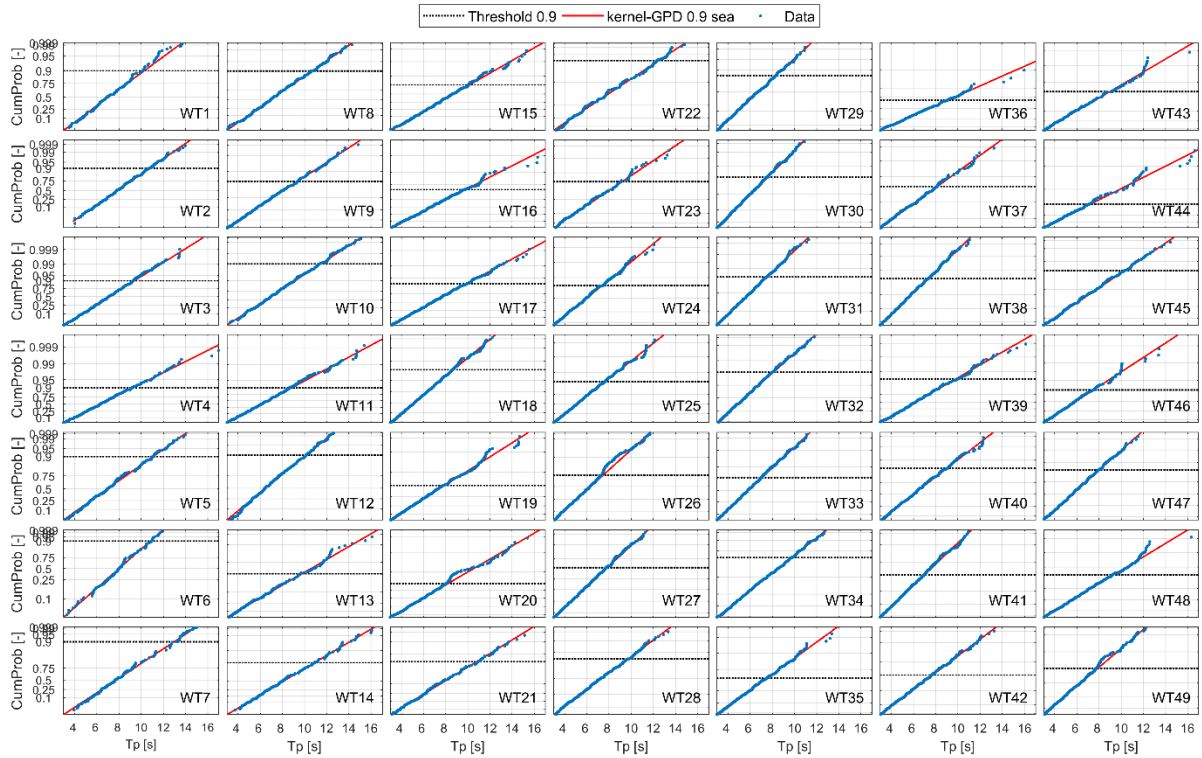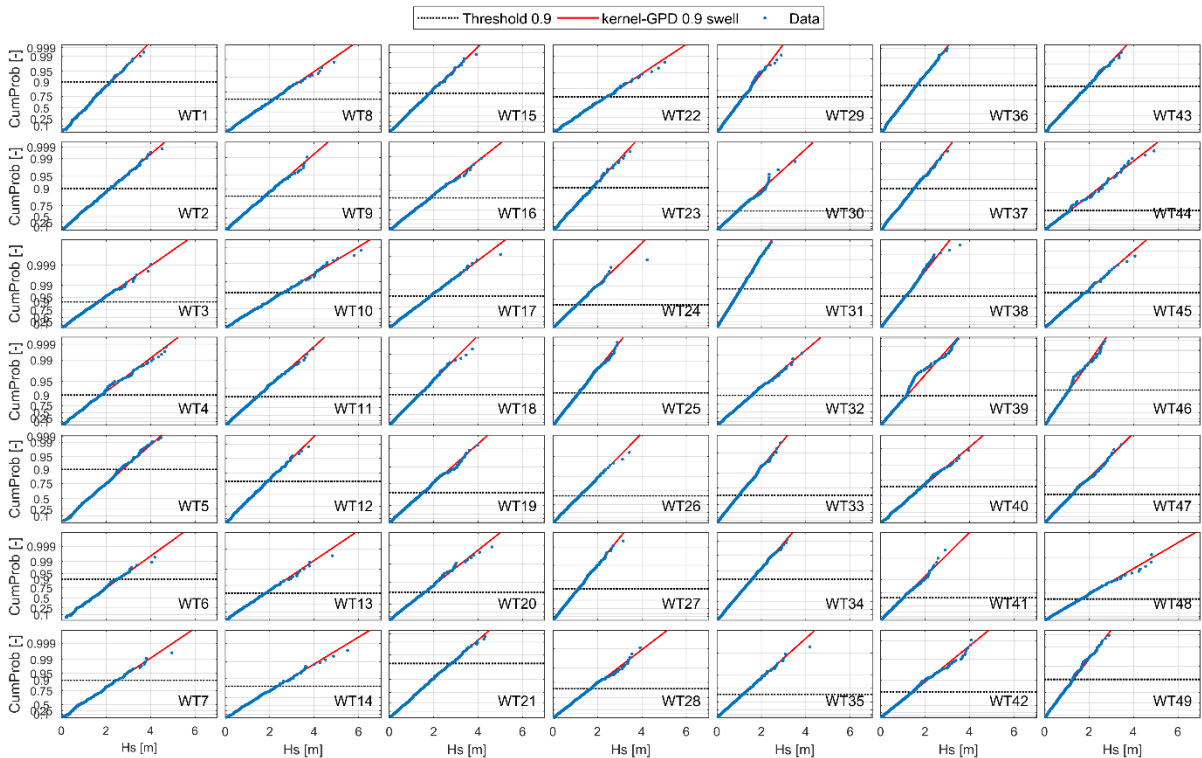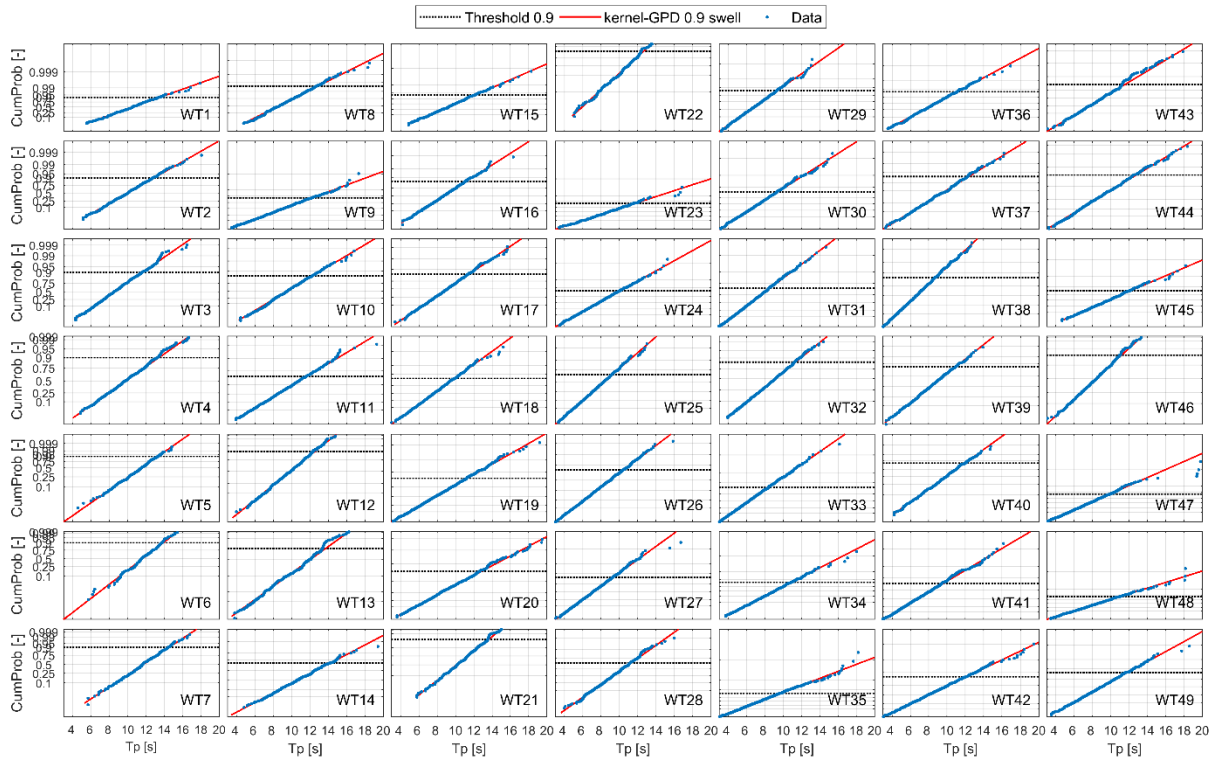

Figure C-2: Weibull probability plots of the empirical and fitted marginal distributions of $H_{S_{swell}}$ associated to each WT.

Based on these results, the same has been concluded: the mixed model with thresholds 0.1-0.9 has been adopted for the representation of the marginal distributions of T_p for both sea and swell components.

Figure C-3: Gumbel probability plots of the empirical and fitted marginal distributions of $T_{p_{sea}}$ associated to each WT.

Figure C-4: Gumbel probability plots of the empirical and fitted marginal distributions of $T_{p_{swell}}$ associated to each WT.

C.3. Fitted marginal distributions

The fitting of the mixed model to the empirical data is shown in the following figures for $T_{p_{sea}}$, $H_{s_{swell}}$ and $T_{p_{swell}}$, respectively.

Figure C-5: Probability plots of the empirical and fitted marginal distributions of $T_{p_{sea}}$ associated to each WT.

Figure C-6: Probability plots of the empirical and fitted marginal distributions of $H_{s_{swell}}$ associated to each WT.

Figure C-7: Probability plots of the empirical and fitted marginal distributions of $T_{p_{swell}}$ associated to each WT.

Appendix D: Rank correlations for unimodal sea states

Spearman's rank correlations between observed variables for the unimodal cases are shown in Figure D-1 for sea and Figure D-2 for swell component. In the figures, positive and negative rank correlations are depicted in cyan and magenta lines, respectively.

As expected, strong positive correlation is observed between $H_{s_{sea}}$ and $T_{p_{sea}}$ in all the weather types for the sea component. The correlation between $H_{s_{swell}}$ and $T_{p_{swell}}$ is much weaker. In general, the figures reveal the interdependence between the variables, emphasizing the importance of considering the dependence structure in the statistical model.

Although each weather type has its own particular pattern, some similarities can be identified. For instance, negative correlations only appear at the right side of the lattice for the sea component. On the other hand, looking at the swell component, correlation between H_s and Dir is always negative at the left side of the lattice, changing to positive values in some WTs located at the right side of the lattice.
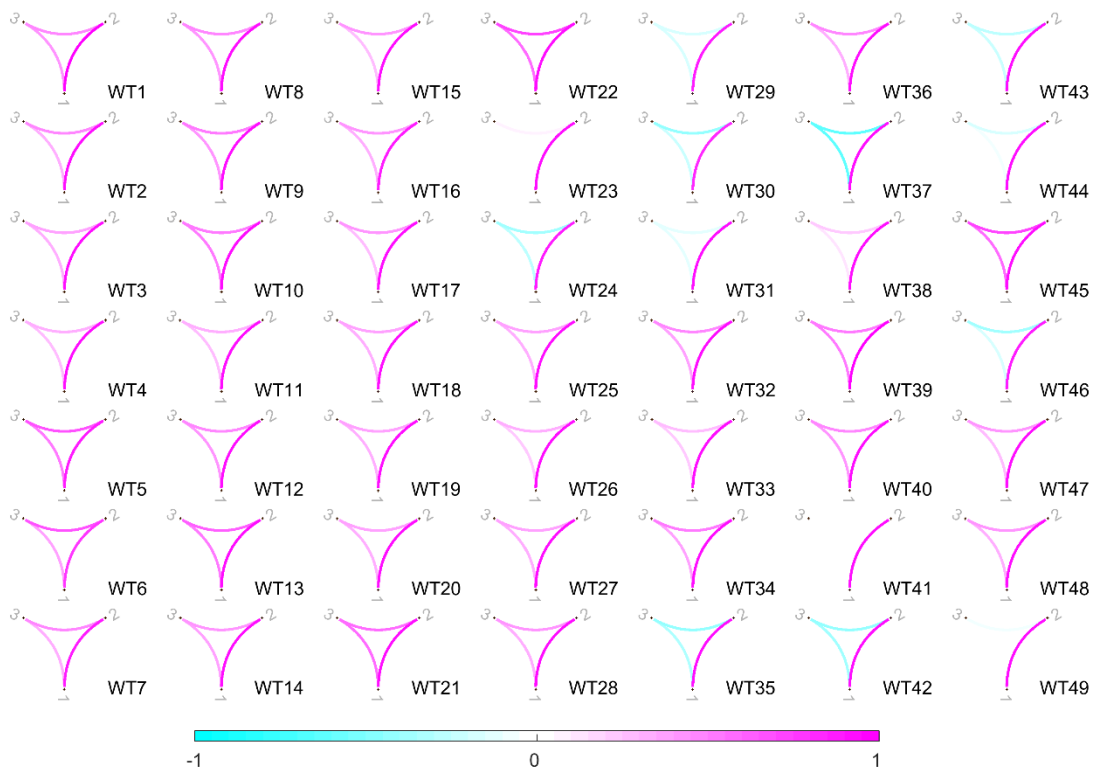
Figure D-1: Graphical representation of rank correlation coefficients for the sea component associated to each WT. Numbers from 1 to 3 stand for $H_{s_{sea}}, T_{p_{sea}}, Dir_{sea}$ respectively. Color scale is defined between -1 (cyan) for negative correlation, 0 (white) for no correlation and 1 (magenta) for positive correlation.
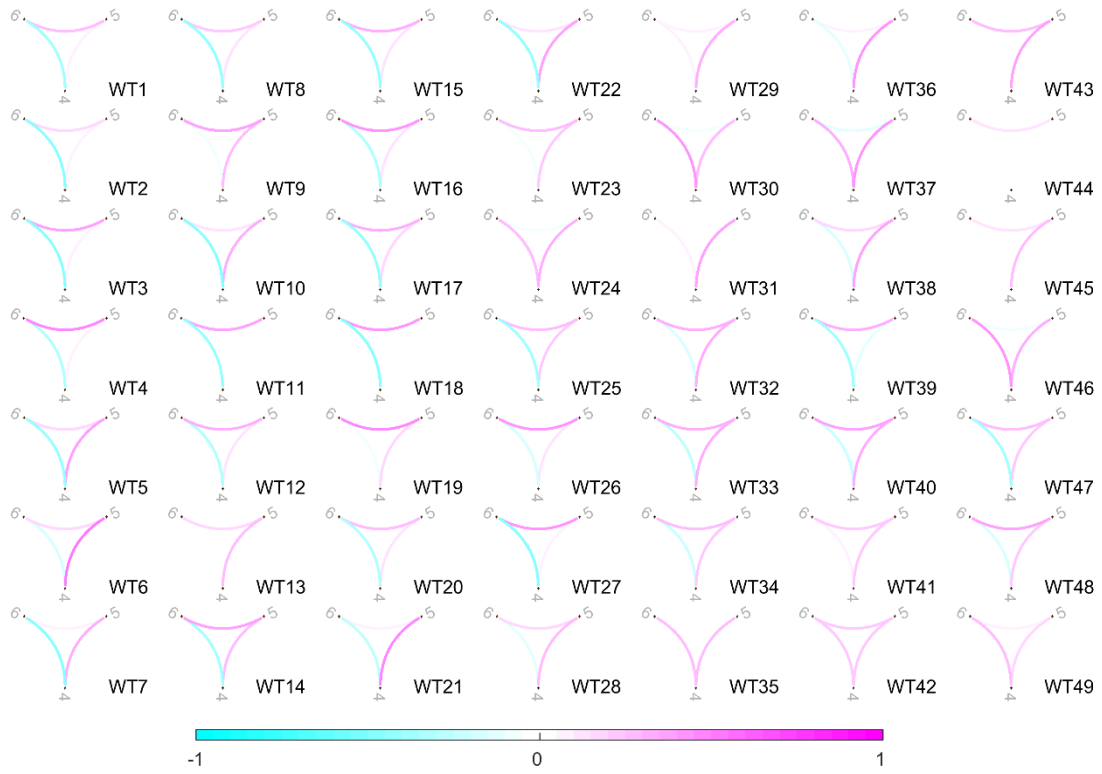
Figure D-2: Graphical representation of rank correlation coefficients for the swell component associated to each WT. Numbers from 4 to 6 stand for $H_{s_{swell}}, T_{p_{swell}}, Dir_{swell}$ respectively. Color scale is defined between -1 (cyan) for negative correlation, 0 (white) for no correlation and 1 (magenta) for positive correlation.

For the sake of simplicity, the sampling algorithm of a D-vine on 6 variables is illustrated using the schematization of the following figure.
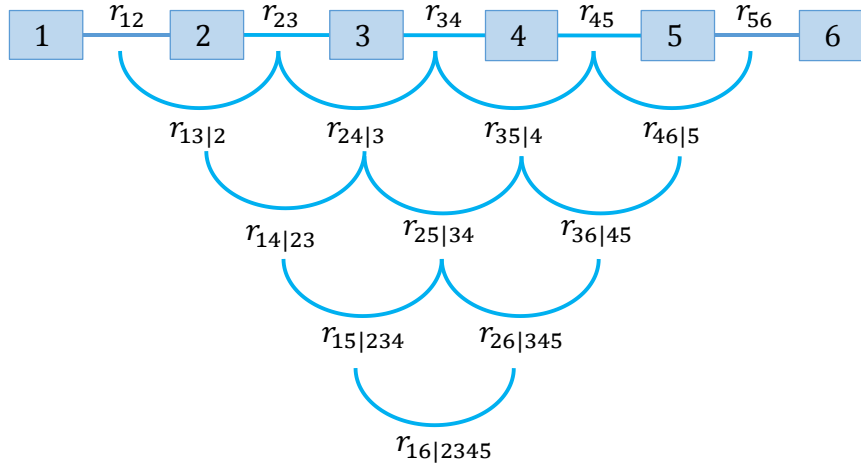

Figure E-1: D-vine on 6 variables with (conditional) rank correlations.

Let $X_1, \ldots, X_6$ be the margins of random variables and let $U_1, \ldots, U_6$ be independent uniform [0,1] variables. After random sampling from $U_1, \ldots, U_6$, where realizations are denoted u_1, u_2 and u_3, the sampling procedure is the following:

1. $x_1 = u_1$

2. $x_2 = F^{-1}_{r_{12};x_1}(u_2)$

3. $x_3 = F^{-1}_{r_{23};x_2}\left(F^{-1}_{r_{13|2};F_{r_{12};x_2}(x_1)}(u_3)\right)$

4. $x_4 = F^{-1}_{r_{34};x_3}\left(F^{-1}_{r_{24|3};F_{r_{23};x_3}(x_2)}\left(F^{-1}_{r_{14|23};F_{r_{13|2};F_{r_{23};x_2}(x_3)}\left(F_{r_{12};x_2}(x_1)\right)}(u_4)\right)\right)$

5. $x_5 = F^{-1}_{r_{45};x_4}\left(F^{-1}_{r_{35|4};F_{r_{34};x_4}(x_3)}\left(F^{-1}_{r_{25|34};F_{r_{24|3};F_{r_{34};x_3}(x_4)}\left(F_{r_{23};x_3}(x_2)\right)}(*)\right)\right)$

$(*) = F^{-1}_{r_{15|234};F_{r_{14|23};F_{r_{24|3};F_{r_{23};x_3}(x_2)}\left(F_{r_{34};x_3}(x_4)\right)}\left(F_{r_{13|2};F_{r_{23};x_2}(x_3)}\left(F_{r_{12};x_2}(x_1)\right)\right)}(u_5)$

6. $x_6 = F^{-1}_{r_{56};x_5}\left(F^{-1}_{r_{46|5};F_{r_{45};x_5}(x_4)}\left(F^{-1}_{r_{36|45};F_{r_{35|4};F_{r_{45};x_4}(x_5)}\left(F_{r_{34};x_4}(x_3)\right)}(*)\right)\right)$

$(*) = F^{-1}_{r_{26|345};F_{r_{25|34};F_{r_{35|4};F_{r_{34};x_4}(x_3)}\left(F_{r_{45};x_4}(x_5)\right)}\left(F_{r_{24|3};F_{r_{34};x_3}(x_4)}\left(F_{r_{23};x_3}(x_2)\right)\right)}(**)$

$$(**) = F^{-1}_{r_{16|2345};F_{r_{15|234};F_{r_{25|34};F_{r_{24|3};F_{r_{34};x_3}(x_4)}\left(F_{r_{23};x_3}(x_2)\right)}\left(F_{r_{35|4};F_{r_{34};x_4}(x_3)}\left(F_{r_{45};x_4}(x_5)\right)\right)}}(***)}(u_6)$$

$$(***) = F_{r_{14|23};F_{r_{24|3};F_{r_{23};x_3}(x_2)}\left(F_{r_{34};x_3}(x_4)\right)}\left(F_{r_{13|2};F_{r_{23};x_2}(x_3)}\left(F_{r_{12};x_2}(x_1)\right)\right)}$$

In this notation, F_r represents the conditional cumulative distribution of the copula with rank correlation r.

Appendix F: Joint distributions of simulated variables for swell

The following set of figures show the joint distribution of the pairs $H_s - T_p$, $Dir - H_s$ and $Dir - T_p$ for the swell component, regardless if the data belong to an unimodal or bimodal sea state. In the figures, the observed and simulated wave data is sorted by months, and the wave climate from the 100 samples is plotted at the same time. The colored contours show the joint probability density of each pair of variables.
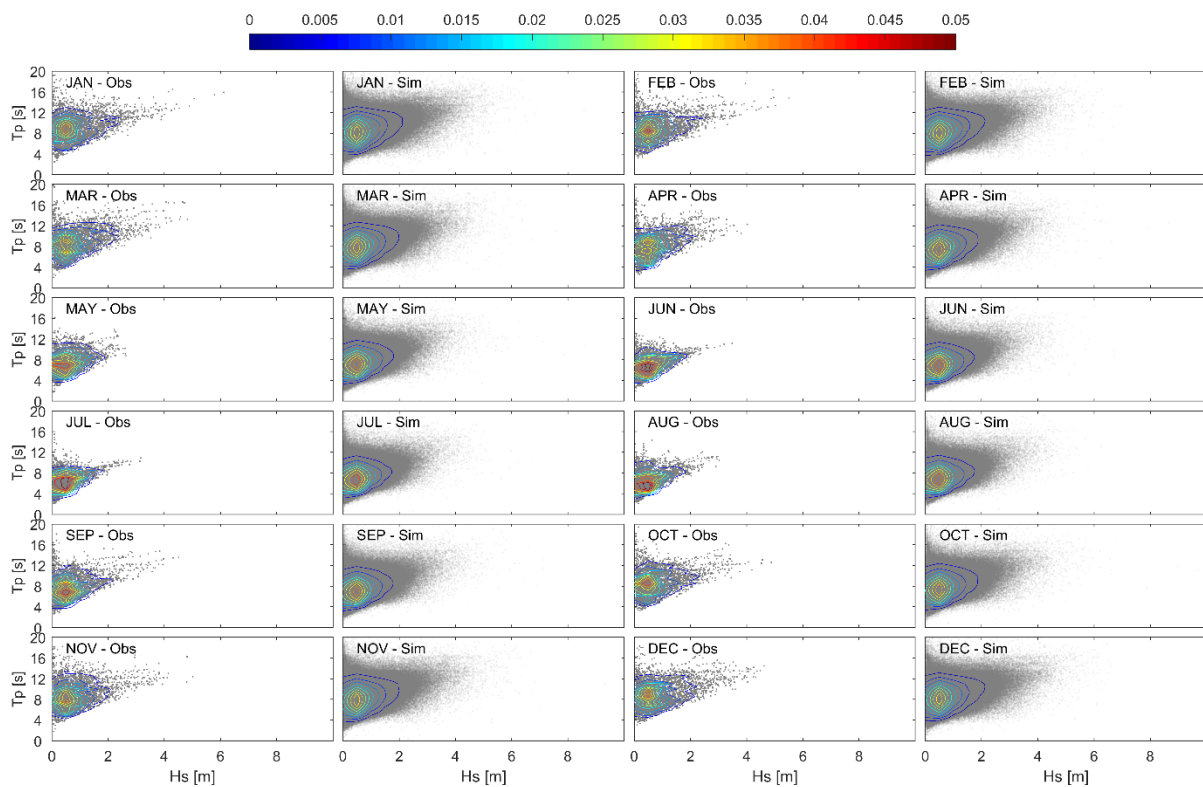
Figure F-1: Joint probability density of the pair $H_s - T_p$ for the swell component, sorted by months. Simulated values correspond to 100 samples. Joint probability density is shown by colored contours.
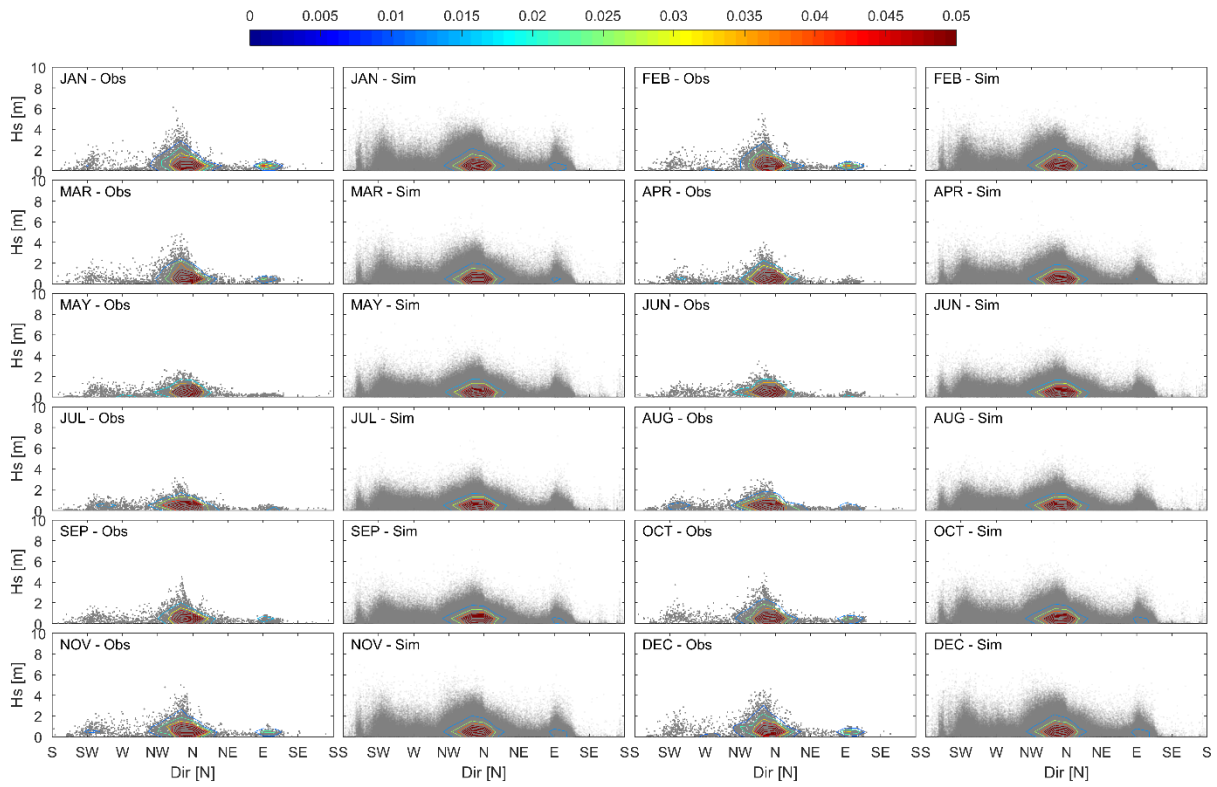
Figure F-2: Joint probability density of the pair $Dir - H_s$ for the swell component, sorted by months. Simulated values correspond to 100 samples. Joint probability density is shown by colored contours.
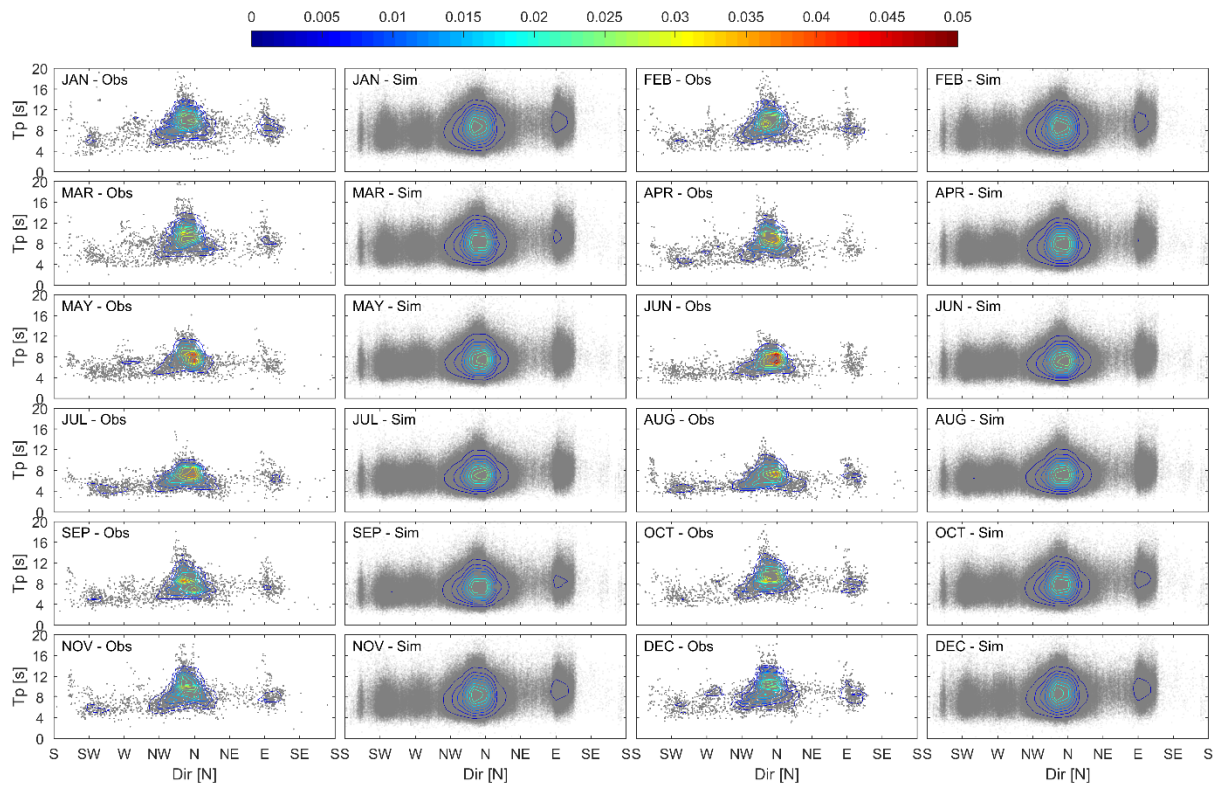
Figure F-3: Joint probability density of the pair $Dir - T_p$ for the swell component, sorted by months. Simulated values correspond to 100 samples. Joint probability density is shown by colored contours.

G.1. Validation of GCM ACCESS1.0

At seasonal scale, there exists some differences in probabilities from both predictors, but the seasonal structure is well represented in both datasets, as it can be seen in Figure G-1. The same behavior is confirmed when comparing the monthly probabilities shown in Figure G-2, where the concentration of some WTs located at the right side of the lattice during summer is observed in both predictors. Absolute differences between monthly probabilities of each WT are shown in Figure G-3.
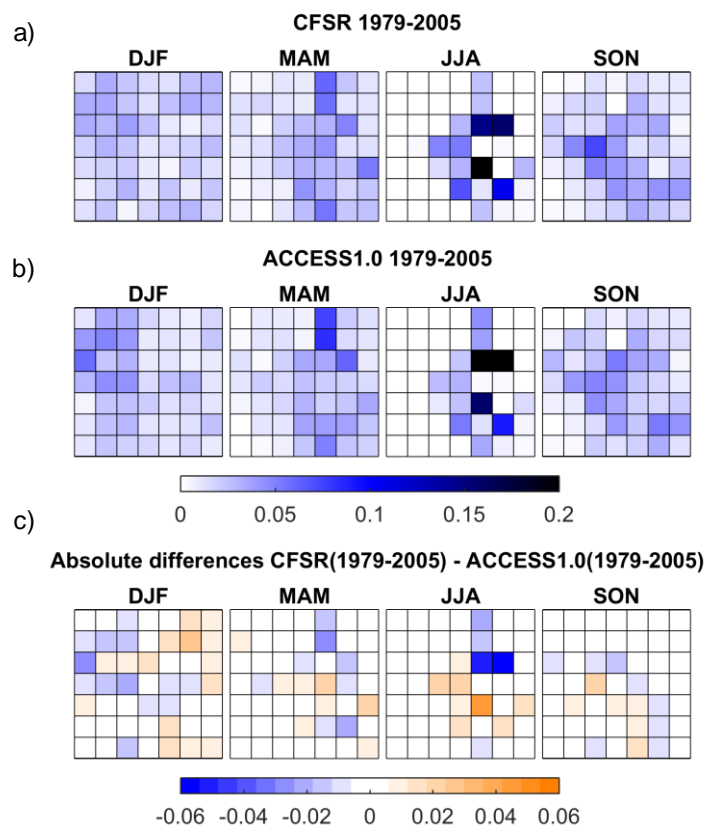
Figure G-1: a) Seasonal probability of each WT for daily predictor from CFSR, b) seasonal probability of each WT for daily predictor from ACCESS1.0 and c) absolute differences between both predictors.
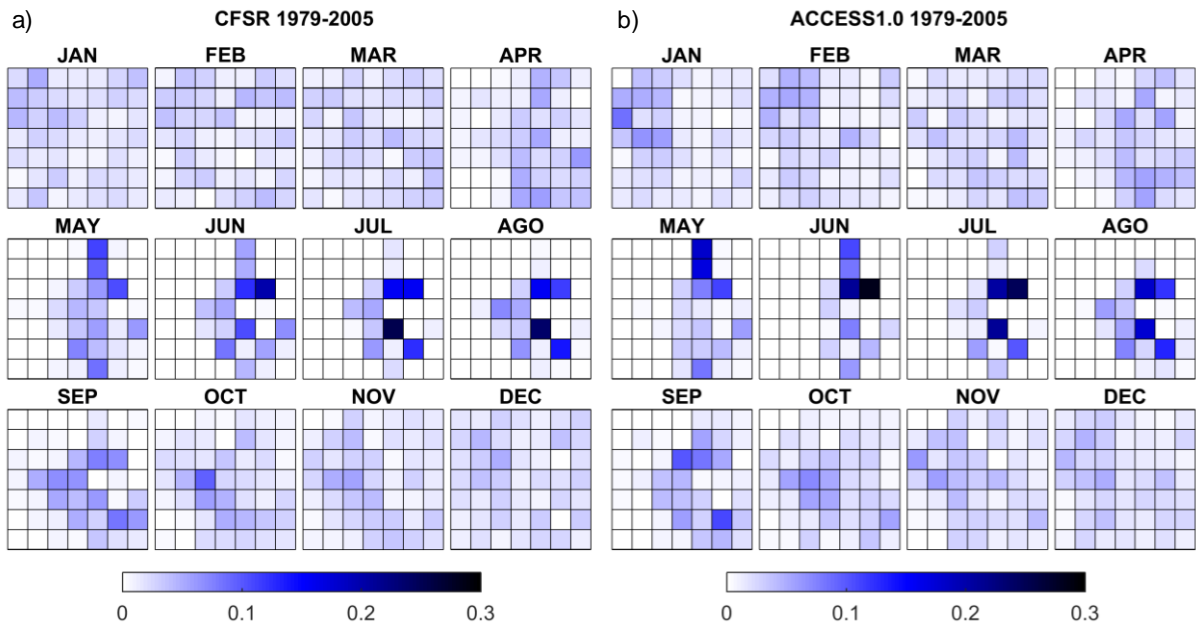
Figure G-2: a) Monthly probability of each WT for daily predictor from CFSR and b) monthly probability of each WT for daily predictor from ACCESS1.0.
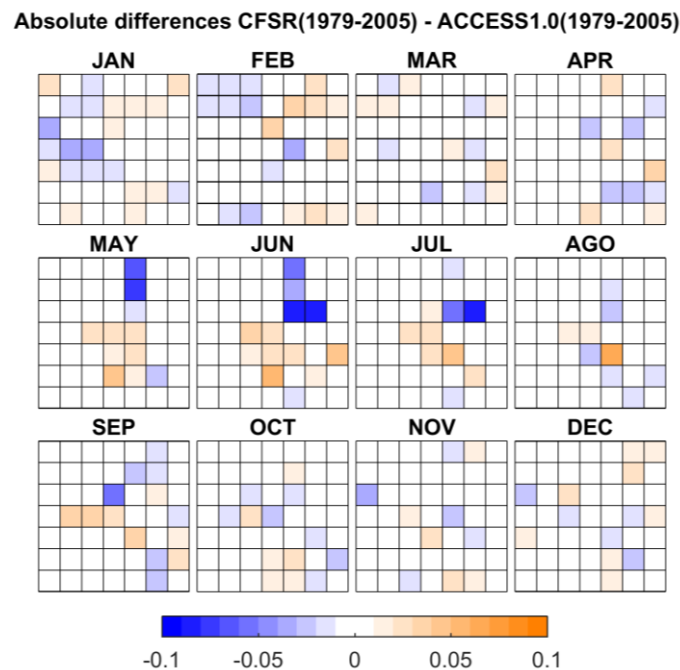

Figure G-3: Absolute differences between monthly probabilities of each WT for daily predictors from CFSR and ACCESS1.0.

G.2. Changes in future scenario

No significant changes are observed at seasonal scale, where minor changes in seasonal probabilities are presented in Figure G-4. The most important changes are observed during the summer, with an increase of the occurrence of WT41 and a decrease of WT38.

At monthly scale, the probabilities follow the same patttern, with no important changes in the future scenario. Figure G-5 and Figure G-6 confirm this, giving more detail about the changes in occurrence of WT38 and WT41: these changes happen mainly in July and August in the second place.
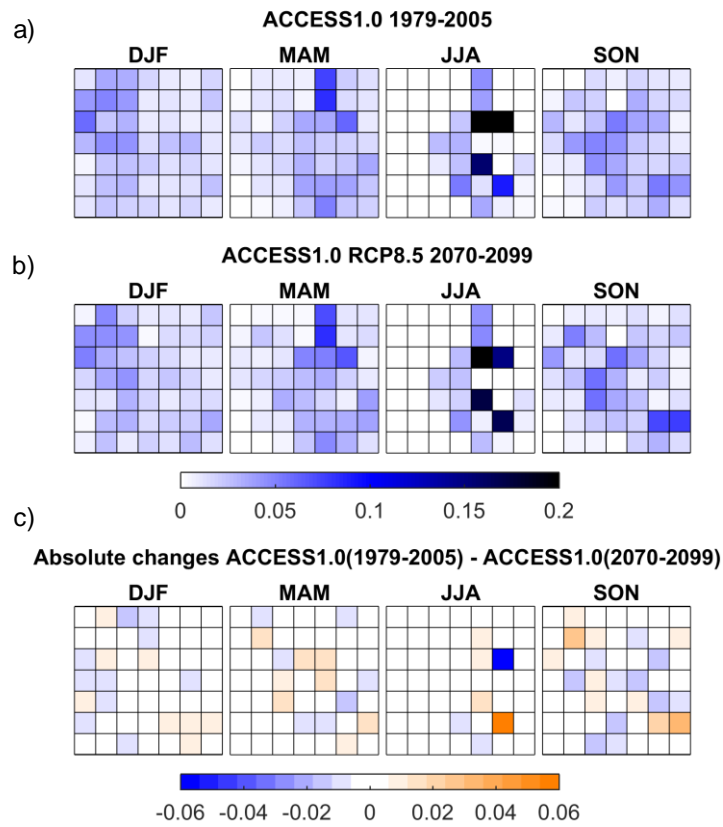
Figure G-4: a) Seasonal probability of each WT for historical period, b) seasonal probability of each WT for future scenario and c) absolute differences between both periods.
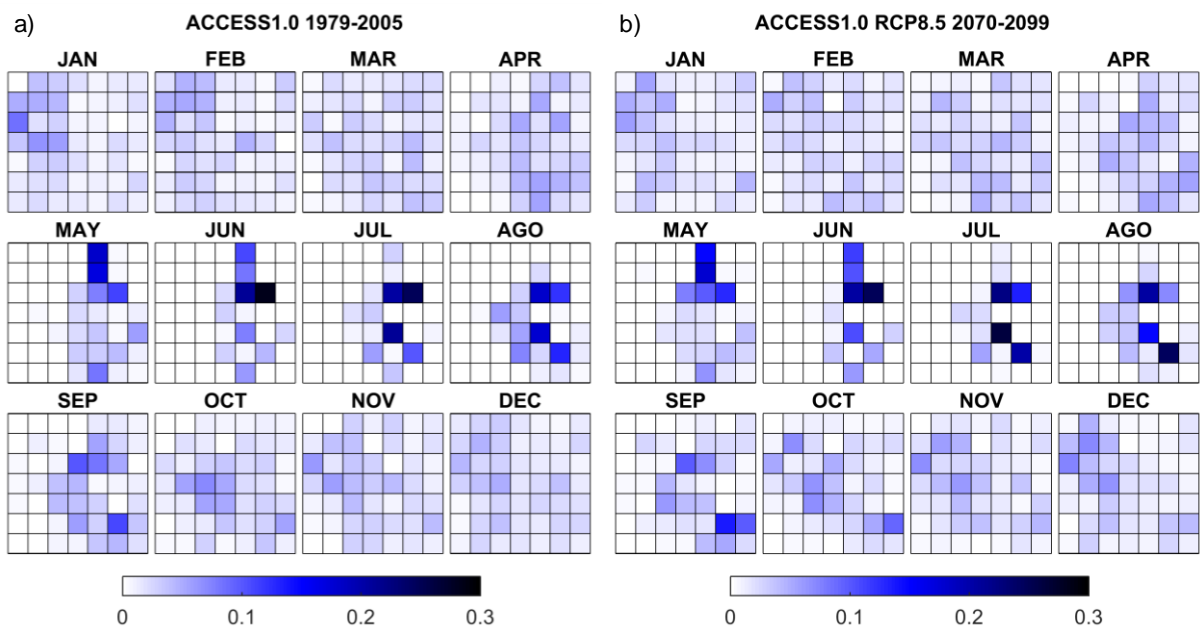

Figure G-5: a) Monthly probability of each WT for historical period and b) monthly probability of each WT for future scenario.
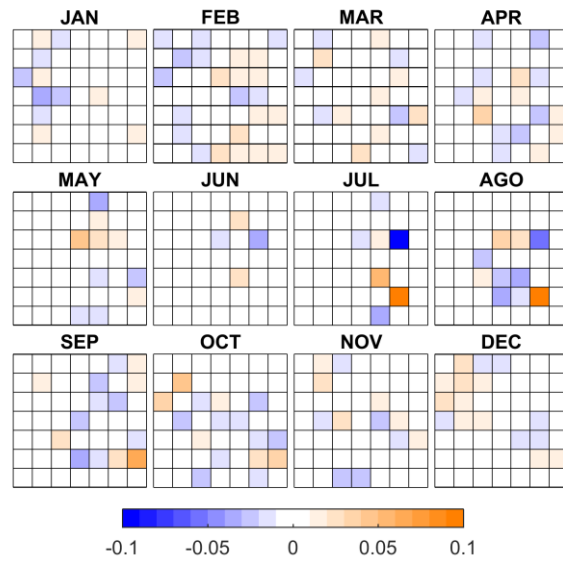
Figure G-6: Absolute differences between monthly probabilities of each WT for the historical period and future scenario.